

Organic Matter Preservation and Sequestration through the Synergistic Ferric Carbon Shuttle

Andrew Barber

A Thesis
In the Department
of
Chemistry and Biochemistry

Presented in Partial Fulfillment of the Requirements
For the Degree of
Doctor of Philosophy (Chemistry) at
Concordia University
Montreal, Quebec, Canada

September 2017

© Andrew Barber, 2017

CONCORDIA UNIVERSITY

School of Graduate Studies

This is to certify that the thesis prepared

By: Andrew Barber

Entitled: Organic Matter Preservation and Sequestration through the Synergistic Ferric Carbon Shuttle

and submitted in partial fulfillment of the requirements for the degree of

Doctor of Philosophy (Chemistry)

complies with the regulations of the University and meets the accepted standards with respect to originality and quality.

Signed by the final Examining Committee:

_____	Chair
Dr. Pedro Perez-Neto	
_____	External Examiner
Dr. Peter Douglas	
_____	External to the Program
Dr. David Walsh	
_____	Examiner
Dr. Xavier Ottenwaelder	
_____	Examiner
Dr. Sébastien Robidoux	
_____	Supervisor
Dr. Yves Gélinas	

Approved by _____
Dr. Peter Pawelek, Graduate Program Director

August 30, 2017

Dr. André Roy, Dean, Faculty of Arts and Science

Abstract

Organic Matter Preservation and Sequestration through the Synergistic Ferric Carbon Shuttle

Andrew Barber, Ph. D

Concordia University 2017

As one of the largest pools of carbon on the planet, organic matter (OM) in aquatic environments plays a major role in balancing the global cycles of carbon and oxygen. Continued sequestration of OM in sediments is required to maintain the Earth's oxidizing atmosphere and the mechanisms responsible for the preservation of OM in sediments are of the utmost importance for understanding and modelling the long-term repercussions of global climate change and ocean acidification. A common approach used to track OM in such environments involves stable carbon isotope analysis, exploiting the variability in ^{13}C content of natural OM. For stable isotope analysis to be useful, the difference in carbon stable isotope content of the OM pools of interest must be larger than the sum of the analytical uncertainty and natural spread in ^{13}C content. Here we present several examples where differences in ^{13}C content of natural OM can be used to track the fate of OM, while also providing a more realistic representation of the analytical uncertainty associated to these measurements. In addition, carbon stable isotopes were used in a long-term incubation study aimed at following the incorporation of a ^{13}C depleted dissolved algal OM tracer from solution into the sediment mineral matrix. The incorporation of this algal tracer was enhanced through interactions with redox sensitive iron oxides, especially when there is co-precipitation of iron alongside OM. The effect of iron oxide precipitation on the preservation of OM is clear, increasing the quantity of OM sequestered in sediments while also slowing its degradation. Combined with a series of C and Fe K-edge X-ray studies, we

demonstrate the importance of inner-sphere covalent complexation for the sequestration of OM via interactions with reactive iron in a series of samples from around the globe including marine and lacustrine sediments with varying oxygen exposure regimes. These strong molecular interactions stabilize iron and OM, allowing for their persistence in sediments via a synergistic ferric carbon shuttle. This allows OM to be stabilized by iron while the reduction of ferric iron is hampered by the presence of OM, leading to their persistence even in reducing environments.

Acknowledgements

I would like to start by thanking those people who have supported me during the trying times that make up a Ph.D candidacy. Most importantly my family and friends who made sure to remind me that academia isn't everything and that there is more to life than work, something that I always tend to forget. Special thanks to my mentor Karine Lalonde who was instrumental in launching this project and remains my scientific inspiration. The technical and support staff at Concordia University have been great throughout my tenure there so thanks to all of them for supporting me both in my quest for answers about iron and organic matter and for their help when organizing the Chemistry and Biochemistry Graduate Research Conference.

Of course I need to thank my supervisor Yves Gélinas for sharing my excitement about high quality, reproducible data and for constantly pushing me to bigger and better things. Finally, all of the L.E.G.O. lab members who have put up with me over the years, including Anic Imfeld, Kathryn Balind, Aleshia Kormendi, Azadeh Joshani, Amanda Gabriel, Francis Haley, Anja Moritz, Mina Ibrahim, Alex Ouellette and Rob Panetta.

Contribution of Authors

Chapter 2 was written by Andrew Barber and reviewed by Yves Gélinas. The study itself was launched by Yves Gélinas, all data interpretation was performed by Andrew Barber. The data included in this chapter was provided by 16 different stable isotope labs from around the globe. The manuscript will be submitted to *Rapid Communications in Mass Spectrometry*.

Chapter 3 was written by Andrew Barber and reviewed by Maude Sirois, Gwénaëlle Chaillou and Yves Gélinas. All data analysis and writing was done by Andrew Barber. The samples were collected over two cruises, one set by Andrew Barber and the other set of samples by Maude Sirois. It is currently accepted for publication in *Limnology and Oceanography*.

Chapter 4 was co-written by Andrew Barber and Karine Lalonde. The incubation setup itself was setup and designed by both of A.B. and K.L. The sheer number of samples generated and the need for 4 hands for the described sub-sampling required both of us, hence the equal contribution. Alfonso Mucci and Yves Gélinas reviewed the manuscript. It was published in *Marine Chemistry* in May 2014.

Chapter 5 was written by Andrew Barber but extensively revised by all of the listed co-authors. Samples were prepared by Jay Brandes or by Andrew Barber under his supervision. Andrew Barber, Karine Lalonde, Alessandra Leri and Yves Gélinas all participated in the various synchrotron analysis. Sue Wirrick and Jian Wang provided valuable insight while collecting the data as well as during subsequent discussions regarding the interpretation of the X-ray results. Kathryn Balind performed the wet chemical extractions required for the mass balance calculations. This manuscript was published in March, 2017 in *Scientific Reports*.

Chapter 6 was written by Andrew Barber and reviewed by Yves Gélinas. Charles Gobeil and André Tessier provided the samples. Synchrotron analysis was performed by Andrew Barber

and Azadeh Joshani. Andrew Barber prepared the samples under the supervision of Jay Brandes.

This chapter will be submitted as a research article in *Geochimica et Cosmochimica Acta*.

Table of Contents

List of Figures	xii
List of Tables	xviii
List of Acronyms.....	xix
Chapter 1: General Introduction.....	1
1.1. The Global Carbon Cycle:	3
1.2. Natural Organic Matter.....	6
1.3. The importance of redox reactions in marine sediments.....	10
1.4. Stable Isotope Analysis:	12
1.5. X-ray Absorption Spectroscopy.....	15
1.6. NEXAFS spectromicroscopy for sediment analysis	16
1.7. Arrangement of Thesis.....	17
Chapter 2: Measuring the $\delta^{13}\text{C}$ Signature of Dissolved Organic Carbon: An Inter-laboratory Proficiency Test.....	20
2.1 Abstract.....	21
2.2. Introduction	22
2.3. Materials and Methods.....	24
2.3.1. Sample Preparation:	24
2.3.2. Sample Pre-treatment:	26
2.3.3. High-Temperature Catalytic Oxidation (HTCO):.....	27
2.3.4. Wet Chemical Oxidation (WCO):.....	27
2.3.5. Liquid-Chromatography Wet Chemical Oxidation (LC-WCO):	27
2.3.6. Statistical Methodology:	28
2.4. Results:.....	29
2.4.1. Freshwater Samples.....	29
2.4.2. Saltwater Analysis:	33
2.5. Conclusions	34
2.5.1. Decrease in precision with decreasing DOC concentration.....	34
2.5.2. Decrease in precision for complex OM sources.....	34
2.5.3. Community Wide Repercussions:	35
Chapter 3: Stable Isotope Analysis of Dissolved Organic Carbon in Canada's Eastern Coastal Waters	37

3.1.	Abstract.....	38
3.2.	Introduction	39
3.3.	Materials and Methods.....	43
3.3.1.	St. Lawrence Valley River System	43
3.3.2.	Hudson Strait	45
3.3.3.	Sample collection	45
3.3.4.	Analytical methods	46
3.4.	Results.....	47
3.4.1.	Saguenay Fjord.....	47
3.4.2.	Northern Quebec and Labrador.....	48
3.4.3.	Across the St. Lawrence Estuary and Gulf	50
3.5.	Discussion.....	51
3.5.1.	Terrestrial Organic Matter Inputs from the Saguenay Fjord	51
3.5.2.	Dependence of $\delta^{13}\text{C}$ -DOC Signatures on the Vegetation in the Drainage Basin.....	53
3.5.3.	$\delta^{13}\text{C}$ -DOC signatures across the St. Lawrence Estuary salinity gradient	55
3.5.4.	Changes in $\delta^{13}\text{C}$ -DOC signatures with depth in the water column	57
3.5.5.	Comparison with the Baltic-North Sea Transition Zone	59
3.6.	Conclusion.....	60
Chapter 4: The role of iron in the diagenesis of organic carbon and nitrogen in sediments: A long-term incubation experiment.....		63
4.1.	Abstract.....	64
4.2.	Introduction	64
4.3.	Materials and methods:.....	67
4.3.1.	Sampling.....	67
4.3.2.	Fresh algal dissolved organic matter	68
4.3.3.	Slurry incubation setup	68
4.3.4.	Analyses	70
4.3.4.1.	Solid Phase Measurements.....	70
4.3.4.2.	DOC concentrations and isotope analysis.....	71
4.3.4.3.	Dissolved iron measurements:.....	71
4.3.4.4.	Tracking the fate of pulsed algal DOM.....	72
4.3.4.5.	Algal DOM partitioning coefficients:.....	72

4.3.4.6.	Measurement of nitrogen in solution:.....	73
4.4.	Results:.....	73
4.4.1.	Control and Fe Scenarios	75
4.4.2.	OM Amended Scenarios	77
4.5.	Discussion.....	81
4.5.1.	Role of iron in OM preservation and DOM shuttling:.....	81
4.5.2.	Accelerated iron-mediated nitrogen removal:	86
4.6.	Conclusions and implications.....	90
Chapter 5: Preservation of organic matter in marine sediments by inner-sphere interactions with reactive iron.....		
		92
5.1.	Abstract.....	93
5.2.	Introduction	93
5.3.	Materials and Methods.....	95
5.3.1.	Samples	95
5.3.1.	Sediment Organic Carbon Content Determination.....	96
5.3.2.	Synthetic Fe hydroxides and OC:Fe Complexes	98
5.3.3.	Fe Mass Balance.....	99
5.3.4.	Iron X-ray Absorption Near Edge Structure Spectroscopy.....	99
5.3.5.	Iron K-edge XANES Linear Combination Fitting	100
5.3.6.	STXM Sample Preparation and Mapping	101
5.3.7.	Near Edge X-ray Absorption Fine Structure Spectroscopy	103
5.3.8.	Redox Calculations	103
5.4.	Results and Discussion	104
5.4.1.	XANES Analyses.....	104
5.4.2.	Iron data by XANES	106
5.4.3.	Co-localization of OC and Fe by STXM	107
5.5.	Implications.....	110
Chapter 6: Redox Conditions Influence the Chemical Composition of Iron-Associated Organic Matter in Boreal Lake Sediments: a Synchrotron-Based NEXAFS Study.....		
		116
6.1.	Abstract.....	117
6.2.	Introduction	118
6.3.	Materials and Methods.....	122

6.3.1.	Study Site	122
6.3.2.	Sample Collection and Preparation	123
6.3.3.	Sample Mapping and NEXAFS Stack Collection	124
6.4.	Results	126
6.4.1.	Fe L _{3,2} edge NEXAFS Spectroscopy	126
6.4.2.	C K _{1s} NEXAFS Spectroscopy	127
6.5.	Discussion:	129
6.5.1.	Co-localization of OC and Fe	129
6.5.2.	OC:Fe complexes in the perennially oxic Basin A	132
6.5.3.	Authigenic OC:Fe complexes.....	135
6.5.4.	OC:Fe complexes in the seasonally anoxic basin	136
6.6.	Conclusions	138
Chapter 7: Conclusions, Perspectives and Future Work.....		141
References		147
Appendix A1		165
Appendix A2.....		171

List of Figures

Figure 1-1: (A) Atmospheric CO ₂ concentration as determined by the analysis of 3 separate ice cores as well as atmospheric CO ₂ measurements in Antarctica demonstrating the increase in atmospheric CO ₂ after the onset of the industrial revolution (Etheridge et al., 1996). (B) Atmospheric CO ₂ content over time (red line) measured at the Mauna Loa Observatory in Hawaii as part of the NOAA Earth System Research Laboratory and Scripps Institute of Oceanography.	2
Figure 1-2: Eh vs pH diagram for iron in seawater solution (From Rickard and Luther, 2007).	3
Figure 1-3: Schematic representation of the long-term carbon cycle (modified from Berner, 1999).	4
Figure 1-4: Schematic of the typical sequence of terminal electron acceptors dissolved in sediment porewaters with different depth (Emerson and Hedges, 2003)	11
Figure 2-1: Expected and Measured $\delta^{13}\text{C}$ signatures for the Freshwater Samples Measured (circles) and expected (triangles) $\delta^{13}\text{C}$ signature for the set of the first 7 freshwater samples for the A) WCO (N=6), B) HTOCO (N=5) and C) LC-WCO (N=3) DOC determination methods....	30
Figure 2-2: Expected and measured $\delta^{13}\text{C}$ signature for the set of the first saline samples analyzed by the A) HTOCO method (N=5) B) WCO, LC-WCO and SPE methods.	31
Figure 2-3: The Increase in Standard Deviation with Decreasing DOC Concentration.....	32
Figure 3-1: (a) Map of all sampling stations in the Upper and Lower St. Lawrence Estuaries, Gulf of the St. Lawrence and Saguenay Fjords..	44
Figure 3-2: Map of all northern sampling stations including their respective surface water DOC concentration and $\delta^{13}\text{C}$ -DOC signatures.	45

Figure 3-3: (a) $\delta^{13}\text{C}$ -DOC signatures (open squares) and salinity (filled triangles) for the surface waters across the St. Lawrence Estuary and Gulf (b) $\delta^{13}\text{C}$ -DOC signatures for the surface (open squares) and cold intermediate (filled diamonds) water layers.. 49

Figure 3-4: Sample water column $\delta^{13}\text{C}$ -DOC signatures profiles showing invariable $\delta^{13}\text{C}$ -DOC signatures at station 29 (open squares), or enrichment in $\delta^{13}\text{C}$ -DOC between the surface and cold intermediate layer at station 17 (open triangles) and station 33 (open circles)..... 51

Figure 3-5: (a) $\delta^{13}\text{C}$ -DOC signatures across the St. Lawrence Estuary and Gulf as a function of salinity. (b) $\delta^{13}\text{C}$ -DOC as a function of the DOC concentration. The error bars represent the 1σ standard deviation from four replicates for the DOC concentration (horizontal) and $\delta^{13}\text{C}$ -DOC signatures (vertical). (c) 1σ standard deviations from replicate measurements as a function of DOC concentration for samples with salinities between 0-5 (open squares), between 5-30 (open circles) and above 30 (open triangles). 61

Figure 4-1: Illustration of the incubation setup. Incubations were carried out under 3 different redox conditions (anoxic, oxic, and mixed redox) by purging the overlying water with nitrogen gas, air, or alternating between the two gases. The sediment-seawater incubations were spiked with A) Fe(II) and DOM (Fe-OM scenario), B) Fe(II) only (Fe scenario), C) DOM only (OM scenario) and D) no addition (Control scenario). Note that each vial was duplicated (in series) in this experiment (8 vials per redox condition, 24 vials in total). 69

Figure 4-2: Final nitrogen concentration (%TN) of the sediment under different redox conditions for the different amendment scenarios..... 76

Figure 4-3: Incorporation of the algal tracer in the sediment for OM and Fe-OM scenarios based on carbon isotope mass balance calculations. Black squares show the average incorporation of all

redox conditions except the oxic Fe-OM scenario. White diamonds and triangles each represent a duplicate vial of the oxic Fe-OM condition. Error bars represent standard deviation..... 79

Figure 4-4: Final stable carbon isotope signature ($\delta^{13}\text{C}_{\text{org}}$) of the sediment (last 4 time points). Error bars represent the standard deviation of the last 4 time points..... 79

Figure 4-5: Temporal evolution of the DOC concentration and isotopic signature ($\delta^{13}\text{C}_{\text{DOC}}$) in duplicate incubation vials (OM scenario, oxic conditions). 80

Figure 4-6: Simplified pathways of DOM incorporation (1. Adsorption/Desorption and 2. Co-precipitation during Fe(II) oxidation) 3. Organic carbon remineralization to CO₂, 4. Bacterial denitrification/anammox, and 5. Iron mediated N₂ production) in marine sediments. 82

Figure 5-1. Iron K-edge XANES Linear Combination Fitting of the raw sediment Fe spectra for the Mexican 306 sediment using three end-members: goethite/lepidocrocite, ferric oxalate and the reactive iron extracted sediment residue. The best fit (red trace) is almost superimposed on the spectra for the raw, untreated sediment (blue trace). 101

Figure 5-2: STXM “Scan Maps” collected between (a) 280 and 288.6 eV for carbon, and (b) between 700 and 710 eV for iron, respectively. These maps allowed selecting areas where OC and Fe were co-localized in our samples for NEXAFS collection. 102

Figure 5-3: Iron K-edge spectra for the samples analyzed in this study. (a) First derivative of Fe 1s XANES spectra for goethite, ferric oxalate and synthetic lepidocrocite with initial solution OC:Fe Molar ratios of 1, 3, and 10. The intersecting line at 7124.5 eV highlights the shift in absorbance maxima for ferric oxalate; (b) Normalized Fe 1s XANES spectra for raw sediments with the vertical line at 7132.8 eV representing the absorption maximum for goethite/lepidocrocite..... 105

Figure 5-4: Iron K-edge XANES linear combination fitting results showing the OC-free iron oxides (blue), OC-complexed reactive iron (brown), and residual sediment iron (green) contributions to the total sediment Fe pool. 107

Figure 5-5: Chemical composition of co-localized iron (panels a and b-d) and organic matter (panels A and E-H). (a) Representative 12 x 8 μm X-ray microscopy image from the Mexican Margin sediment (Station 306); (b) Iron L3 edge XAS spectra for the Fe cluster maps in panels (c) and (d); (e) Carbon K-edge XAS spectra for the (c) cluster maps in panels (f), (g) and (h). Note that colored traces in panels (b) and (e) correspond to the different coloured carbon clusters in panels (c-d), and (f-h), respectively. Each cluster was identified using the PCA and clustering analysis described in the methods section. 109

Figure 5-6: Correlation between the quantity of OC associated to iron oxides measured by wet chemical extraction (Lalonde et al., 2012), and the quantity of Fe found complexed to OC measured by XANES (this work) for the samples studied in this work. Sediments accumulating under anoxic conditions are excluded from the regression (see text for explanations). 112

Figure 6-1: (A and B) Fe L_{3,2} edge cluster maps (13 x 13 μm) for sediments from the oxic basin of Lake Tantaré. (C) Fe L_{3,2} NEXAFS spectra corresponding to the individual cluster maps... 123

Figure 6-2: (A, B and C) Fe L_{3,2} edge cluster maps (10 x 10 μm) for sediments from the anoxic basin of Lake Tantaré. (D) Fe L_{3,2} NEXAFS spectra corresponding to the individual cluster maps. 126

Figure 6-3: (A) C K_{1s} edge NEXAFS spectra for the oxic surface sediments. Each spectra corresponds to the similarly labelled cluster maps (B-I). The dashed vertical lines are located at photon energies of interest (285.1 eV, 288.6 eV and 289.5 eV)..... 128

Figure 6-4: (A) C K_{1s} edge NEXAFS spectra for the anoxic surface sediments. Each spectra corresponds to the similarly labelled cluster maps (B-G). The dashed vertical lines are located at photon energies of interest (285.1 eV, 286.6 eV, 287.4 eV, 288.6 eV and 290. 2 eV). 129

Figure 6-5: (A) C K_{1s} edge NEXAFS spectra for the authigenic iron complexes from the Teflon plate material. Each spectra corresponds to the similarly labelled cluster maps (B-E). The dashed vertical lines are located at photon energies of interest (285.1 eV, 286.6 eV, 288.6 eV and 289.5 eV)..... 130

Figure A2-1: The temporal evolution of the DOC concentration (white) and δ¹³C signature (teal) for the oxic, OM amended scenario. V1 and V2 each represent duplicate vials. 174

Figure A2-2: The temporal evolution of the DOC concentration (white) and δ¹³C signature (teal) for the mixed redox, OM amended scenario. Periods appearing with a grey background were anoxic at the time of subsampling while those appearing on a white background were subsampled while the vials were maintained under oxic conditions. V1 and V2 each represent duplicate vials. 174

Figure A2-3: The temporal evolution of the DOC concentration (white) and δ¹³C signature (teal) for the anoxic, OM amended scenario. V1 and V2 each represent duplicate vials. 175

Figure A2-4: The temporal evolution of the DOC concentration (white) and δ¹³C signature (teal) for the oxic, Fe and OM amended scenario. V1 and V2 each represent duplicate vials. 176

Figure A2-5: The temporal evolution of the DOC concentration (white) and δ¹³C signature (teal) for the mixed redox, Fe and OM amended scenario. Periods appearing with a grey background were anoxic at the time of subsampling while those appearing on a white background were subsampled while the vials were maintained under oxic conditions. V1 and V2 each represent duplicate vials. 177

Figure A2-6: The temporal evolution of the DOC concentration (white) and $\delta^{13}\text{C}$ signature (teal) for the anoxic, Fe and OM amended scenario. V1 and V2 each represent duplicate vials..... 177

Figure A2-7: The temporal evolution of the DOC concentration (white) and $\delta^{13}\text{C}$ signature (teal) for the oxic, control scenario. V1 and V2 each represent duplicate vials..... 178

Figure A2-8: The temporal evolution of the DOC concentration (white) and $\delta^{13}\text{C}$ signature (teal) for the mixed redox, control scenario. Periods appearing with a grey background were anoxic at the time of subsampling while those appearing on a white background were subsampled while the vials were maintained under oxic conditions. V1 and V2 each represent duplicate vials. ... 179

Figure A2-9: The temporal evolution of the DOC concentration (white) and $\delta^{13}\text{C}$ signature (teal) for the anoxic, control scenario. V1 and V2 each represent duplicate vials. 180

Figure A2-10: The temporal evolution of the DOC concentration (white) and $\delta^{13}\text{C}$ signature (teal) for the oxic, Fe amended scenario. V1 and V2 each represent duplicate vials. 181

Figure A2-11: The temporal evolution of the DOC concentration (white) and $\delta^{13}\text{C}$ signature (teal) for the mixed redox, Fe amended scenario. Periods appearing with a grey background were anoxic at the time of subsampling while those appearing on a white background were subsampled while the vials were maintained under oxic conditions. V1 and V2 each represent duplicate vials. 181

Figure A2-12: The temporal evolution of the DOC concentration (white) and $\delta^{13}\text{C}$ signature (teal) for the anoxic, Fe scenario. V1 and V2 each represent duplicate vials..... 182

Figure A2-13: Soluble Fe^{2+} concentration with time for the unamended control vials in the anoxic, oxic and mixed redox scenarios. 183

Figure A2-14: Soluble Fe^{2+} concentration with time for the Fe(II) amended vials in the anoxic, oxic and mixed redox scenarios..... 184

List of Tables

Table 2-1: List of Sample Identities and Expected DOC Concentration.....	26
Table 4-1: Concentrations of dissolved species at the end of the incubations (250 days, asymptotic value) in $\mu\text{mol L}^{-1}$. Standard deviations are shown in brackets when available.	77
Table 4-2: Pseudo first-order degradation rate constants and half-lives of DOC in oxic and anoxic incubations. Standard deviations are shown in brackets.	81
Table 5-1. Composition of the samples and raw sediment Fe K-edge Linear combination fitting results	97
Table A1-1: $\delta^{13}\text{C}$ -DOC signatures and DOC concentrations for the Saguenay Fjord	166
Table A1-2: $\delta^{13}\text{C}$ -DOC signatures and DOC concentrations for the Upper St. Lawrence Estuary.....	165
Table A1-3: $\delta^{13}\text{C}$ -DOC signatures and DOC concentrations for the Lower St. Lawrence Estuary and Gulf	166

List of Abbreviations

$\delta^{13}\text{C}$ -DOC – Carbon stable isotope signature of dissolved organic carbon

BNL – Brookhaven National Laboratories

CLS – Canadian Light Source

CIL – Cold Intermediate Layer

DOC – Dissolved Organic Carbon

DCB – Dithionite Citrate Bicarbonate

HTCO – High Temperature Catalytic oxidation

IRMS – Isotope ratio mass spectrometry

LC-WCO – Liquid Chromatography Wet Chemical Oxidation

LSLE – Lower St. Lawrence Estuary

NEXAFS – Near Edge X-ray Absorption Fine Structure

OM – Organic Matter

OC – Organic Carbon

SLE – St. Lawrence Estuary

SPE – Solid Phase Extraction

STXM – Scanning Transmission X-ray Microscopy

TN – Total Nitrogen

USLE – Upper St. Lawrence Estuary

WCO – Wet Chemical Oxidation

XANES – X-ray Absorption Near Edge Structure

XAS – X-ray Absorption Spectroscopy

Chapter 1: General Introduction

Among the most pressing issues in modern science is continued growth of the atmospheric carbon pool and its relation to global anthropogenic climate change. In fact, since the start of the industrial revolution the size of the atmospheric carbon pool has been on the rise at an ever increasing rate (Etheridge et al., 1996) (Fig. 1-1). This phenomenon is often attributed to the burning of fossil fuels, releasing carbon which has been sequestered within soils and sediments over millions of years, creating an imbalance between the short-term and long-term global carbon cycles (Berner, 2003). Rectifying this imbalance by sequestering large quantities of carbon in the earth's sediments and soils is an interesting solution but it is equally important to understand the mechanisms that allow for the continued burial of carbon already present in such environments. The carbon sequestered via interactions with redox or pH sensitive minerals is in danger of being released due to changes in ocean pH via ocean acidification and bottom water oxygen content (hypoxia and anoxia)..

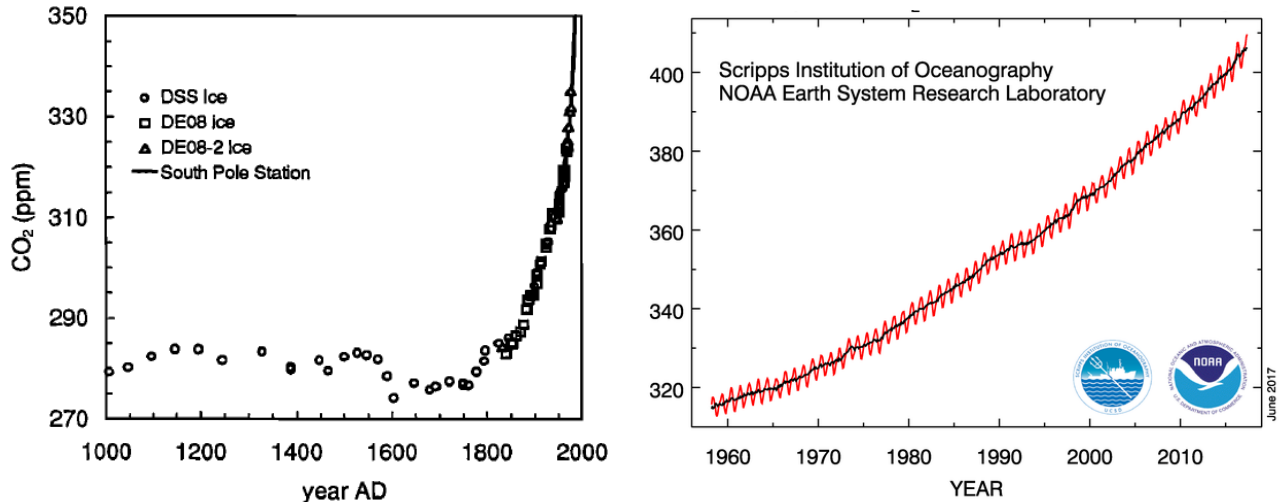


Figure 1-1: (Left) Atmospheric CO₂ concentration as determined by the analysis of 3 separate ice cores as well as atmospheric CO₂ measurements in Antarctica demonstrating the increase in atmospheric CO₂ after the onset of the industrial revolution (Etheridge et al., 1996). (Right) Atmospheric CO₂ content over time (red line) measured at the Mauna Loa Observatory in Hawaii as part of the NOAA Earth System Research Laboratory and Scripps Institute of Oceanography. The black line represents the seasonally corrected average atmospheric CO₂ concentration (taken from <https://www.esrl.noaa.gov/gmd/ccgg/trends/full.html>).

Changes in bottom water and porewater pH and Eh causes shifts in which species dominate in the water column and in the sediment, easily visualized by the Eh vs pH diagram for iron (Fig. 1-2).

This thesis will comprise a series of publications focused on the study of carbon across the aquatic continuum and during deposition/burial in sediments, building towards a better understanding of the synergistic interactions between iron oxides and OC in marine sediments, stabilizing OM matter while also protecting redox sensitive iron species.

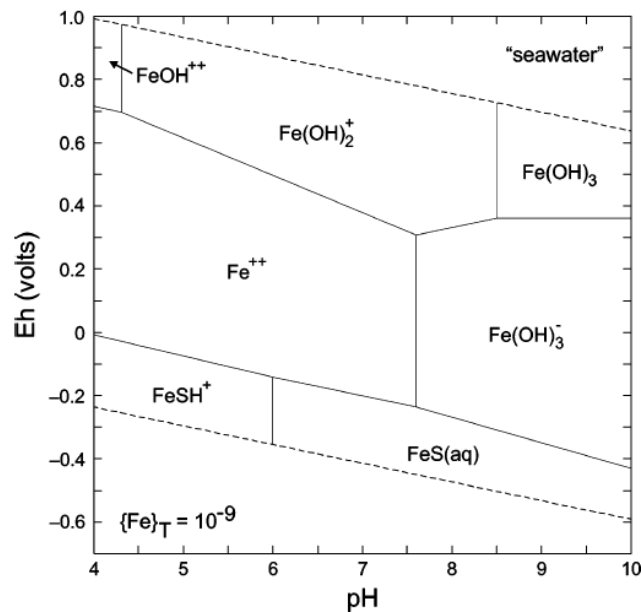


Figure 1-2: Eh vs pH diagram for iron in as seawater solution (From Rickard and Luther, 2007).

1.1. The Global Carbon Cycle:

The global carbon cycle is, at its simplest, a representation of the various pools of carbon on the planet and the exchanges between them. The work presented here will focus on carbon from only a select few, yet quantitatively significant carbon reservoirs including the world's oceans and sediments (Hedges and Keil, 1995). The importance of these reservoirs arises not only from the amount of carbon stored within them but also the mechanisms that keep carbon sequestered therein. Marine sediments act as a bridge between the long-term and short-term carbon cycles, allowing

for the transfer of carbon from rapid turnover pools to geologically stable sinks of carbon, making them particularly interesting for the study of carbon sequestration dynamics. Of specific interest are the interactions between OM and redox sensitive metals that play a critical role in sequestering carbon in a variety of settings, particularly marine and lacustrine sediments as well as in soils (Solomon et al., 2012a; Lalonde et al., 2012; Estes et al., 2017).

Over geologic timescales the Earth's denser oceanic crust and by extension the sedimentary material which composes it subducts beneath the less dense continental crust, allowing for carbon to be buried deep within the Earth (see figure 1-3 for a visual representation of the long-term carbon cycle) (Berner 1999). Under typical circumstances this carbon remains trapped in such environments until it is converted into CO_2 deep within the Earth's crust and mantle before being released back into atmosphere cycle via volcanism, with a small fraction escaping this fate and becoming fossil fuels. The extraction and subsequent combustion of fossil fuels circumvents this by releasing CO_2 back into the atmosphere prematurely, rejoining the quick-turnover carbon cycle.

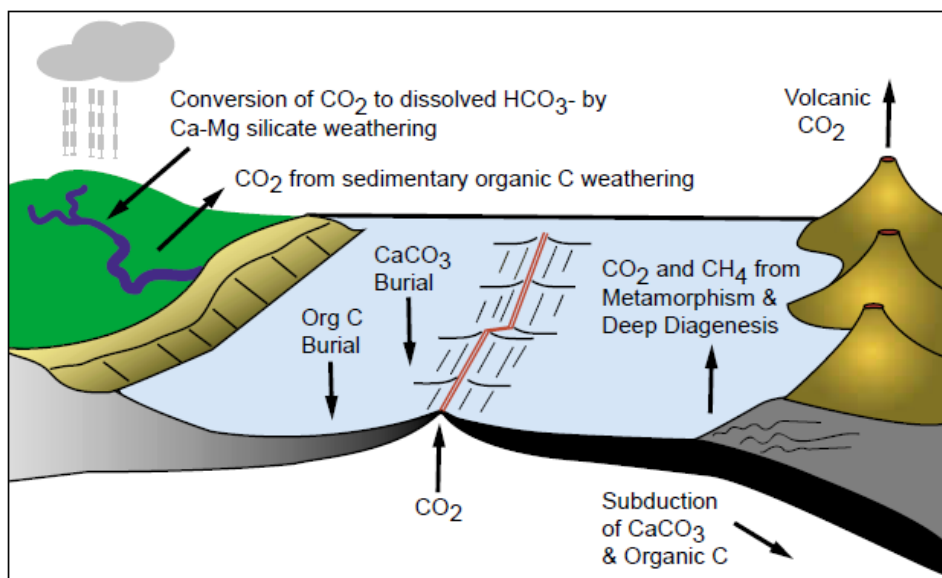


Figure 1-3: Schematic representation of the long-term carbon cycle (modified from Berner, 1999).

The rapid turnover, short term carbon cycle, works primarily on a yearly to decadal timeframe and includes the primary active pools of carbon, mainly the atmosphere, the ocean, soils, sediments and life (Berner, 1999). On the other hand, the slow moving carbon cycle involves carbon reservoirs with much longer residency times including sediments and sedimentary rocks (Berner, 2004), acting on a geological timescale. This transition from active cycling pools to rocks is what differentiates the slow and fast moving carbon cycles (Berner, 2004). Environmental changes across these different pools may have far reaching impacts with regards to long term carbon sequestration, explaining our interest in the topic.

Despite its prevalence in the media, the atmospheric carbon pool is substantially smaller than many other C pools, containing approximately 800 Pg of C (Scharlemann et al., 2014). Comparatively, the global ocean contains approximately 38 000 Pg of carbon, primarily found in the form of dissolved carbonates (Hedges and Keil, 1995) Despite their low average organic carbon content (1-2 % wt/wt) of marine sediments and sedimentary rocks, these pools combine to bury over 22,000 times more carbon than is currently in the atmosphere (Lalonde et al., 2012), making marine sediments the most important sink of OM on the planet. This is made possible due to the sheer volume of sediments and sedimentary rocks found on Earth.

The importance of marine sediments on the environment does not end there, as the sequestration of reduction power in the form of OM is partially responsible for the rise in atmospheric oxygen. Even in modern times, these geologically stable carbon stores regulate the quantity of O₂ and CO₂ in the atmosphere (Berner, 2003). The burial of reduction potential (in the form of reduced carbon functionalities) allowed for the buildup of atmospheric oxygen, without this burial mechanism the atmosphere would have remained more reducing than oxidizing. Thus it is the combination of the

total amount of carbon stored in these pools and their importance in regulating the cycling of carbon that drives out interest to study such environments.

1.2. Natural Organic Matter

The compositional complexity and heterogeneous nature of natural OM make it difficult to tease out the mechanisms that allow for its preservation in sediments and soils. Over 90% of the OM generated via primary production in the ocean, is degraded as it sinks within the water column. Another 90% of the residual, now heavily altered, OM reaching the seafloor is degraded during early diagenesis (the sum of both physical and biological processes which alter the composition of sediments during deposition and burial) (Hedges and Keil, 1995). The chemical composition of the OM which escapes rapid degradation remains elusive (Hedges et al., 1997; Knicker, 2004), as until recently bulk organic extractions and spectroscopic analysis were the primary tools used for the characterization of sediment OM. Owing to the highly variable size and reactivity range of this pool, the majority of sediment OM falls outside the analytical window of these techniques and is therefore deemed “molecularly uncharacterizable” (Hedges et al., 2000). Recent applications of solid-state ^{13}C Nuclear Magnetic Resonance (Gélinas et al., 2001; Hedges et al., 2001; Simpson and Hatcher, 2004; de Leeuw et al., 2006), Fourier Transform-Infrared spectroscopy (Celi et al., 1997) and ultra-high resolution mass spectrometry (Riedel et al., 2013; Riedel et al., 2014) have allowed for further characterization of a variety of complex natural OM samples, though these methods often require intricate sample preparation steps that alter the chemical structure of OM or selectively extracts only a small fraction of the bulk sample (Zonneveld et al., 2010). As such, novel techniques with broader analytical windows, involving less sample manipulation, must be used for complete OM characterization.

Determining the composition of sediment OM remains but a stepping stone to the ultimate goal of this work which is to better understand the mechanisms by which OM is preserved in sedimentary environments. In general, the OM preservation mechanisms can be divided in two groups, first as processes that physically sequester and protect OM from degradation, and the other whereby OM is “refractorized” through molecular level transformations, thus reducing its bioavailability. Although it is useful to categorize OM preservation mechanisms in this way, it is equally important to realize that actual OM sequestration likely involves a combination of these processes, and that physical protection mechanisms often go hand in hand with molecular level re-working mechanisms (Burdige, 2007).

Physical protection of OM through interactions with the inorganic sediment mineral matrix has been proposed in order to explain the presence of labile organic molecules in old, extensively re-worked marine sediments (Burdige, 2007). Sorption of OM to mesopores (pores with diameters between 2 and 50 nm) either on the surface of, or within, the sediment matrix material likely dominates the preservative interactions responsible for the selective preservation of OM (Mayer, 1994a; Mayer, 1994b). Long term preservation of OM, requires nearly irreversible sorption between the OM and the inorganic or organic sediment matrix (Mayer, 1994a; Mayer, 1994b; Henrichs, 1995). Irreversible binding of OM within mesopores would protect it by creating a physical barrier between the OM and the high molecular weight exoenzymes synthesized by bacteria that are thought to be responsible for the enzymatic degradation of OM (Mayer, 1994a). Even if exoenzymes can partially enter the interlayers of expandable clays or inorganic mesopores, it has been proposed that steric hinderance caused by these inclusions inhibits enzymatic degradation by preventing the enzymes from undergoing the necessary conformational changes required for their proper functioning. Sorption of labile OM within mesopores can also promote a

variety of “refractorization” mechanisms which may in part account for the abundance of refractory OM which is found within sediments at depth (Collins et al., 1995).

All of the upcoming mechanisms involve alterations in OM composition at the molecular level, creating intrinsically refractory organic molecules that are less susceptible to degradation. One such process is geopolymerization whereby OM is broken down into low molecular weight molecules that can then undergo condensation reactions forming recalcitrant high molecular weight OM (Tissot and Welte, 1978). The classic example of this process is the Maillard condensation reaction forming melanoidins through the condensation of amino acids and sugars (Thurman, 1985). Other proposed abiotic condensation reactions that are thought to occur in marine sediments include cross-linkage of peptides to other macromolecules (Nguyen and Harvey, 2001), sulfurization of lipids or carbohydrates (Tegelaar et al., 1989), and finally the formation of heterocyclic N-containing molecules through the incorporation of ammonium species into non-nitrogen containing organic molecules (Knicker, 2004).

In addition to the abiotic chemical re-working processes listed above, intrinsically refractory material can be found within organic biomolecules. For instance, cell wall components such as algaenans can escape degradation owing to their highly aliphatic, insoluble and non-hydrolyzable nature (Knicker and Hatcher, 1997; Knicker, 2004). Although these compounds do not account for a large fraction of natural biomass, the bulk OM pool becomes enriched in such compounds during OM degradation owing to their refractory nature, while the other more labile constituents such as proteins, lipids and carbohydrates, are degraded. Other forms of refractory material such as black carbon, not formed during sediment diagenesis but through the pyrolysis of terrestrial organic matter (Riedel et al., 2014) or the weathering of graphitic rocks (Dickens et al., 2004), can be transferred to aquatic environments by rivers and aeolian dust transport. The increasing relative

abundance of this pool of refractory OM compounds in sediments compared to more bioavailable, fresh OM is indicative of enrichment through selective preservation.

The “melting pot” of different processes by which OM can be preserved in marine sediments can be better understood by elucidating the speciation of the sediment OM in relation to the mineral matrix. X-ray absorption spectromicroscopy is the ideal tool for this study by providing OM and mineral speciation data overlaid onto actual visual images of intact sediment particles. A central tenet of biochemistry, that structure determines function, can be modified and applied to sediment OM, as composition determines mechanism of preservation, something we will explore in the latter chapters of this thesis. Further characterization of natural sediment OM will narrow down the potential preservation mechanisms responsible for the selective preservation of specific OM compounds.

Using the most advanced synchrotron X-ray techniques available we can circumvent several of the method artefacts created during the bulk preparation methods required to disrupt the sediment mineral matrix. Recent advances in synchrotron X-ray instrumentation, specifically the energy and spatial resolution available for spectromicroscopic techniques, have made possible the analysis of complex OM samples at the nanometer-scale (Lehmann et al., 2008). Alongside these technical advances, the development of novel sample preparation methods using carbon-free embedding materials have allowed researchers to characterize the composition of soil (Lehmann et al., 2005; Lehmann et al., 2008; Lehmann et al., 2009; Solomon et al., 2012a; Solomon et al., 2012b) and marine particulate OM in the ocean (Brandes et al., 2004). Due to the relatively low OC concentration (~1% is typical for marine sediments compared to 12% for the soils studied to date) and the difficulty associated to sample collection, many of these X-ray techniques have not extensively been used to study marine sediment samples, until now. Despite

these difficulties we have characterized sediment OM from a variety of depositional settings on intact sediment particles embedded in an elemental sulfur resin using STXM. The main focus of this portion of our work was aimed at elucidating the mechanisms responsible for the sequestration of carbon through the chemical characterization of sediment OM in relation to its interactions with the sediment mineral micro-fabrics. A complementary objective is probing the effects of the physico-chemical characteristics of the deposition environment, most importantly the redox potential, on sediment OM composition.

1.3. The Importance of Redox Reactions in Marine Sediments

The finding that approximately 20-30% of the total sediment OC pool is associated to reactive iron oxides (Lalonde et al., 2012) is not only interesting due to the sheer amount of carbon this adds up to but also due to the redox sensitive nature of metal oxides. Sediments depth profiles have a strong vertical redox profile, visualized as redox “zones” separated based on the presence/absence of specific terminal electron acceptors (Fig. 1-4) (Emerson and Hedges, 2003). In sediments with oxygenated overlying waters, oxygen can diffuse within surface sediments, where it is the terminal electron acceptor for a cascade of redox reactions. These redox reactions influence the not only the redox sensitive species directly targeted by changes in sediment redox potential with depth but also other non-redox sensitive components of the sediment mineral matrix which interact with them.

Within the oxic layers of marine sediments, iron is found primarily in the form of iron oxyhydroxides (referred to as iron oxides in this text) such as ferrihydrite, lepidocrocite, goethite and hematite (Cornell and Schwertmann, 2006). The porewater pH, redox potential, salt content and OM content will all influence the speciation of the iron oxides that form at the sediment oxic/anoxic redox boundary. Anions such as salts and certain components of OM can poison the

iron oxide crystal structure, preventing crystal structure growth as well as affecting the overall speciation of iron (Schwertmann, 1966).

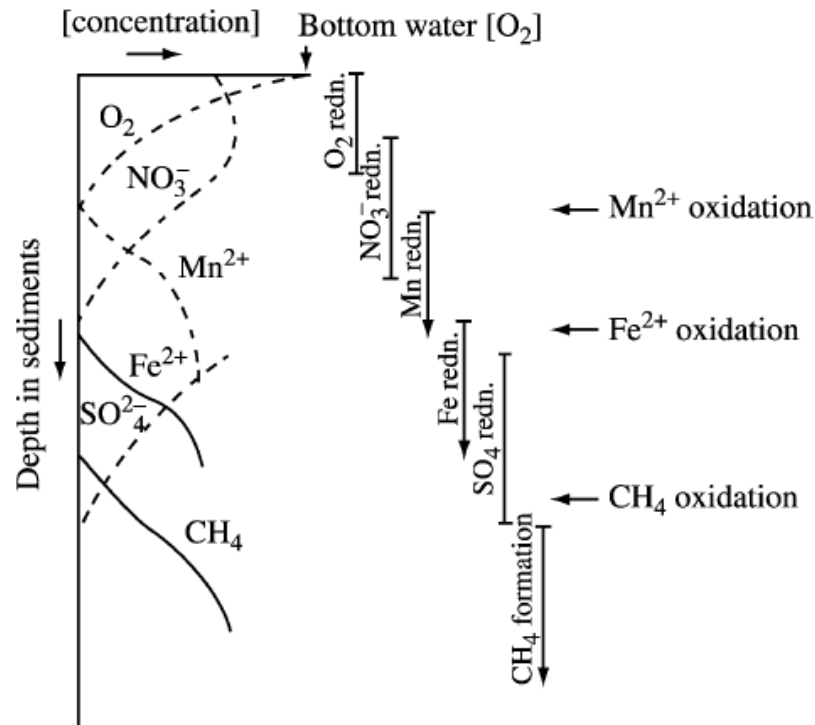


Figure 1-4: Schematic of the typical sequence of terminal electron acceptors dissolved in sediment porewaters with different depth (Emerson and Hedges, 2003)

At the sediment oxic/anoxic redox boundary the iron oxides abundant in surface sediments undergo reductive dissolution, allowing for a buildup of soluble ferrous iron in the sediment porewaters. This pool of Fe(II) can then diffuse within the sediment, precipitating out as iron sulfur minerals within the anoxic sediment layers or diffuse back into the oxic sediment layers where it can reform iron oxides. In the latter situation the precipitation of iron as iron oxides can occur alongside dissolved organics, allowing for co-precipitation of both species. Such a co-precipitation mechanism leads to rather high molar OC:Fe ratios of above 5, as opposed to pure sorptive processes which will have lower OC:Fe molar ratios (Wagai and Mayer, 2007; Raiswell

and Canfield, 2012). Although it is clear that OM can be co-extracted alongside iron oxides, the overall importance of these interactions towards the long-term sequestration and preservation is unclear. If the interactions are formed primarily from weak electrostatic effects, these complexes could not allow for the long-term preservation of OM while strong, inner-sphere covalent interactions would potentially allow for the stabilization of OM and iron over such a temporal scale. The OC:Fe molar ratio determined from the co-extraction of both species can be helpful in narrowing down potential interaction mechanisms (Wagai and Mayer, 2007; Lalonde et al., 2012), yet care must be taken as co-extraction does not necessarily indicate direct association or co-localization. We propose that the iron-OM complexes which form in sediments may prevent the reductive dissolution of iron (Haese et al., 1997) while also sequestering OM, transporting it through the sediment oxic/anoxic interface where it can be preserved.

1.4. Stable Isotope Analysis:

One of the avenues commonly used to track the fate of OM includes the analysis of carbon stable isotope signatures, taking advantage of small variations in the relative proportion of ^{13}C to ^{12}C in natural organic matter. About 98.9% of all carbon is found as the lighter stable isotope (^{12}C) with the remaining 1.1% mostly consisting of the second stable isotope of carbon (^{13}C) (Peterson and Fry, 1987). As an aside, in this work we deal exclusively with the stable isotopes of carbon, excluding the radio-isotope of carbon (^{14}C). In reality the $\sim 1.1\%$ is not a constant value, with natural changes in this atom percent occurring at the fourth and fifth decimal places depending on the source carbon used in carbon fixation as well as differences in carbon fixation mechanisms (Farquhar et al., 1989). The relative proportion of ^{13}C to ^{12}C in OM is initially set during carbon fixation, with differences in starting material (gaseous CO_2 vs dissolved carbonates) and C fixation pathways leading to differences in ^{13}C content. These differences are

determined using an isotope ratio mass spectrometer (IRMS) and are commonly reported using the delta notation using:

$$\delta^{13}\text{C} (\text{‰}) = \left(\frac{{}^{13}\text{R}_{\text{Sample}}}{{}^{13}\text{R}_{\text{Reference}}} - 1 \right) \times 1000 \quad (\text{Eq. 1-1})$$

where R is the ratio of $^{13}\text{C}/^{12}\text{C}$ in either the sample the reference material. By convention a carbonate mineral (Vienne Pee Dee Belimnite) is used as the reference material, with its $^{13}\text{C}/^{12}\text{C}$ ratio being set as the 0 reference point for this scale.

The IRMS itself is not used to measure the organic matter directly but rather the combustion products of that organic matter. The fact that the ^{13}C content is conserved during combustion is what makes this possible. A series of Faraday cups are aligned to measure specific masses, or more specifically mass/charge ratios, for carbon the masses of interest include 44 ($^{12}\text{C} \text{ }^{16}\text{O} \text{ }^{16}\text{O}$), 45 ($^{13}\text{C} \text{ }^{16}\text{O} \text{ }^{16}\text{O}$, $^{12}\text{C} \text{ }^{16}\text{O} \text{ }^{17}\text{O}$), and 46 ($^{12}\text{C} \text{ }^{16}\text{O} \text{ }^{18}\text{O}$, $^{13}\text{C} \text{ }^{16}\text{O} \text{ }^{17}\text{O}$, $^{12}\text{C} \text{ }^{17}\text{O} \text{ }^{17}\text{O}$). These masses correspond to the most abundant isotopologues of CO_2 formed during the combustion or chemical oxidation of OM. Other isotopologues of CO_2 exist yet their relative abundance compared to those with mass 44, 45 and 46 is minor. The use of carbon stable isotopes is not limited to the environmental sciences and has become increasing in the context of forensic science as well. Differences in ^{13}C content in natural and synthetic steroids has allowed IRMS analysis to become the gold standard for confirming whether or not athletes are using banned steroids due to differences in endogenous and exogenous steroid ^{13}C content (Ouellet et al., 2013).

In this thesis we will present bulk stable isotope data generated using two separate peripherals coupled to an IRMS, elemental analysis (EA) for solid samples and dissolved organic carbon (DOC) for the determination of carbon in aqueous solutions. A central theme of the work

presented in this thesis is taking a strong analytical approach, ensuring that the data is presented with a realistic degree of analytical precision and accuracy, something that is lacking in a large portion of the stable isotope literature. Specifically in the context of stable isotope analysis on DOC, where there is a serious lack of consensus reference material, and relatively recent interlaboratory comparison studies have presented data with problematically large differences in measured $\delta^{13}\text{C}$ signatures. Many publications will provide accuracy and precision measurements based off of repeated measurements of standards of known isotopic composition, which may be sufficient when the samples are matrix matched, yet for the analysis of samples from a complex matrix such as seawater, or waters along an estuarine mixing zone where salinity and dissolved ion concentrations can vary considerably the samples must be run with enough replicates for the data to be useful/convincing.

EA-IRMS has been a staple of geochemical isotope measurements for decades and involves the combustion of the organic matter in a given sample, followed by a reduction column, several chemical traps to remove unwanted contaminants and a packed GC column to chromatographically separate the combustion products with the goal of maintaining a constant ionization efficiency for the species of interest. Even though the masses of interest are based on specific isotopologues during IRMS analysis, without the additional chromatography several species such as N_2 and CO_2 would reach the ionization source of the IRMS simultaneously. Varying amounts of either species would significantly impact the ionization efficiency of the other species regardless, altering the final measured isotope signature. For the coupled DOC-IRMS analysis described in this thesis no chromatography is used in order to separate the combustion products of interest. Instead a chemical trap which sorbs CO_2 at room temperature and rapidly releases it when heated to $250\text{ }^\circ\text{C}$ serving a dual purpose, to exchange the carrier gas

between the DOC analyzer which uses O₂ to a more IRMS suitable carrier gas (He) while also allowing us to separate the carbon combustion products from other species generated during the combustion of OM.

1.5. X-ray Absorption Spectroscopy

On a fundamental level, X-ray absorption spectroscopy involves the excitation of an electron from its ground state to a continuum state. Ionization of an electron to a photoelectron occurs when an atom is bombarded by a photon of energy equal to that of the electrons initial binding energy (Lehman et al., 2009). More interestingly, when an atom is subjected to photons with energies lower than the electron binding energy, they are promoted to a partially filled or unfilled orbitals. Third generation synchrotron radiation sources, such as the Canadian Light Source (CLS) laboratory in Saskatoon, have provided the infrastructure and instrumentation necessary to improve upon the original prototype soft microscopy beamline built at the Advanced Light Source at Berkeley (Kaznacheyev et al., 2007). The increased beamline stability, higher brightness and higher energy fluxes created at these state-of-the-art facilities provide the energy and spatial resolution necessary to make techniques such as STXM applicable to the highly complex, chemically re-worked samples with low C contents that are typical of environmental sciences (e.g. soils, particulate OM (Lehmann et al., 2009) and even extraterrestrial meteorite samples (Gregorio et al., 2011)).

The STXM end-station created for the soft microscopy beamline at the CLS passes the synchrotron generated radiation through a series of lenses acting as a microscope, focusing the beam to a minimum spot size of 30 nm (Kaznacheyev et al., 2004; Kaznacheyev et al., 2007). The combination of tiny spot size and high magnification makes this technique ideal for measuring micro- and nano-scale samples by capturing actual microscopic images of the sediment alongside

X-ray absorption spectra with a high spatial resolution leading to the collection of large stacks of images and NEXAFS spectra every 35 nm during sample scanning.

1.6. NEXAFS Spectromicroscopy for Sediment Analysis

The use of NEXAFS spectromicroscopy in determining the speciation of different elements of interest is based on the Beer-Lamberts law for X-ray spectroscopy,

$$I = I_0 e^{-\mu t}$$

where I_0 and I are the intensities of the incident photon hitting the sample and the energy transmitted through the sample, respectively, μ is the absorption coefficient for a given species and t is the sample thickness (Lehmann et al., 2009). Each collected spectrum normalizes the measured intensity of the transmitted photons to that of the photons reaching the detector without passing through the sample, thus correcting for any fluctuation in beam energy during the analysis. When an atom is subjected to energies greater than or equal to the binding energy of an electron from a given shell, it is ionized, but at energies slightly below this energy level the electron can be promoted to unbound molecular orbitals (Lehmann et al., 2009). The exact energy at which these transitions occur is dependent on the species and transitions involved. The shape and energy at which the absorption bands are observed can be used in comparison to the NEXAFS spectra of known standards in order to determine the speciation for a given element.

We have used X-ray absorption spectra from the C and Fe K-edge transitions and Fe L-edge transitions in order to determine the speciation of C and the oxidation state of Fe. It is important to keep in mind that not only do these technique provides X-ray absorption spectra and overlays these spectra onto actual images of the sediment particles, allowing for the discussion of each element's spatial relationship with the mineral matrix.

1.7. Arrangement of Thesis

This work is a compilation of 5 manuscripts (3 published, 2 to be submitted for publication) followed by some perspectives on the fate of organic matter along the aquatic continuum taking into consideration the sum of the presented work. Each chapter is presented in a similar fashion, with the figures and tables embedded within the text and all supplementary material being found as appendices.

Chapter 2 (Measuring the $\delta^{13}\text{C}$ Signature of Dissolved Organic Carbon: An Inter-laboratory Proficiency Test – to be submitted in *Rapid Communications in Mass Spectrometry*) begins by presenting the results from an interlaboratory comparison study designed to evaluate the modern methodologies used for the analysis of carbon stable isotope signatures of dissolved organic carbon. The high-temperature catalytic oxidation method of DOC determination was most suited for the analysis of saltwater samples. The carbon stable isotope results for dissolved OM presented in this thesis come from samples collected along the aquatic continuum covering the transition from fresh to salty waters. As such the high-temperature catalytic oxidation method was used for all $\delta^{13}\text{C}$ -DOC analysis presented in the following chapters.

Chapter 3 (Stable Isotope Analysis of Dissolved Organic Carbon in Canada's Eastern Coastal Waters, accepted for publication in *Limnology and Oceanography*) presents the most comprehensive $\delta^{13}\text{C}$ -DOC dataset along Canada's coastal waters. Focussing primarily on tracking the fate of terrestrial and marine organic matter along the St. Lawrence Estuary and Gulf as well as along the east coast of Labrador and finally across the Hudson Strait to the north of Quebec. The primary goal here was to evaluate the processes which affect the

preservation/degradation as OM is transported both across the estuary as well as down the water column. This chapter is accepted for publication in *Limnology and Oceanography*.

Chapter 4: The Role of Iron in the Diagenesis of Organic Carbon and Nitrogen in Sediments: A Long-term Incubation Experiment, *Marine Chemistry*. **162**, 1–9 (2014)) focussed on using carbon stable isotope signatures to track the fate of a ^{13}C depleted OM tracer over the course of a long-term incubation. Using the slurry incubation setup described in the manuscript we were also able to evaluate the effect of oscillating redox conditions and the precipitation of iron oxides on the transport of natural OM from the dissolved phase to solid phase sediments. This study presents the initial building blocks for our hypothesis regarding the synergistic ferric carbon transport mechanism which is explored more fully in Chapter 5.

Chapter 5: Preservation of Organic Matter in Marine Sediments by Inner-sphere Interactions with Reactive Iron was published in *Scientific Reports* in March of 2017 and presents the crux of this thesis. We present a combination of synchrotron X-ray data collected on intact sediment particles in order to demonstrate nano-scale co-localization of OC and Fe in sediments from around the globe. Additionally, we were able to probe the mechanism by which OM interacts with iron oxides in these sediments, combining X-ray absorption spectroscopy with wet chemical mass balance experiments to show that inner-sphere covalent interactions between OM and iron oxides play a critical role in stabilizing both OM and iron during its transport through the sediment oxic/anoxic interface.

Chapter 6: Redox Conditions Influence the Chemical Composition of Iron-Associated Organic Matter in Boreal Lake Sediments: a Synchrotron-Based NEXAFS Study – (to be submitted for publication in *Geochimica et Cosmochimica Acta*) further demonstrates the importance of OC and Fe interactions to the preservation of OM, this time in lacustrine sediments. Here we present

C and Fe X-ray absorption spectra and images for samples coming from surface sediments from two Basins of the same lake with contrasting oxygen exposure regimes.

Chapter 2: Measuring the $\delta^{13}\text{C}$ Signature of Dissolved Organic Carbon: An Inter-laboratory Proficiency Test

Andrew Barber¹ and Yves G  linas^{1*}

¹GEOTOP and the Department of Chemistry and Biochemistry, Concordia University, 7141 Sherbrooke West, Montr  al, Quebec, Canada, H4B 1R6.

*Correspondence to:

Yves G  linas

E-mail: yves.gelinas@concordia.ca

Phone: 514-848-2424 (3337)

2.1 Abstract

The quantitation of dissolved organic carbon (DOC) has long been a difficult measurement in organic geochemistry and only through community driven international inter-laboratory proficiency tests were researchers able to evaluate the accuracy and precision of the different analytical techniques available for this type of measurement. With the growing number of publications now claiming to be able to accurately and precisely determine the carbon stable isotope signature ($\delta^{13}\text{C}$) of DOC, the need for another series of proficiency tests is clear. With the goal of comparing the common $\delta^{13}\text{C}$ -DOC analysis methods, a total of 16 laboratories were shipped a series of freshwater and saline DOC samples with varying $\delta^{13}\text{C}$ signatures. Included within the sample set was a series of simple molecule (potassium hydrogen phthalate) and complex organic matter (OM) mixtures (marine and lake ultrafiltered DOM) with known $\delta^{13}\text{C}$ signatures. Overall, the High Temperature Catalytic Oxidation (HTCO) and bulk Wet Chemical Oxidation (WCO) methods accurately and precisely determine the $\delta^{13}\text{C}$ signature for simple molecule and complex terrestrial organic matter samples. Meanwhile, the lower sample volume Liquid Chromatography Wet Chemical Oxidation (LC-WCO) method was able to determine the $\delta^{13}\text{C}$ signature with a similar variance as the other two methods, but for complex or low concentration samples there was a 3-fold increase in standard deviation relative to the HTCO and WCO methods. These complex, low concentration samples are typical of natural samples and as such the only acceptable analysis methods for the determination of the $\delta^{13}\text{C}$ -DOC would be the HTCO and bulk WCO methods.

Keywords: $\delta^{13}\text{C}$, dissolved organic carbon, inter-laboratory comparison, proficiency test

2.2. Introduction

Historically, the measurement of the dissolved organic carbon (DOC) content in natural waters has been difficult, requiring long reaction times and large sample volumes of up to 10 L (Hansell and Carlson, 2014). A common thread in all modern DOC determination methods involves the oxidation of organic carbon to CO₂, typically through the addition of chemical oxidants, sample irradiation or high temperature combustion. Over 100 years of DOC concentration measurements exists, yet much of the early research has now been found to be erroneous due to poor sampling techniques and a lack of analytical precision and accuracy. In fact several studies the 1970-80's analyzed similar, natural abundance DOC samples but the results varied by a factor of 3, grossly overestimating open ocean carbon budgets(Williams, 1975; Sugimura and Suzuki, 1988; Hansell and Carlson, 2014). These discrepancies in reported DOC concentrations gave rise to a series of inter-laboratory comparison studies to determine which methods were capable of accurately and precisely making these types of measurements (Sharp, 1997; Sharp et al., 2002).

From this series of DOC concentration proficiency tests the major sources of uncertainty for DOC quantitation include various blanks (system blank, water blank), oxidation interferences and the lack of stable, soluble reference materials (Sharp et al., 2002). Poorly constrained blank contributions led to larger uncertainty and poor reproducibility, particularly when coupled with stable isotope analysis, where measured the stable isotope signature is the combined stable isotope signature of the sample and blanks (Lalonde et al., 2014a). Matrix effects arise when analyzing saline samples, limiting the throughput of these analysis methods by causing salt buildup and generating corrosive Cl⁻. This not only corrodes the inner workings of these instrument but can also interfere with analyte oxidation through competitive inhibition of the catalyst/reactants leading to faulty stable isotope values (Aiken, 1992). Each of the widely-used DOC determination methods are more/less susceptible to each of these drawbacks (for example high temperature combustion units are more likely to be inhibited by salt buildup, while chemical oxidation units are more susceptible to oxidation inhibitors).

With the increasing interest in carbon stable isotope analysis, several methods of coupling [DOC] determination to Isotope Ratio Mass Spectrometers (IRMS) and Cavity Ring Down Spectrometers (CRDS) have been published over the last decade (Bouillon et al., 2006; Albéric, 2011; Hartland et al., 2012; Federherr et al., 2014; Lalonde et al., 2014a). These measure the $^{13}\text{C}/^{12}\text{C}$ ratio of the CO_2 generated from the oxidation of the dissolved organic matter, in reference to an internationally certified standard (Vienna Pee Dee Belimnite) using the following formulae (Muccio and Jackson, 2009):

$$^{13}\text{R (Unitless)} = ^{13}\text{C}/^{12}\text{C} \quad (\text{Eq. 2-1})$$

$$\delta^{13}\text{C (‰)} = (^{13}\text{R}_{\text{Sample}}/^{13}\text{R}_{\text{Reference}} - 1) \times 1000 \quad (\text{Eq. 2-2})$$

The factor driving this type of research and emphasis on the coupling of DOC analysis instruments and stable isotope detector systems is the increased interest in the global carbon cycle, in the context of anthropogenic climate change. More specifically, using the $\delta^{13}\text{C}$ signature of natural samples as a source indicator to evaluate which pools in the global carbon cycle act as sources vs sinks of carbon (Muccio and Jackson, 2009; Lalonde et al., 2014b). Also, with the advent of these novel determination methods there has been an increase in the use of carbon stable isotopes in $\delta^{13}\text{C}$ -DOC enriched labelling studies, where the fate of the added tracer can be followed throughout the course of an incubation (Barber et al., 2014) or used to determine novel biosynthetic pathways for the production of biologically relevant molecules (Schierbeek et al., 2007). Despite several publications using stable carbon isotope DOC values to draw important conclusions with regards to global carbon dynamics (Bianchi et al., 1997; Ouellet et al., 2012; Barber et al., 2014; Lalonde et al., 2014b), no consensus reference material exists in order to adequately compare the response of the different instruments used for this analysis. This study will aim at addressing this issue through the analysis of identical samples using the most commonly used carbon stable isotope determination methods.

Without the availability of a soluble organic carbon stable isotope reference material it has been difficult to evaluate the analytical limitations of these novel analysis techniques, and to date the published

proficiency tests have had too few participants (2 DOC participants only) (Geldern et al., 2013), to adequately draw any statistically useful comparisons between the different methods. All of this demonstrates the need for a broad scale community wide inter-laboratory study such as the one presented here.

A call for participants for this $\delta^{13}\text{C}$ -DOC proficiency test was initially issued in August of 2012 with the goal of evaluating the accuracy and precision of the different methodologies used for $\delta^{13}\text{C}$ -DOC analysis as well as to provide analyst specific reports comparing their provided results to the consensus values determined by each method included in this study. Each analyst was provided a series of freshwater and saline samples (saline samples were only included if requested) with varying DOC concentrations, organic carbon sources, and expected $\delta^{13}\text{C}$ -DOC signatures.

A study with a similar purpose but with only a total of 5 participating labs primarily focussed on the determination of $\delta^{13}\text{C}$ for dissolved *inorganic* carbon also discussed the ability of 2 of the participating labs to measure the $\delta^{13}\text{C}$ -DOC (Geldern et al., 2013). Although similar in scope and a good demonstration of why these types of ring tests are required, the low number of participants and lack of representation for several DOC conversion methods discussed below shows why these studies must be repeated and ideally a consensus reference material can be obtained for future analysts.

2.3. Materials and Methods

2.3.1. Sample Preparation:

A series of freshwater (9) samples with varying organic matter sources and concentrations were shipped blind to each participant as requested. All samples were acidified to a pH of ~ 2 using HCl or H_3PO_4 , as requested, and stored refrigerated at 4°C in the dark prior to shipment. Included within the freshwater dataset was a 4-point calibration curve using potassium hydrogen phthalate (KHP) as well as both marine and lake Ultra-filtered Dissolved Organic Matter (UDOM) dissolved/diluted in 18.2Ω Milli-Q water (Table 2-1). The two remaining freshwater samples (Sample ID 8 and 9) consisted of different organic

matter sources with a wide range of $\delta^{13}\text{C}$ signatures and no expected value was determined for this complex mixture. Analysts were forewarned that these would be enriched in ^{13}C relative to Pee Dee Belemnite in order to allow them to use an appropriate set of standards with $\delta^{13}\text{C}$ signatures similar to that of the enriched compounds, if available.

For the labs that requested the saline samples, a series of 7 saltwater samples were also included. These were created in a similar fashion by spiking known amounts of either KHP, UDOM or the ^{13}C enriched complex OM mixture to deep lower St. Lawrence Estuary water with a salinity of 34.5 PSU. Finally, included in the saltwater data set was an ampoule of Deep Florida Straight water collected as part of the DOC consensus reference material program run by the Hansel lab (University of Miami, <http://yyy.rsmas.miami.edu/groups/biogeochem/CRM.html>) with the goal of obtaining a consensus $\delta^{13}\text{C}$ -DOC value.

Table 2-1: List of Sample Identities and Expected DOC Concentration

Sample ID	Organic Matter Source	Expected DOC Concentration (μM)
1	Potassium Hydrogen Phthalate (KHP)	130
2	Lake UDOM	69
3	Potassium Hydrogen Phthalate	570
4	Lake UDOM	358
5	Potassium Hydrogen Phthalate	782
6	Marine UDOM	136
7	Potassium Hydrogen Phthalate	84
8	Lake UDOM + ^{13}C Enriched OM	NA
9	Lake UDOM + ^{13}C Enriched OM	NA
10	Lake UDOM + ^{13}C Enriched OM	NA
11	Lake UDOM	201
12	Deep St. Lawrence Estuary Water	57
13	Marine UDOM	236
14	Lake UDOM	569
15	Lake UDOM + ^{13}C Enriched Water	NA
Ampoule	Florida Straight Water (CRM)	41-44*

All expected concentrations were determined by the mass of the analyte/solution dissolved in a known mass of water. * This value was obtained from the Consensus Reference Material program from Hansel Lab.

2.3.2. Sample Pre-treatment:

In order to prevent over-estimation of the DOC concentrations, the dissolved inorganic carbon (DIC) in the sample must be removed via either offline or online sparging of the samples. DIC Purging is often done using the peripheral carrier gas, in this case either He or O₂ and typical sparging times varied between 1 and 4 minutes for the different labs. Online sparging allows for the dual determination of both

the DIC and DOC content for the samples but was not often used in this study as it increases total run times compared to offline sparging and analysts were only asked to report the $\delta^{13}\text{C}$ -DOC values.

2.3.3. High-Temperature Catalytic Oxidation (HTCO):

A total of 5 labs used high temperature combustion units where the dissolved organic carbon was combusted at temperatures between round 680-850°C in the presence of a platinum catalyst using O_2 as a carrier gas (Federherr et al., 2014; Lalonde et al., 2014a). The oxygen carrier gas was not amenable to IRMS analysis, thus a chemical trap was used in order to switch the carrier gas to helium in order to analyze the isotopic signature of the CO_2 produced from the DOC combustion. The sample injection volumes used for these analyses ranged between 0.5 and 3.0 mL of water.

2.3.4. Wet Chemical Oxidation (WCO):

A total of 6 labs used wet chemical oxidation units, converting the DOC to CO_2 through a reaction between the DOC in the sample and $\text{Na}_2\text{S}_2\text{O}_4$ plus H_3PO_4 in a UV irradiated reaction chamber. In order for the reaction to proceed to completion in a timely manner for high throughput analysis the solutions must be heated to 100°C and the persulfate solution must be “washed” of potential contaminants prior to use using UV radiation (Bouillon et al., 2006; Osburn and St-Jean, 2007a). Sample injection volumes varied between 1 and 15 mL depending on the analyst.

2.3.5. Liquid-Chromatography Wet Chemical Oxidation (LC-WCO):

Only 3 labs used a modified LC-WCO setup with an online reaction chamber where the DOC in the sample is converted to CO_2 via the same mechanism as in the WCO method. Although the reaction remains the same, the volumes of sample and reagents are considerably smaller, with sample injection volumes between 50 and 200 μL . The acidified persulfate solution chemically oxidizes the DOC in a reaction chamber kept at around 100 °C and the acidified reactants are pumped through the system at a flow rate of 120 $\mu\text{L}/\text{min}$ (Albéric, 2011).

2.3.6. Statistical Methodology:

Analysts were requested to provide the data as if they were part of their routine service lab analysis. As such the majority of all participants did not provide the raw data but rather provided an average measured $\delta^{13}\text{C}$ and standard deviation for each of the samples that they were capable of analyzing/willing to provide data for. Upon receipt of the datasets, following the guidelines set by the Institute for Interlaboratory Studies (Starink et al., 2014) the data for each sample was subjected to the Lilliefors normality test (Lilliefors, 1967; Molin and Abdi, 1998) prior to any subsequent statistical analysis.

The freshwater data provided for the 3 major methods (HTCO, WCO and LC-WCO) was found to be normally distributed. As such the different methodologies were compared by using their mean, standard deviation, confidence intervals ($\alpha=0.05$) and finally t-tests. The latter was used in order to determine whether the reported values for each method differed significantly from the expected values when available.

$$\text{Confidence Interval} = \bar{X} \mp t_{\text{crit}} \left(\frac{\sigma}{\sqrt{N}} \right) \quad (\text{Eq. 2-3})$$

$$t = (\bar{X} - \mu) / \left(\frac{\sigma}{\sqrt{N}} \right) \quad (\text{Eq. 2-4})$$

Where μ is the expected/true mean value, N is the number of observations, x is the measured $\delta^{13}\text{C}$ signature, t_{crit} is the critical t value at a significance level of 95%. In order to take into consideration each labs reported uncertainty the σ values used for are actually the pooled standard deviations, calculated using the following formula:

$$\text{Pooled Standard Deviation} = \sqrt{\frac{(N_1-1)S_1^2 + (N_2-1)S_2^2 + \dots + (N_i-1)S_i^2}{(N_1 + N_2 + \dots + N_i - i)}} \quad (\text{Eq. 2-5})$$

Where S_i and N_i are the standard deviation and number of replicates reported for each of the i^{th} labs. This ensures that the reported analyst standard deviations are weighted according to the number of acquired

replicates. The confidence intervals provides a visual aid for a quick comparison of the different methodologies (Fig. 2-1 and 2-2), while using Student's t-test for the comparison with a known/expected value will allowed us to evaluate the statistical significance of any differences in the measured *vs.* theoretical $\delta^{13}\text{C}$ for each method. Note that several methods included in the study did not have the required number of observations per sample in order to perform these statistical calculations. As such the aforementioned statistical methods only apply to the HTCO, WCO and LC-WCO methods.

2.4. Results:

2.4.1. Freshwater Samples

Samples 1, 3, 5 and 7 where 18 Ω Milli-Q water was spiked with known quantities of KHP with a reference isotopic signature of -28.16 ± 0.10 ‰, as determined independently through Elemental Analysis-IRMS (EA-IRMS) by 3 different stable isotope labs. From this set of 4 solutions we can critically evaluate the practical limitations for the different analysis methods. Across the three methods

used in this study, for simple molecule freshwater samples with DOC concentrations above $\sim 84 \mu\text{M}$, the

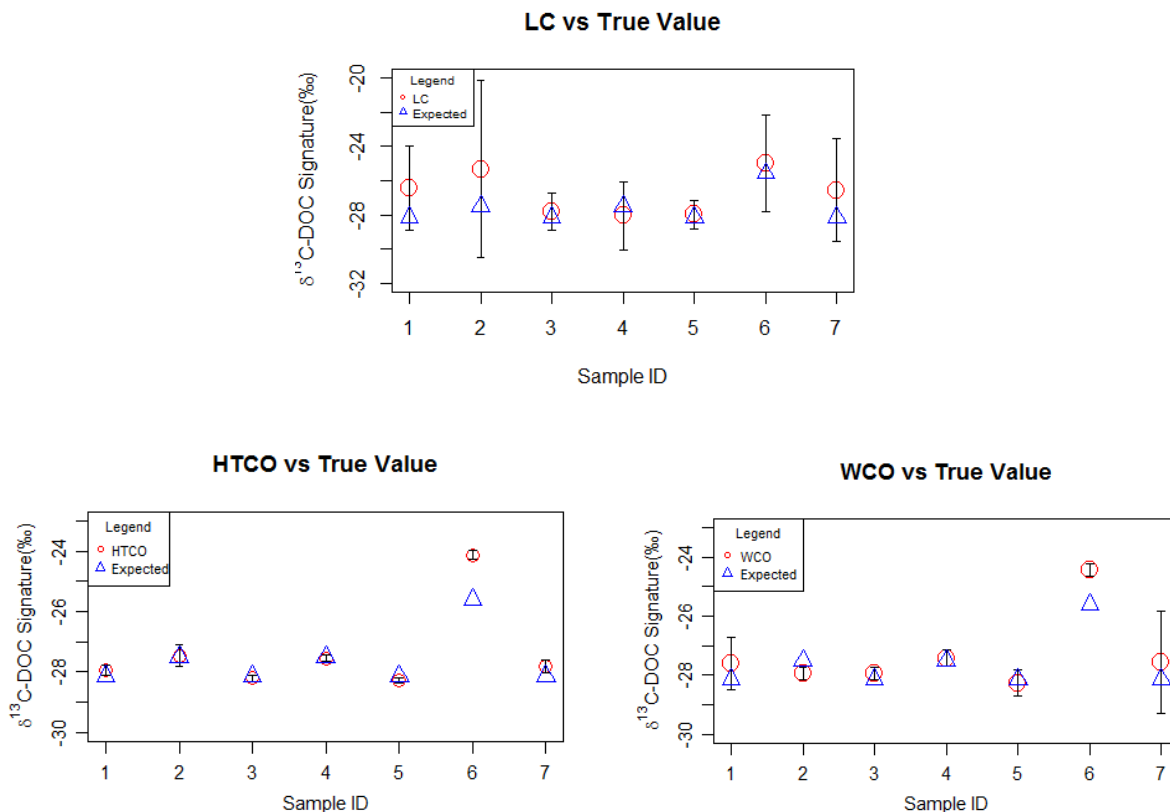


Figure 2-1: Expected and Measured $\delta^{13}\text{C}$ signatures for the Freshwater Samples Measured (circles) and expected (triangles) $\delta^{13}\text{C}$ signature for the set of the first 7 freshwater samples for the A) WCO (N=6), B) HTCO (N=5) and C) LC-WCO (N=3) DOC determination methods. Error bars represent the confidence interval for each sample with a significance level of 95%. Expected values were determined by EA-IRMS analysis. Note the scale change for the y-axis.

measured isotopic signatures were not statistically significantly different ($\alpha=0.05$) from the expected mean value (Fig. 2-1, Samples 1, 3, 5 and 7) using Student's t-test for the comparison of means to a known value.

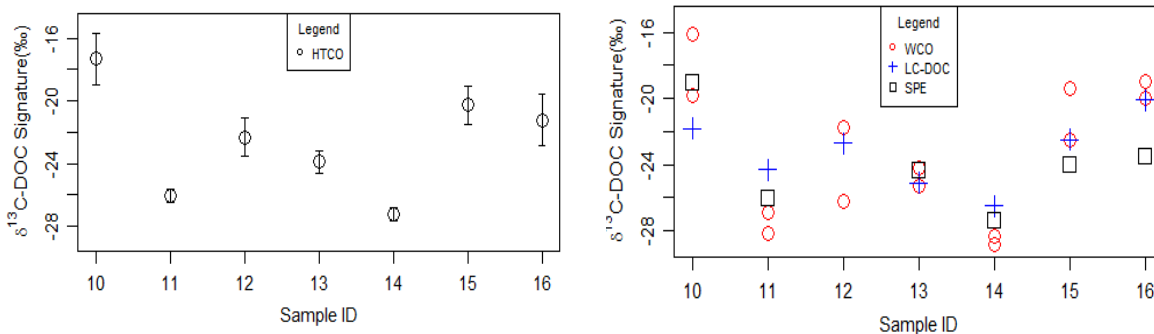


Figure 2-2: Expected and measured $\delta^{13}\text{C}$ signatures for the saline samples

Measured $\delta^{13}\text{C}$ signature for the set of the first saline samples analyzed by the A) HTCO method (N=5) B) WCO, LC-WCO and SPE methods. Error bars represent the confidence interval for each sample with a significance level of 95%. Note that in B each point represents one data point since there were not enough replicates to statistically compare these methods.

Several freshwater solutions were spiked with ultra-filtered dissolved organic matter (UDOM) from either Lake Brock (QC, Canada) for samples 2 and 4 or from the mostly marine Station 20 of the Lower St. Lawrence Estuary (QC, Canada) for sample 6. $\delta^{13}\text{C}$ signatures for both UDOM sources were determined by EA-IRMS analysis in three participating laboratories prior to the beginning of this ring test. In line with the results for the simple molecule solutions presented above the measured $\delta^{13}\text{C}$ for the lacustrine UDOM samples were not statistically different ($\alpha=0.05$) from the expected value for all three compared methods using Student's t-test for the comparison of means to a known value.

Interestingly despite not being statistically significantly different it should be noted that for samples with a DOC concentration lower than $\sim 400 \mu\text{M}$ carbon there was a large increase in variance for the LC-WCO method (Fig. 2-3). This can be visualized in Figure 2-1 as the overall range of the confidence intervals as well as in Fig. 2-3, which demonstrates the increase in standard deviation across all methods as the concentration of DOC decreases. From these standard deviations, there was a clear decrease in analytical

precision for the lower concentration samples across all methods owing to the larger reported variance for these samples (independent of sample complexity). This phenomenon was exacerbated for the low concentration more complex OM, particularly using the LC-WCO methods further demonstrating the limitations of this technique (Fig. 2-1 and 2-3). In fact there was a 3-fold increase in standard deviation for the 69 μM (Sample 2) compared to the 358 μM (Sample 4) solution using this technique.

Finally, the reported $\delta^{13}\text{C}$ signatures for the marine UDOM sample (6) for the WCO and HTC methods were found to be statistically significantly different compared the expected $\delta^{13}\text{C}$ value ($\alpha=0.05$). Although there was no statistically significant difference between the expected value and the reported values for the LC-DOC method, this was driven once again by the larger variance reported for these samples and can be visualized by the range of the confidence intervals for these samples (Fig. 2-1). Future studies with similar sample types would be required in order to identify what is causing the difference observed for this sample. Note that for the samples enriched in $\delta^{13}\text{C}$ (Samples 8 and 9) no useful statistical comparison could be done due to the irreproducibility of the measurements across the different methods and the lack of an expected signature. Further studies would be required to better evaluate the $\delta^{13}\text{C}$ -DOC community's ability to measure enriched organic matter samples.

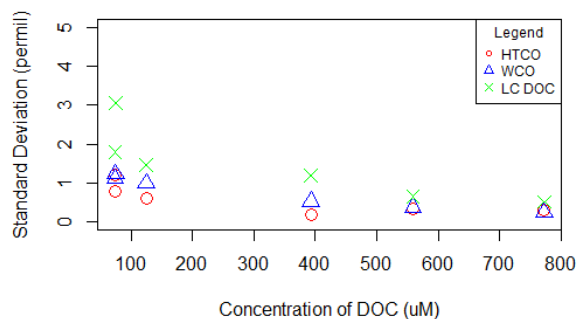


Figure 2-3: The Increase in Standard Deviation with Decreasing DOC Concentration
Measured standard deviation for the first 7 freshwater samples with the sample concentration.

2.4.2. Saltwater Analysis:

A total of 9 labs provided data for the saltwater sample set. Over half (5 of 9) analysis sets were performed with high-temperature combustion being as the method of DOC conversion to CO₂. Other methods for which saltwater data was reported included the WCO (N=2), LC-WCO (N=1) and finally using EA-IRMS after passing the sample through a solid phase extraction column (N=1). With this in mind, only the HTC data was analyzed using the statistical methods mentioned above. Samples 11, 13 and 14 all have relatively small 95% confidence intervals (0.85, 1.38 and 0.86 ‰ respectively) compared to the remaining saline samples. Clearly this is once again due to the DOC concentration of these given solutions, with sample 11 being the lowest of the three at 201 μM. The remaining, low DOC content samples have confidence intervals that encompass a range of 0.6 to 3.3 ‰ (Fig. 2-1). A similar trend can be observed for the other samples as well, yet no statistically significant conclusions could be drawn due to the low number of observations for each method (Fig. 2-2).

Samples 12 and 16 were low concentration seawater samples without any additional organic matter sources with sample 12 being a blind sample consisting of water from the St. Lawrence Estuary (~300 m depth) and sample 16 being a labelled ampoule of deep Florida Strait water from the Hansel CRM program.

The low DOC concentration relative to the high salt content of these samples make them among the most difficult natural samples to analyze. Previous studies have reported carbon stable isotopic signatures for similar marine DOC samples (Bauer et al., 2002; Bouillon et al., 2006; Federherr et al., 2014), yet no consensus $\delta^{13}\text{C}$ -DOC reference solutions are currently available. In total the deep Florida Strait water was measured by 7 analysts with an average $\delta^{13}\text{C}$ -DOC signature of -20.9 ‰ (± 1.74) compared to the St. Lawrence Estuary sample, which had an average $\delta^{13}\text{C}$ -DOC signature of -22.8 ‰ (± 1.7). Interestingly, from a geochemical perspective these signatures are similar to what has been predicted for deep seawater (Bauer et al., 2002), with the more marine sample having a slightly enriched signature relative to the estuarine mixing zone samples, due to the difference in source material used in the formation of the

organic matter. The previous $\delta^{13}\text{C}$ -DOC interlaboratory comparison study involving only 2 labs obtained values of -9.3 and -21.0‰ (Geldern et al., 2013) for the seawater samples and reported a much larger spread for the other samples (up to 20‰ spread). This study benefits from the larger number of participants and this could explain the overall improvement in apparent analytical precision and accuracy relative to the aforementioned study, where no study wide statistics could be performed with an N of 2.

Although further repeated analysis would be required for establishing either of these samples as consensus reference material we encourage novel and experienced analysts alike to test the accuracy of their instrument using samples such as these until a proper dissolved carbon isotope standard becomes readily available.

2.5. Conclusions

2.5.1. Decrease in precision with decreasing DOC concentration

Clearly, there was an increase in estimated variance for the low concentration freshwater samples (Fig. 2-3). This was as expected, since low concentration samples will tend to have a higher blank water and system blank contribution relative to the contribution from the sample. Although mathematical mass balance equations exist which would allow for proper blank subtraction (Federherr et al., 2014; Lalonde et al., 2014a), this equation requires that the isotopic signature of the blanks to be determined. This measurement pushes the limits of modern day IRMS and CRDS detection limits, and is most likely the dominant factor that contributes to the increased uncertainty for low concentration measurements. For the saline samples the issue regarding low concentration samples is exacerbated by the presence of interferants at concentrations much higher than that of the analyte.

2.5.2. Decrease in precision for complex OM sources

From the size/range of the confidence intervals in Figure 1 (specifically Samples 2 and 6) compared to those for the simple molecule samples with comparable concentrations, decrease in precision for more complex samples (most noticeably for the LC and WCO methods) was found. This likely arises due to

either a lack of sample homogeneity (due to the low injection volumes used for the LC method) or from incomplete persulfate oxidation of the organic matter. Complex organic matter sources such as UDOM have a wide range of reactivities from highly labile (easily oxidized) to more refractory (harder to oxidize) components. A possible solution for the latter case would be an addition of excess oxidizing agent, or increasing the reaction time to ensure full oxidation of the sample. In the case of the LC-WCO method, perhaps increasing the number of replicate injections would provide a more representative sample of the actual population. Although the minimal sample volume required for this type of analysis is typically considered an advantage, the absolute amount of carbon being analyzed makes it difficult to determine its isotopic signature. Several participants using wet oxidation methods preferred not to provide data for the saline samples, as Cl^- ions are known to compete for the oxidant with the oxidant, persulfate, and competes with the analyte of interest (DOC)(Aiken, 1992).

2.5.3. Community Wide Repercussions:

Despite the LC-WCO method being a published method which has been used for the stable isotope determination of low concentration samples, this method requires additional optimization in order to be comparable in terms of accuracy and precision to the other methods presented above. Overall, another round robin proficiency test would now be required in order to better determine the threshold limit at which there is a rapid decrease in analytical precision using samples with a concentration ranging from ~ 40 to ~ 400 μM . Additionally, more work is needed in order to improve the current analysis methods in order to be able to analyze samples which are enriched in ^{13}C (samples 8 and 9) which were not included in any statistical analysis due to the data not being normally distributed. This second study would also try to include more participants and natural (non OM spiked samples) in order to further establish a saline $\delta^{13}\text{C}$ consensus reference material as was initially intended in this study. For now, we suggest using either the deep Florida Strait water from the Hansel lab as purchasable reference material in conjunction with the isotope data presented here.

Chapter 3: Stable Isotope Analysis of Dissolved Organic Carbon in Canada's Eastern Coastal Waters

Andrew Barber¹, Maude Sirois², Gwenaëlle Chaillou², Yves Gélinas¹

¹GEOTOP and the Department of Chemistry and Biochemistry, Concordia University, 7141
Sherbrooke West, Montréal, Quebec, Canada, H4B 1R6.

²Canadian Research Chair on Geochemistry of Coastal Hydrogeosystems, Université du Québec
à Rimouski, 300 Allée des Ursulines, Rimouski, Quebec, Canada, G5L 3A1.

*Correspondence to:

Yves Gélinas

E-mail: yves.gelinas@concordia.ca

Phone: 514-848-2424 (3337)

3.1. Abstract

The application of carbon stable isotope analysis of dissolved organic carbon ($\delta^{13}\text{C}$ -DOC) from natural seawater has been limited owing to the inherent difficulty of such analysis, with order of magnitude differences in interfering ions and analyte concentrations. High temperature catalytic oxidation allows for the attenuation of these interferences by precipitation of inorganic ions on quartz chips upstream from the oxidation catalyst. Using a chemical trap, the OI 1030C combustion DOC analyzer unit can be coupled to an IRMS, allowing for the analysis of low DOC content saline waters with relatively high throughput. The analytical limitations and large water volumes traditionally required for these types of analyses have prevented any large-scale $\delta^{13}\text{C}$ -DOC studies.

Here we present $\delta^{13}\text{C}$ -DOC signatures for surface and bottom waters obtained along Canada's East Coast. Included in the study are samples from the Esquiman channel (between Newfoundland and Labrador), Lake Melville, the Saglek and Nachvak Fjords, the Hudson Strait and finally covering the salinity gradient across the St. Lawrence Estuary and Gulf. Measured $\delta^{13}\text{C}$ -DOC signatures ranged from predominantly marine values of $-19.9 \pm 0.3 \text{ ‰}$ (vs. VPDB) off the coast of Newfoundland to predominantly terrestrial signatures of $-26.9 \pm 0.1 \text{ ‰}$ in Lake Melville. We observed a large spread in $\delta^{13}\text{C}$ -DOC signatures for samples with a salinity of ≈ 35 between -19.9 and -23.3 ‰ demonstrating the difficulty associated to selecting a marine end-member to be used in stable isotope mixing models to determine the fate of organic matter along the freshwater – marine continuum.

3.2. Introduction

Dissolved organic carbon (DOC), ubiquitous in all marine and lacustrine environments, is one of the largest pools of organic carbon on the planet, comparable in magnitude to the atmospheric CO₂ pool. Virtually all natural waters contain some form of DOC, ranging from highly reactive freshly produced DOC to low reactivity recalcitrant DOC escaping remineralization for upwards of 6000 years (Druffel and Williams, 1992). This broad range of DOC composition and reactivity can be encountered in spatially limited areas such as the transition zones between terrestrial and marine environments, which are a key component of the hydrological and biogeochemical continuum linking surface waters and the ocean (Ward et al., 2017). Organic matter is extensively reworked along this continuum through biotic processes such as bacterial degradation, as well as by abiotic processes such as photo-oxidation, co-precipitation alongside inorganic minerals and salting out. These fresh to saline transition zones are particularly interesting in terms of carbon sequestration as they have been shown to act as both sources and sinks for organic carbon and atmospheric CO₂ (Cai, 2011; Laruelle et al., 2015).

The advent of high precision and accuracy DOC determination instruments has allowed for more complete oceanic and riverine carbon budgets, yet DOC concentration measurements alone are insufficient for tracking the fate of organic matter. A series of DOC concentration inter-laboratory comparison studies (ring-tests) was launched to better explain the discrepancy in reported DOC concentrations for similar samples (Sharp, 1997; Sharp et al., 2002). The unavailability of organic carbon free water, insufficient blank corrections, and method artifacts (such as the inadvertent generation of oxidation inhibitors) were the primary sources of error in DOC concentration determination. Equally important to the routine analysis of DOC has been the increase in availability and widespread use of consensus reference materials, such as those

offered by the Hansel lab at the University of Miami, which has been provided to over 240 laboratories worldwide (<http://yyy.rsmas.miami.edu/groups/biogeochem/CRM.html>).

The now routine nature of DOC analysis has allowed for DOC determination to be coupled with isotope ratio mass spectrometers (IRMS) to determine not only DOC concentrations in natural waters but also the $\delta^{13}\text{C}$ signature of the DOC. While DOC-IRMS coupling is straightforward for the analysis of freshwater, low DOC concentration (usually $< 100 \mu\text{mol L}^{-1}$) marine samples present a complex analytical challenge. The high dissolved salt content ($>3\%$ wt) leads to incomplete organic matter oxidation in wet chemical oxidation instruments, as the oxidation of DOC by persulfate is inhibited by inorganic ions found in seawater, such as Cl^- (Aiken, 1992; Peyton, 1993) and limited sample throughput due to salt build-up within the inner workings of the instrument. Only recently have instrument developments made this measurement possible with sufficient precision and accuracy to acquire meaningful data (Bouillon et al., 2006; Osburn and St-Jean, 2007b; Federherr et al., 2014; Lalonde et al., 2014a).

Natural abundance carbon stable isotope ($\delta^{13}\text{C}$) signatures can be exploited to track the sources and transformations of the various carbon pools along this continuum. Differences in $\delta^{13}\text{C}$ signatures arise either from differences in carbon fixation mechanisms or initial carbon source used during carbon fixation (Farquhar et al., 1989; Guy et al., 1993). These differences allow for the use of $\delta^{13}\text{C}$ signatures as source indicators, with marine organic matter being more enriched in ^{13}C (Williams and Druffel, 1987; Bauer and Druffel, 1998; Wang and Druffel, 2001), leading to less negative $\delta^{13}\text{C}$ signatures, compared to higher order terrestrial plant organic matter (Hedges et al., 1997; Lalonde et al., 2014a). In marine environments, newly photosynthesized organic matter is created through the fixation of dissolved inorganic carbon, which has an initial $\delta^{13}\text{C}$ signature of approximately 0 ‰, while in terrestrial environments the source material for carbon

fixation is atmospheric CO₂, with a signature ranging from -8 to -9 ‰ (Earth System Research Laboratory Global Monitoring Division of NOAA; <https://www.esrl.noaa.gov/gmd/dv/iadv/>).

These variations in source material and fractionation factors for different photosynthetic C fixation pathways lead to marine planktonic organic matter having $\delta^{13}\text{C}$ -DOC signatures of -19 to -24‰ compared to typical woody terrestrial organic matter $\delta^{13}\text{C}$ -DOC signatures of -28‰ (Peterson and Fry, 1987).

These natural changes in $\delta^{13}\text{C}$ -DOC can be exploited in conjunction with isotope mass balance calculations to decipher the fate of terrestrial and/or marine organic matter (Bauer et al., 2002; Osburn and St-Jean, 2007b; Bouillon et al., 2012; Lalonde et al., 2014a). They are most useful for looking at the freshwater to saline continuum, where $\delta^{13}\text{C}$ -DOC signatures are different enough to discriminate between terrestrial and marine organic matter. The St. Lawrence Estuary and the Hudson Bay/Strait north of Quebec are important systems in terms of both total water and organic carbon discharge. Of particular note is the St. Lawrence Valley river system between the Great Lakes to the Atlantic Ocean (Qc, Canada), the second largest freshwater discharge in North America (Xie et al., 2012), where the estimated seaward DOC flux reaches 1.55×10^9 kg C yr⁻¹ (Telang et al., 1991). Coupled with the hypoxic and acidic bottom waters found in this region (Mucci et al., 2011), the high riverine DOC to particulate organic carbon (POC) ratio of 10:1 (Hélie, 2004) makes it an important study site for understanding terrestrial DOC export and molecular level transformations during its transit.

The importance of the Hudson Bay and surrounding regions, in the context of carbon cycling, arises from its large drainage basin (1/3 the size of Canada) and high water discharge rates, with a total of 5.5×10^9 kg of DOC flowing into the Hudson Bay from the surrounding large river systems and hydrological dams on a yearly basis (Déry et al., 2005). The bulk of the discharged

organic matter originates from southernmost rivers (4.6×10^9 kg of the 5.5×10^9 kg of total organic C per year) draining the surrounding boreal forest (Mundy et al., 2010); as well as from Quebec's large river systems and hydro-reservoirs to the north. This is in contrast to the eastern coast of Quebec and Labrador which is sparsely vegetated with several fjords, located north of the tree-line, discharging out to the Labrador Sea (Bentley and Kahlmeyer, 2012).

Importantly, several processes are known to alter the bulk isotopic signature of organic matter through the preferential removal of specific organic functionalities (Wang and Druffel, 2001). Changes in DOC stable isotope signatures along the freshwater-marine continuum and throughout the water column are either due to differences in organic matter sources or through the re-working of this organic matter during degradation. While bacterial degradation does not lead to significant ^{13}C fractionation between the initial material and the altered organic remnants, (Shaffer et al., 1999; Bauer, 2002), photo-oxidation of riverine organic matter leads to an increase in $\delta^{13}\text{C}$ -DOC signatures, owing to the preferential removal of conjugate carbon-carbon double bonds, which are more sensitive to UV degradation than saturated C-C bonds and other carbon containing functionalities (Lalonde et al., 2014a). Unfortunately, the changes in the signature of the terrestrial end-member upon photo-degradation, combined to the broad range of reported values for the marine end-member, make the use of isotopic mass balance calculations to quantify the proportion of terrestrial and marine DOC in a sample extremely uncertain.

Here, using carbon stable isotopes and DOC concentrations, we discuss DOC dynamics in Canada's Eastern coastal waters, including the St. Lawrence Estuary, East Coast of Newfoundland and Labrador and the Hudson Strait. Coupled with previous terrestrial vs. marine proxy studies (Tremblay and Gagné, 2009; Xie et al., 2012; Zhang and Xie, 2015), we explore different processes, such as photo-oxidation, leading to variations in carbon stable isotope

signatures for DOC from different locations and water column depths. We also discuss the limitations of isotopic mass balance calculation approaches to apportion DOC sources along the freshwater-ocean continuum, which arise from the uncertainties in $\delta^{13}\text{C}$ signatures of the end-members used in the model.

3.3. Materials and Methods

3.3.1. St. Lawrence Valley River System

Draining the North American Great Lakes, the St. Lawrence River is the Canadian river with the highest water discharge, transporting approximately 413 km^3 of water per year to the Gulf of the St. Lawrence (Telang et al., 1991). Based on differences in water column depth and salinity, it can be separated into 3 major regions, the Upper and Lower Estuaries, and the Gulf (Fig. 3-1a). The Upper Estuary (USLE) begins near Quebec City and extends towards Tadoussac and the mouth of the Saguenay Fjord (Stations 1 to 12; Fig. 3-1b). It is characterized by relatively shallow water and a steep salinity gradient ranging from under 0.1 near Quebec City to approximately 22.5 near Tadoussac. Seaward of the USLE, the water column is characterized by a strong vertical stratification. Differences in density between surface waters flowing seaward and the colder, denser waters flowing into the estuary from the Atlantic, coupled with changes in surface water density during the warmer summer months, allow for the formation of a cold intermediate layer (CIL), characterized by a local temperature minimum (Gilbert and Pettigrew, 1997), as low as -1°C during the May 2016 sampling mission. The Lower St. Lawrence Estuary (LSLE) begins near Tadoussac, where there is a steep change in water column depth, dropping by over 200 m as this is the head of the Laurentian Channel, a trough that extends out to the Atlantic Ocean, through the Cabot Strait. Here, the stratified water masses of the St. Lawrence River valley system mix owing to the upwelling currents originating from the Atlantic (Mucci et

al., 2011). The LSLE (Stations 13 to 19 in this study) is characterized by higher surface water salinities (22-30) and lower DOC concentrations. Finally, the Gulf of the St. Lawrence incorporates water from the lower estuary as well as high salinity waters flowing in from the northeast and southeast through the Belle-Isle Strait and Cabot Strait, respectively.

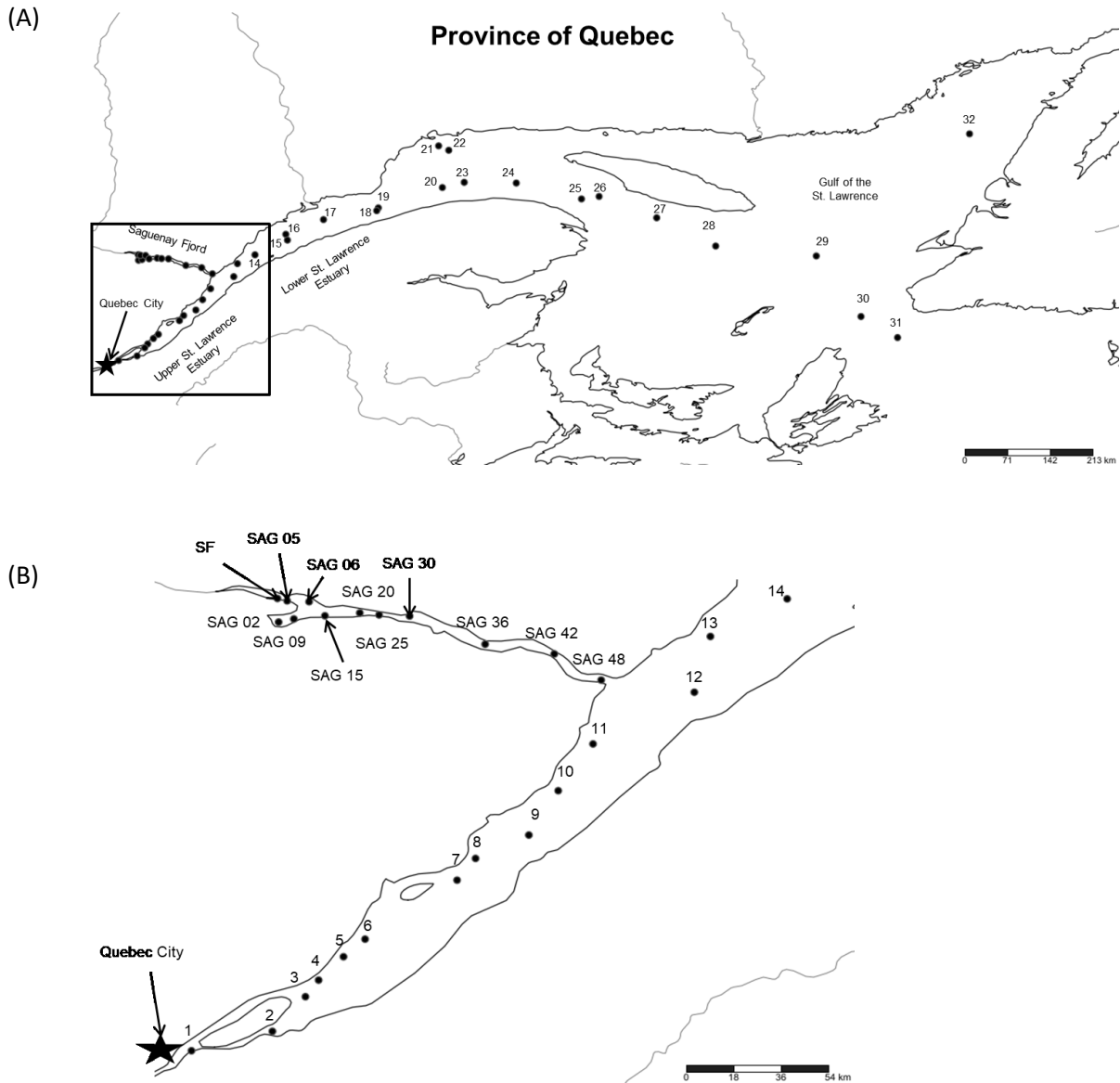


Figure 3-1 (a) Map of all sampling stations in the Upper and Lower St. Lawrence Estuaries, Gulf of the St. Lawrence and Saguenay Fjords. Station numbers increase from 1 to 33 starting near Quebec City and increasing seaward. The station numbers for the boxed area can be found in the inset map (b) the sampling stations from the Upper St. Lawrence Estuary and Saguenay Fjord.

3.3.2. Hudson Strait

The Hudson Strait joins Hudson Bay to the Labrador Sea and sits between the northern tip of Quebec and Baffin Island (Fig. 3-2). Along the northern coast, water flows westward towards the Hudson Bay, while flowing eastward towards the Labrador Sea along the southern coast (Straneo and Saucier, 2008). The Hudson Strait joins the largest body of water that completes a yearly freeze/thaw cycle (the Hudson Bay) to the Labrador Sea, acting as an important source of freshwater (salinity <28) to the Labrador Current and global thermohaline circulation.

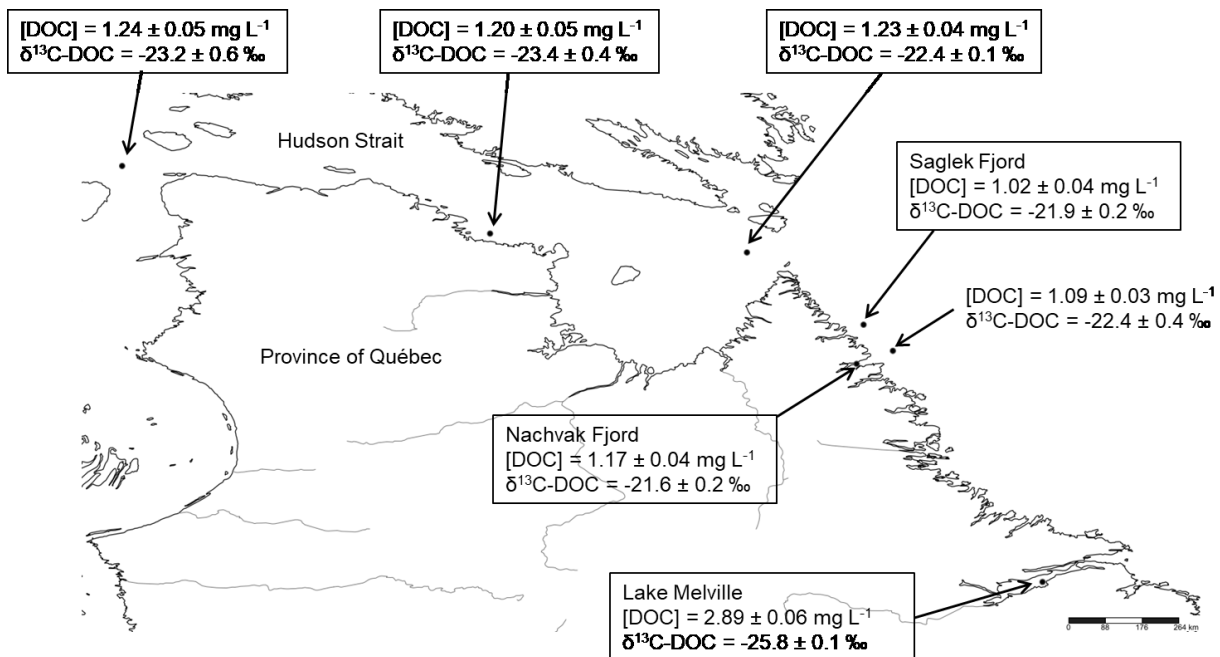


Figure 3-2. Map of all northern sampling stations including their respective surface water DOC concentration and $\delta^{13}\text{C-DOC}$ signatures.

3.3.3. Sample collection

Water samples were collected aboard the R/V Maria S. Merian and the R/V Coriolis II (September 2015 and May 2016 respectively) using a CTD Rosette fitted with 12.5 L Niskin bottles. Combusted (450 °C for 6 hours) EPA borosilicate vials (40 mL) with PTFE lined caps were filled with water filtered through combusted 0.7 μm glass fiber filters. All samples were

acidified to pH 2 using 12N TRACE select grade HCl and stored at 4°C in the dark prior to their analysis in the laboratory. Surface water (depth of between 2 and 3 m) was collected at all stations (11 in the USLE, 12 in the Saguenay Fjord, 20 in the LSLE and Gulf, as well as 7 on the Labrador Coast and Hudson Strait; Figs. 3-3, and Tables A1-A3). In addition, one deep-water sample was collected about 10 m above the sediment-water interface at four USLE stations where the water column is stratified (Stations 6, 9, 10 and 11), as well as at one station in the Saguenay Fjord (Station SAG 30). In the LSLE and Gulf, partial profiles (4 depths) were collected at each station (surface, in the middle of the CIL layers at depths between 30 and 70 m, middle of the deep water mass 200 and 250 m, and about 10 m above the sediment-water interface at depths varying between 196 and 437 m).

3.3.4. Analytical methods

DOC concentrations and $\delta^{13}\text{C}$ -DOC signatures were determined using a modified Aurora OI 1030 high-temperature catalytic oxidation unit coupled to a chemical trap (GD-100, Graden Instruments Inc., Ontario, Canada) and a GV/V Isotope Ratio Mass Spectrometer (Isoprime Ltd., Manchester, UK). The total organic carbon analyzer was modified in order to decrease the baseline CO_2 content by replacing the original PTFE tubing with PEEK tubing, which is less permeable to CO_2 , even at elevated temperatures. A system pressure of 30 psi was used, while the combustion column was maintained at 680°C. For each sample, four replicate injections of 1.5 mL were sent to the combustion column after 2.5-min sparge at 90°C to remove any dissolved inorganic carbon in the water. The analysis of one replicate injection takes approximately 17.5 min. A full description of the GD-100 trap valve configuration can be found in Lalonde et al. (2014a). For the fully saline samples approximately 60 injections could be performed before cleaning the combustion column due to salt build-up.

In-house calibrated β -alanine (40.4% OC, -26.18 ± 0.10 ‰), sucrose (42.1 %OC, -11.77 ± 0.09 ‰) and potassium hydrogen phthalate (47.0% OC, -28.14 ± 0.10 ‰), dissolved in 18.2 m Ω cm⁻¹ milli Q water, were used as isotopic standards while β -alanine was used as a standard for DOC concentration. The post calibration isotope signature was then blank subtracted using an isotope mass balance correction modified from (Brand, 2004; Panetta et al., 2008; Lalonde et al., 2014a),

$$\delta^{13}C_{sample} = \frac{\delta^{13}C_m \eta_m - \delta^{13}C_b \eta_b}{\eta_m - \eta_b} \quad (\text{Eq. 3-1})$$

where η_m and η_b are the measured and blank intensities respectively, assuming that the measured $\delta^{13}C$ signature is determined by only the sample and blank contributions in a linear fashion. The intensity of the blank was determined through repeated blank measurements while the $\delta^{13}C$ signature of the blank was extrapolated using a 4 or 5 point β -alanine calibration curve of varying concentration plotted against the inverse intensity (Fry et al., 1992), which also served to ensure instrument linearity over the desired range of concentrations. Solving for the intercept gives the blank corrected $\delta^{13}C$ (δ_{bc}) signature, but the actual true blank $\delta^{13}C$ signature (δ_b) can be solved for using the following formula (Lalonde et al. 2014a),

$$\delta_b = \left(\frac{\text{slope}}{\eta_b} \right) + \delta_{bc} \quad (\text{Eq. 3-2})$$

where the slope is taken from the plot of 1/intensity vs. $\delta^{13}C$.

3.4. Results

3.4.1. Saguenay Fjord

The Saguenay Fjord is considered an important contributor of terrestrial organic matter as it discharges into the St. Lawrence Estuary near Tadoussac (Tremblay and Gagné, 2009; Xie et al., 2012; Zhang and Xie, 2015). The surface $\delta^{13}C$ -DOC signatures measured across the Saguenay

Fjord were practically invariant with an average $\delta^{13}\text{C}$ -DOC across all surface stations of -26.6 ± 0.4 ‰ and DOC concentrations ranging between 4.05 and 5.25 mg L⁻¹ OC (N=12) (Table A1-1). Where the water column is deepest, at station SAG 30 (Smith and Walton, 1980; Locat and Levesque, 2009), a significant decrease in DOC concentration was observed between the surface and deep waters, from 5.25 ± 0.01 mg L⁻¹ to 1.46 ± 0.02 mg L⁻¹, respectively, alongside an enrichment in $\delta^{13}\text{C}$ -DOC of 2.1 ‰. These deep, high salinity waters have a mixed terrestrial and marine carbon stable isotope signature of -24.6 ± 0.2 ‰ (Table A1-1). Surface waters from the Saguenay have a low salt content (salinity between ~0 and 4.3) with the exception of station SAG 48, the closest from the St. Lawrence Estuary, where the salinity reaches 12.4 as determined from conductivity measurements.

3.4.2. Northern Quebec and Labrador

DOC in water from the Saglék and Nachvack fjords and surrounding coast was predominantly of marine origin with $\delta^{13}\text{C}$ -DOC signatures ranging between -21.6 ± 0.2 ‰ and -22.4 ± 0.4 ‰ (Fig. 3-2) and concentrations ranging from 1.02 ± 0.04 to 1.17 ± 0.04 mg L⁻¹. This is in contrast to the Hudson Strait, which had slightly higher DOC concentrations (approximately 1.2 mg L⁻¹) while being more depleted in ¹³C (Fig. 3-2). The DOC concentrations across the Hudson Strait were fairly similar but the $\delta^{13}\text{C}$ -DOC signatures became more depleted going west, from -22.4 ± 0.1 ‰ to -23.2 ± 0.6 ‰. Finally, surface water samples collected from Lake Melville contained more DOC than the other northern stations, with a concentration of 2.89 ± 0.06 mg L⁻¹ and a $\delta^{13}\text{C}$ -DOC signature of -25.8 ± 0.1 ‰ (Fig. 3-2).

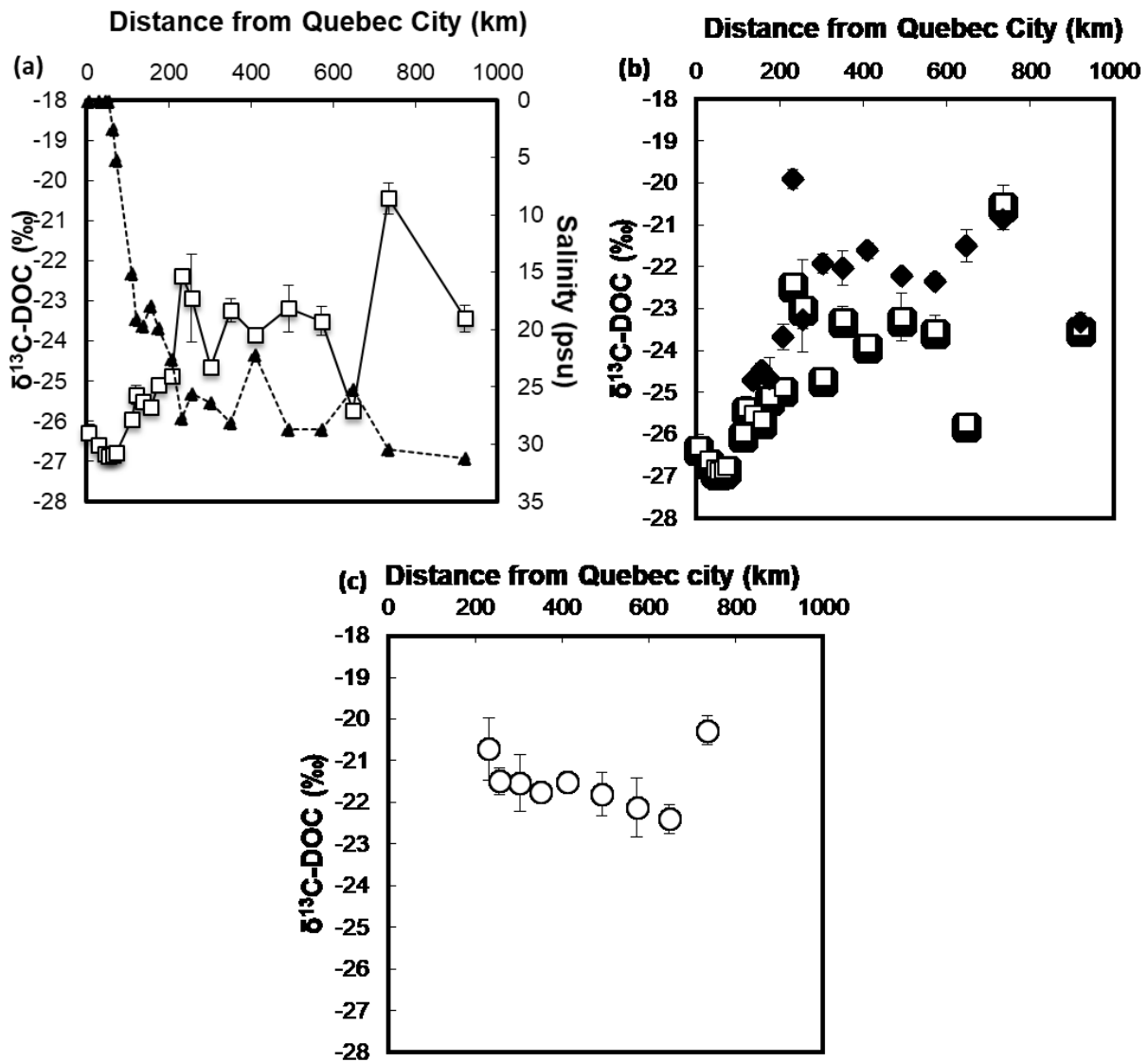


Figure 3-3. (a) $\delta^{13}\text{C-DOC}$ signatures (open squares) and salinity (filled triangles) for the surface waters across the St. Lawrence Estuary and Gulf (b) $\delta^{13}\text{C-DOC}$ signatures for the surface (open squares) and cold intermediate (filled diamonds) water layers (CIL) as a function of the distance from Quebec city (c) $\delta^{13}\text{C-DOC}$ signatures for the deep water layers (open circles), all as a function of the distance seaward from Quebec City. Error bars represent the reproducibility from 4 replicates. Deep waters were collected approximately 3 m above the sediment-water interface.

3.4.3. Across the St. Lawrence Estuary and Gulf

Samples collected from the USLE had an average $\delta^{13}\text{C}$ -DOC signature of -26.7 ± 0.4 ‰ (Fig. 3-3, up to ~210 km from Quebec City), the lowest $\delta^{13}\text{C}$ -DOC signatures observed in this study along with those from the Saguenay Fjord. Within the mixing zone, there is a gradual enrichment in $\delta^{13}\text{C}$ -DOC signature for the surface samples ranging from -26.9 ± 0.1 ‰ at station 5 (~65 km from Quebec City) to -22.4 ± 0.1 ‰ at station 24 (~571 km from Quebec City), with salinities of 2.5 and 27.7, respectively (Fig. 3-3).

Within the Gulf of the St. Lawrence, DOC concentrations are lower compared to the upper estuary, ranging from 2.03 ± 0.10 mg L⁻¹ for surface waters immediately south of Anticosti Island (Station 25) to 0.64 ± 0.05 mg L⁻¹ for deep water at Station 27 (Tables A2 and A3). These samples are also among by the most extreme $\delta^{13}\text{C}$ -DOC signatures observed for this region with the near shore sample near Anticosti Island (Station 25) having a strong terrestrial signature of -25.7 ± 0.1 ‰, while the low concentration, salty bottom waters at station 27 is typically marine (-20.3 ± 0.7 ‰; Table A1-3).

Across both sampling missions, a trend towards more positive $\delta^{13}\text{C}$ -DOC signatures was observed for the St. Lawrence Estuary samples from the CIL compared to surface water samples (Table A1-3; representative profiles are shown as examples on Fig. 3-3b and Fig. 3-4). This enrichment in ¹³C of DOC within the CIL was observed at 16 of the 20 stations, with statistically significant differences being observed at 8 stations ($\alpha = 0.05$). The largest differences in $\delta^{13}\text{C}$ -DOC signatures between the surface and CIL water layers were found off the coast of Anticosti Island (Station 25), with signatures of -25.7 ± 0.1 ‰ and -21.5 ± 0.4 ‰ for the surface and cold intermediate layers, respectively (Fig. 3-3b and Table A1-3). Samples from stations 29 and 31 (Fig. 3-4), near the transition between the Gulf of the St. Lawrence and the Atlantic Ocean,

showed no change in $\delta^{13}\text{C}$ -DOC down the water column. This is in contrast to samples from the Esquiman Chanel (Station 32) where the $\delta^{13}\text{C}$ -DOC signatures were more depleted within the CIL but then returned to values similar to those at the surface at depth (Fig. 3-4). A compilation of all the DOC concentrations and $\delta^{13}\text{C}$ signatures collected in this study is available in Table A1-1.

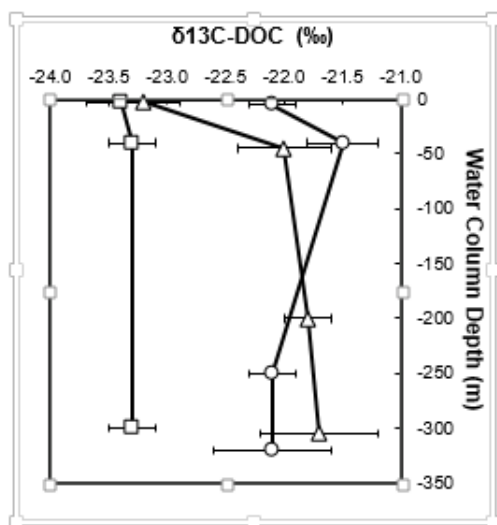


Figure 3-4. Sample water column $\delta^{13}\text{C}$ -DOC signatures profiles showing invariable $\delta^{13}\text{C}$ -DOC signatures at station 29 (open squares), or enrichment in $\delta^{13}\text{C}$ -DOC between the surface and cold intermediate layer at station 17 (open triangles) and station 33 (open circles). All three stations are located in the Gulf of St. Lawrence (Fig. 3-1). Error bars are 1σ standard deviations from 4 replicates.

3.5. Discussion

3.5.1. Terrestrial Organic Matter Inputs from the Saguenay Fjord

The DOC concentrations for the surface waters from the Saguenay Fjord were the highest among the regions analyzed in this study. These high DOC concentration surface waters discharge into the St. Lawrence Estuary near Tadoussac and account for a large fraction of the total discharge of terrestrial organic matter in the estuary (Schafer et al., 1990; Tremblay and Gagné, 2009; El-Sabh and Silverberg, 2012). The measured $\delta^{13}\text{C}$ -DOC signatures in these surface waters are

predominantly terrestrial in nature, in agreement with the previously reported bulk organic C/N molar ratios of 21 to 25 (Pocklington and Leonard, 1979; Louchouart et al., 1997; St-Onge and Hillaire-Marcel, 2001) and the terrestrial-specific lignin degradation products (Louchouart and Lucotte, 1998). This result reflects the fact that the surrounding vegetation is dominated by boreal forest and, more specifically, woody gymnosperms (Louchouart et al., 1997).

Although surface DOC concentrations and carbon stable isotope signatures remain relatively constant throughout the Saguenay Fjord, variations in both concentrations and $\delta^{13}\text{C}$ -DOC were observed between surface waters and those just above the sediment water interface (Table A1-1). The waters of the Saguenay remain distinct and vertically stratified (Yeats and Bowers, 1976), with high DOC, brackish surface waters flowing above the mostly saline deep waters, which flow into the Fjord from the St. Lawrence Estuary (Bourgault et al., 2012). The mixed terrestrial/marine $\delta^{13}\text{C}$ -DOC signature for the deep waters arises from a combination of the degradation of the more labile components of particulate organic matter as it sinks within the water column, as well as from mixing of relatively fresh terrestrial organic matter discharged from the surrounding boreal forest and the less reactive, partly marine organic matter transported into the Saguenay from the St. Lawrence Estuary.

Despite the vast amount of work exploiting bulk and compound-specific stable carbon isotope analysis done on sediment organic matter from terrestrial-to-marine transition zones, relatively few stable isotope analyses can be found in the literature for non-fractionated, bulk dissolved organic matter using an appropriate analytical methodology. A study on fjords from the Fiordland National Park in New Zealand (Yamashita et al., 2015) reported surface $\delta^{13}\text{C}$ -DOC signatures between -28.1 ‰ to -31.8 ‰, several permil more depleted than those reported here, a difference likely due to differences in the type of vegetation found in Fiordland compared to the

Saguenay River watershed. The most depleted terrestrial values reported in this study (-26.9 ± 0.1 ‰; Table A1-1 and A1-2) are similar to those measured by Osburn and Stedmon (2011) in the Baltic-North Sea transition zone, reflecting the fact that both regions drain catchments dominated by boreal forest (Stepanauskas et al., 2002; Mundy et al., 2010). These results highlight the importance of constraining and selecting an appropriate signature for the terrestrial $\delta^{13}\text{C}$ -DOC end-member value based on the surrounding vegetation and organic matter inputs when attempting to perform isotope mass balance calculations.

3.5.2. Dependence of $\delta^{13}\text{C}$ -DOC Signatures on the Vegetation in the Drainage Basin

As opposed to the Saguenay Fjord which receives large quantities of organic matter in the form of woody gymnosperms, the stations from Northern Québec and the North-Eastern Coast of Labrador (Nunatsiavut) are located above the tree line in the Torngat Mountains National Park (Elliott and Short, 1979). Notably, the DOC in samples from within the Saglek Fjord as well as at the mouth of the Saglek and Nachvak Fjords were less depleted in ^{13}C relative to the Saguenay, with comparatively lower DOC concentrations. The erosion-resistant bedrock (Wilton, 1996) coupled with the decreasing abundance of woody trees in this region (Bentley and Kahlmeyer, 2012) likely explains the absence of terrestrial signatures in these fjord systems despite the presence of riverine water inputs. A similar marine-like signature (-22.3 ± 0.2 ‰) was obtained by (Druffel et al., 2017) for a sample collected near the surface in the North Atlantic Ocean south of Iceland.

The western side of Quebec is dominated by large river systems and hydro-dammed reservoirs surrounded by the boreal forest, leading to higher terrestrial organic inputs into the Hudson Bay compared to the Nachvak and Saglek Fjords. This influx of OC and the dominant surface

currents may explain the trend across the Hudson Strait, going from depleted mixed terrestrial/marine organic $\delta^{13}\text{C}$ signatures to more enriched signatures (from -23.4‰ to -22.4‰) as water is transported out to sea from the Hudson Bay across the Hudson Strait (Fig. 3-2). Previous studies looking at the fate of chromophoric dissolved organic matter (CDOM), another organic matter source indicator, have shown a similar trend in this region (Granskog et al., 2007). Fluorescence analysis of the dissolved organic matter (DOM) from this region, coupled to parallel factorial analysis (PARAFAC), showed that terrestrial organic matter inputs into the Hudson Bay are high and as water is carried from the Hudson Bay through the Hudson Strait there is a loss of terrestrial organic matter biomarkers (Granskog, 2012). The $\delta^{13}\text{C}$ signature for DOC of $-23.4 \pm 0.4\text{‰}$ obtained for the westernmost station included in this study, at the mouth of the Hudson Strait, likely represents a mix of transported terrestrial and freshly produced planktonic organic matter.

Along the southern coast of the Hudson Strait, water flows eastward (Straneo and Saucier, 2008) transporting a fraction of the terrestrial inputs from the Hudson Bay through the Hudson Strait, explaining the gradual enrichment in $\delta^{13}\text{C}$ -DOC signatures going towards the Labrador Sea. The dominant terrestrial characteristics of DOC in the Hudson Bay were not observed within the Hudson Strait in previous studies (Granskog et al., 2007; Guéguen et al., 2011). Here we show the progressive loss of the terrestrial DOC isotope signature across the Strait, reaching almost entirely marine $\delta^{13}\text{C}$ -DOC signatures in Canada's northeastern coastal waters.

3.5.3. $\delta^{13}\text{C}$ -DOC signatures across the St. Lawrence Estuary salinity gradient

The shift in $\delta^{13}\text{C}$ -DOC signatures towards more enriched values, observed for surface waters moving seaward from Quebec City, coincides with an increase in salinity (Fig. 3-3a). Water from the freshwater Upper Estuary stations 1 to 4 (salinity <2.5) flows eastward, where it begins to mix with more saline waters from the Gulf of the St. Lawrence. The seaward change in $\delta^{13}\text{C}$ -DOC represents differences in organic matter inputs, dilution of terrestrial DOC with endogenously photosynthesized marine DOC, as well as the effect of processes which alter organic matter composition such as photo-oxidation of chromophoric DOM (Xie et al., 2012).

The trend showing the decreasing terrestrial organic matter contributions in the St. Lawrence Estuary has also been reported in the sediment record, where the relative abundance of terrestrial organic matter biomarkers decreases across the St. Lawrence Estuary to the Gulf (Pocklington and Leonard, 1979; Alkhatib et al., 2012). Notably, both the Saguenay and USLE have large terrestrial organic matter inputs from the surrounding mixed temperate and boreal forest delivered by major rivers. The ubiquitous average $\delta^{13}\text{C}$ -DOC signature for these terrestrial dominated stations, similar to the $\delta^{13}\text{C}$ -DOC signature of the DOC discharged by the St. Lawrence River (Hélie, 2004), suggests that it represents an appropriate terrestrial end-member for $\delta^{13}\text{C}$ -DOC mixing models. In fact, several freshwater to saline transition zones have $\delta^{13}\text{C}$ -DOC values similar to the terrestrial organic carbon end-member determined for the Upper St. Lawrence Estuary (-26.7 ± 0.4 ‰) including the Baltic Sea, Perdido Estuary in Florida (Coffin and Cifuentes, 1999) and the Danube-Black Sea mixing zone (Saliot et al., 2002) as well as for ocean margins near the Mid-Atlantic Bight (Guo et al., 1996).

Additionally, many studies looking at the $\delta^{13}\text{C}$ -DOC of riverine samples have reported more depleted signatures than the most extreme values reported here (Spiker and Rubin, 1975;

Raymond and Bauer, 2001a; Guo and Macdonald, 2006; Lalonde et al., 2014b). These differences could either be due to methodological artifacts involving some form of discrimination towards a specific fraction of the dissolved organic matter pool when using ultrafiltration or solid-phase extraction to desalt the samples, or to differences in organic matter inputs from the surrounding drainage basin. Only recent analytical advancements (Osburn and St-Jean, 2007b; Federherr et al., 2014; Lalonde et al., 2014a) have allowed for carbon stable isotope analysis of dissolved organic carbon without fractionating the DOC pool based on molecular weight or chemical composition (reviewed in (Raymond and Bauer, 2001b)). Great care must thus be taken when comparing literature values for $\delta^{13}\text{C}$ -DOC analysis owing to such methodological differences.

Freshwater to saline transition zones can be found throughout the globe, yet do not always show the same trend between $\delta^{13}\text{C}$ -DOC and salinity. An interesting case is the Tana Delta in Kenya, where the opposite trend was observed compared to the St. Lawrence Estuary, with less depleted $\delta^{13}\text{C}$ -DOC signatures observed at the freshwater sampling sites and more depleted signatures at the saline sampling sites (Bouillon et al., 2007). Clearly, the relationship between salinity and the carbon stable isotope signature of DOC is not universal. In the case of the Tana Estuary, the contribution planktonic organic matter to the total DOC pool is very small (Bouillon et al., 2007), yet the measured $\delta^{13}\text{C}$ -DOC signatures are similar to those observed here for the St. Lawrence Estuary owing to inputs of OM derived from C3 and C4 vegetation in the watershed (Bouillon et al., 2007). This similarity in $\delta^{13}\text{C}$ -DOC signatures despite the vastly different sources of DOC further reinforces the need to adequately constrain the end-members used for stable isotope mixing model calculations based on the sources of organic matter inputs.

Based on the combination of the measured $\delta^{13}\text{C}$ -DOC signatures and ratio of particulate organic carbon to the chlorophyll A observed for the Tana estuary, the contribution of a marine planktonic $\delta^{13}\text{C}$ -DOC member is negligible relative to the total DOC pool (Bouillon et al., 2007). This has the benefit of increasing the discrimination power of isotope mass balance calculations owing to the large difference in $\delta^{13}\text{C}$ -DOC signatures between the two main end-members. In systems like the St. Lawrence Estuary where the contribution from marine organic matter is significant, establishing the marine end-member for these isotope mixing model calculations can be challenging, with values varying between about -18 to -24 ‰ being used across different studies (e.g. Bauer et al. 2002; Osburn and Stedmon 2011; Lalonde et al. 2014b). The potential artefacts linked to the desalting of DOC using ultrafiltration or solid-phase extraction in preparation for $\delta^{13}\text{C}$ -DOC analysis are exacerbated for saline samples, with DOC recoveries of less than 50% and as little as 20 to 30% of the total DOC pool (Raymond and Bauer, 2001b). Such chemical or size fractionation of dissolved organic compounds with different $\delta^{13}\text{C}$ signatures most often leads to differences between the $\delta^{13}\text{C}$ signatures of the desalted and total DOC pools. Based on our results for a system such as the St. Lawrence Estuary where the drainage basin is dominated by boreal forest plants that act as a source of ^{13}C -depleted carbon, an appropriate marine end-member would be similar to our most enriched values of -20.3 ± 0.7 ‰ (Table A1-3), similar to the value reported by Williams and Druffel in 1987.

3.5.4. Changes in $\delta^{13}\text{C}$ -DOC signatures with depth in the water column

Two sources may explain the trend towards more enriched $\delta^{13}\text{C}$ -DOC values within the CIL compared to surface waters: 1) marine DOC originating from the surface waters of the Labrador Sea, and 2) photodegraded terrestrial DOC transiting through the estuary surface waters.

First, the ^{13}C -enriched organic matter flowing into the St. Lawrence Gulf from the Labrador Sea and Atlantic Ocean is supported by previous work from Mucci et al. (2011), who suggests that the CIL is fed by cold, marine water flowing into the Gulf through the Strait of Belle Isle from the northeast (Mucci et al., 2011). This creates a net landward flow for the CIL north of Anticosti Island where the CIL is thickest. DOC enriched in ^{13}C produced in marine surface waters in the Labrador Sea is transported into the Gulf of the St. Lawrence, where the cold and salty CIL subducts beneath the warmer and less salty surface waters of the Gulf.

Additionally, the heating of surface waters during the spring and summer causes a stratification between the warmer top 30-45 m of the water column and the CIL (Mucci et al., 2011).

Therefore, also at play is the partial (photo)degradation of terrestrial organic compounds during their transit across the St. Lawrence Estuary and Gulf. Recent work involving the artificial irradiation of DOC samples, exclusively of riverine origin, has shown an enrichment of up to 3 ‰ in $\delta^{13}\text{C}$ -DOC signatures upon irradiation equivalent to a half-year of UV radiation (Lalonde et al., 2014a). Exposure of organic matter to sunlight prior to the formation of the CIL could cause this biochemical fractionation through the preferential removal of photosensitive organic molecules. Complex organic molecules containing conjugated double bond systems, such as those found in chromophoric compounds, are more likely to undergo photochemical reworking when exposed to UV radiation (Blough and Del Vecchio, 2002; Xie et al., 2012). Such large aromatic compounds are commonly associated with lignin and lignin degradation products in terrestrial environments, as well as vascular plant cell wall materials (tannins and cutans) which tend to be depleted in ^{13}C relative to the bulk organic matter pool (Goñi and Eglinton, 1996). Preferential removal of $\delta^{13}\text{C}$ depleted DOC causes an enrichment in ^{13}C for the residual measurable DOC pool, which could lead to values such as those observed for the cold

intermediate layer in this study. More work is needed to determine the relative importance of these two mechanisms explaining the enriched $\delta^{13}\text{C}$ -DOC signatures within the CIL. These results also suggest that the DOC pool in this mass of water is more heavily altered, and thus more recalcitrant, than in the surface layer just above.

3.5.5. Comparison with the Baltic-North Sea Transition Zone

The comparison between the St. Lawrence Estuary and the Baltic-North Sea transition zone is a natural one, having similar sized drainage basins (Perttilä et al., 1980; Bugden, 1981) dominated by subarctic boreal ecosystems (Stepanauskas et al., 2002; Mundy et al., 2010) and affected by bottom water hypoxia (Gilbert et al., 2005; Conley et al., 2009). Also, both transition zones have highly stratified water columns with sub-surface temperature minima characteristic of a CIL. The previous work of Osburn and Stedmon (2011) coupled several biomarkers including $\delta^{13}\text{C}$ -DOC, excitation-emission matrix fluorescence and dissolved lignin phenol concentrations in order to better understand organic matter reworking in these types of systems, although with a limited number of sampling stations. Only two of the sampling cruises from that study collected $\delta^{13}\text{C}$ -DOC data from depths near the local temperature minimum within the Baltic Sea proper, unsurprising for the winter cruise as the CIL is formed from meltwater at the tail-end of the winter season (Gilbert and Pettigrew, 1997). Interestingly, there were observable differences in $\delta^{13}\text{C}$ -DOC between the surface waters and this CIL. Unlike in the present study where the DOC from the CIL was found to be more enriched in ^{13}C relative to the surface waters during both the spring 2015 and fall 2016 sampling missions, the shifts observed by Osburn and Stedmon (2011) showed an enrichment for the summer cruise (August 2006) while also showing a depletion during the fall (October 2006). More data specifically looking at differences between surface

waters and sub-surface temperature minima from the region would be needed in order to compare the cause of these isotopic shifts across both systems.

3.6. Conclusion

This study represents the most comprehensive $\delta^{13}\text{C}$ -DOC dataset for Canada's east coast to date, a step towards building a comprehensive carbon budget for this region. Terrestrial organic matter inputs can be tracked along fresh to saline water transition zones by exploiting the natural variations in $\delta^{13}\text{C}$ -DOC signatures between terrestrial and marine end-members. However, actual mass balance calculations are innately prone to large errors unless a series of suitable end-members are selected. The selection of the terrestrial end-member from regions where woody trees dominate the drainage basin is trivial, as seen by the lack of variability in freshwater $\delta^{13}\text{C}$ -DOC signatures ($-26.6 \pm 0.4\text{‰}$ in the Upper St. Lawrence Estuary and Saguenay Fjord). The marine end-member is more difficult to constrain, with $\delta^{13}\text{C}$ -DOC signatures varying between -20‰ and -23‰ for samples with salinities of ~ 35 (Fig. 3-5a). The larger analytical uncertainty associated for troublesome low DOC, high salt concentration samples lower the discrimination power of isotope mass balance calculations.

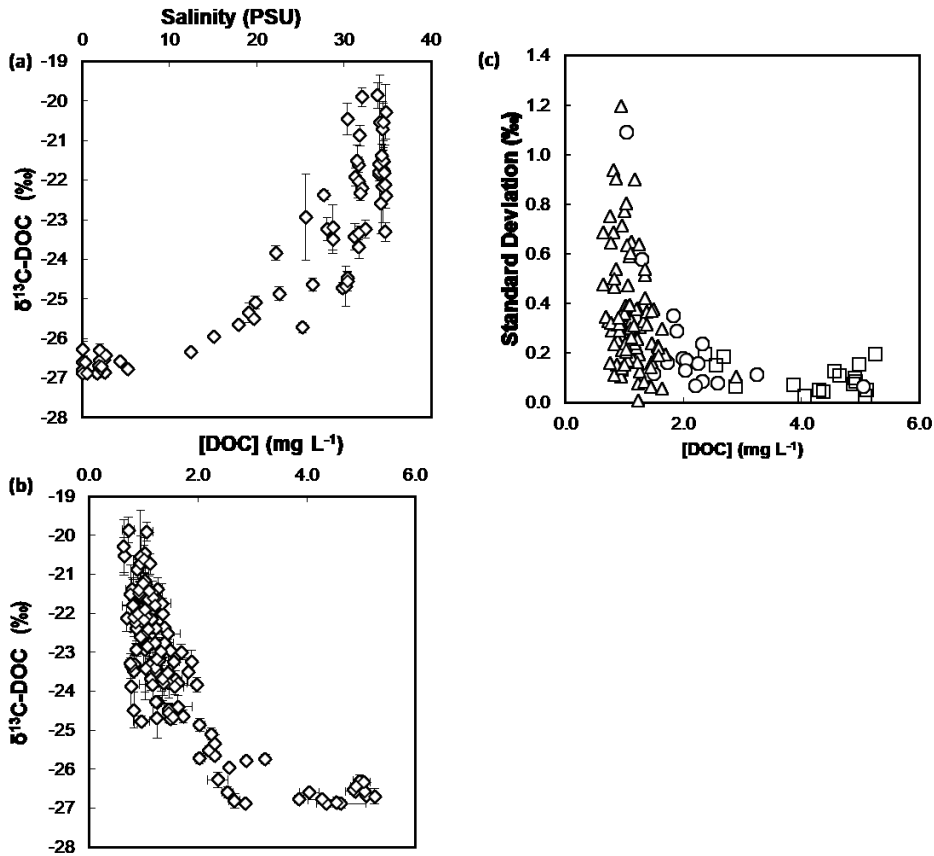


Figure 3-5 (a) $\delta^{13}\text{C-DOC}$ signatures across the St. Lawrence Estuary and Gulf as a function of salinity. (b) $\delta^{13}\text{C-DOC}$ as a function of the DOC concentration. The error bars represent the 1σ standard deviation from four replicates for the DOC concentration (horizontal) and $\delta^{13}\text{C-DOC}$ signatures (vertical). (c) 1σ standard deviations from replicate measurements as a function of DOC concentration for samples with salinities between 0-5 (open squares), between 5-30 (open circles) and above 30 (open triangles).

Specifically, when looking at the freshwater to marine continuum, an additional issue arises owing to the decrease in precision for low concentration DOC samples. Since the stations with higher organic matter inputs tend to be dominated by terrestrial runoff, the high DOC concentration samples tend to have more terrestrial $\delta^{13}\text{C-DOC}$ signatures (Fig 3-5b). This is in contrast to the low concentration marine samples which have a larger natural spread in $^{13}\text{C-DOC}$ content as well as higher analytical uncertainties due to their low DOC content and larger matrix effects. The cumulative effect of the decrease in precision associated to the marine samples and

their natural spread greatly decreases the discrimination power of isotope mass balance calculations. . The analytical precision obtained in this study was similar to that of Lalonde et al., 2014a, with standard deviations within 0.2 ‰ being expected for low salt samples with DOC concentrations greater than 2 mg L⁻¹, while those for salty, low DOC concentration samples, corresponding to the majority of the data, were within 1 ‰ of the mean (Fig. 3-5c). Organic matter re-working further decreases the discriminating power of isotope mass balance calculations, where the terrestrial organic matter signature can be altered owing to the preferential degradation of specific organic functionalities. Isotopic mass balance calculations must thus be used with care, particularly in surface waters with a low suspended solid content and high exposure time to sunlight. Future studies targeting the aromatic DOC content, such as fluorescence measurements with PARAFAC analysis, of waters from the CIL could be used to determine if the enrichment in $\delta^{13}\text{C}$ -DOC signatures observed here are due to photo-oxidation or differences in DOC inputs from the northeast of the St. Lawrence.

Chapter 4: The role of iron in the diagenesis of organic carbon and nitrogen in sediments: A long-term incubation experiment

Barber, Andrew^{a*}; Lalonde, Karine^{a*}; Mucci, Alfonso^b; Gélinas, Yves^a

^a GEOTOP and Department of Chemistry and Biochemistry, Concordia University, 7141 Sherbrooke Street West, Montreal (Quebec), Canada

^b GEOTOP and Department of Earth and Planetary Sciences, McGill University, 3450 University Street, Montreal (Quebec), Canada

*These authors contributed equally

Corresponding author:

Yves Gélinas

GEOTOP and Department of Chemistry and Biochemistry

Concordia University

7141 Sherbrooke Street West

Montréal (Québec), Canada, H4B 1R6

Tel.: 1-(514) 848-2424 (3337)

Fax: 1-(514) 848-2868

Email: yves.gelinas@concordia.ca

4.1. Abstract

The burial and preservation of organic matter (OM) in marine sediments is tightly coupled to the diagenetic cycles of iron and manganese. Recently, it has been shown that approximately 20% of the sedimentary organic carbon (OC) may be bound to reducible iron oxides (Lalonde et al., 2012). These strong iron-OC complexes, formed within the oxic layer of the sediment, are transferred to the deeper anoxic sediment layers through sedimentation, physical reworking and bioturbation and are metastable over geological timescales. Using long-term (250-day) incubations under various redox and amendment conditions (Fe(II) and dissolved OM (DOM) additions), we examined the effect of iron on the early diagenetic transformations of OM in marine sediments. The fate of fresh, algal-derived DOM was monitored by tracking its stable carbon isotopic signature ($\delta^{13}\text{C}$). We demonstrate the incorporation of the ^{13}C -depleted tracer into the sediment through sorption (adsorption and co-precipitation). In the presence of iron oxides, we observed increased transfer of the dissolved algal material to the solid phase, revealing the role of iron in shuttling DOM from sediment porewaters to sediment particles. Furthermore, we show that the presence of iron has a differential effect on OC and organic nitrogen (ON), with preferential preservation of OC and accelerated degradation of ON in the presence of reactive iron oxide surfaces. Hence, we propose that redox-sensitive metals may regulate the global redox balance through increased carbon preservation as well as exerting a control on the concentration of fixed nitrogen species in marine sediments.

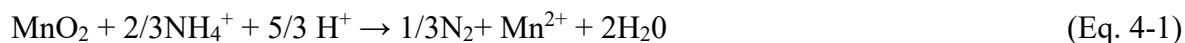
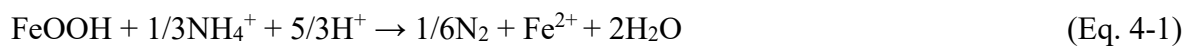
4.2. Introduction

The burial and preservation of organic matter (OM) in marine sediments are important factors in modulating the concentration of atmospheric oxygen and carbon dioxide over geological time (Bernier, 1989). Hence, elucidating factors that favor sedimentary OM preservation over its

degradation is important. OM can be physically shielded from degradation by adsorption to mineral particles. In fact, over 99% of sedimentary organic carbon (OC) is bound to particle surfaces - the remainder is found as discrete organic debris (Hedges and Keil, 1995; Keil et al., 1994; Ransom et al., 1998a). The surface area of sedimentary mineral particles determines the abundance of OM binding sites and modulates OC-mineral binding, maintaining surface loadings at a near constant and universal value (0.5-1.0 mg OC m⁻²) on continental shelves and margins (Keil et al., 1994; Mayer, 1994; Mayer, 1995). Organic compounds can also be protected from microbial degradation through encapsulation within diatom tests (Arnarson and Keil, 2007; Ingalls et al., 2003), expandable-clay interlayers (Kennedy and Wagner, 2011), particle mesopores (Mucci et al., 2000), and macromolecular hydrophobic OM (Mariotti et al., 1981). Over the past 20-30 years, the identification of these processes has shaped our understanding of the fate of OM in sedimentary systems, but the exact nature of these preservative interactions as well as the conditions under which they form still remain unclear. Recently, metal oxides have been identified as key players in the physical protection of OM, accounting for the sequestration and preservation of ≈20% of the OC in marine sediments (Lalonde et al., 2012).

Sedimentary nitrogen is essentially affected by the same preservative associations as OC, but the two species display divergent degradation pathways. The production of N₂ through denitrification and anammox in marine sediments is an important component of the global nitrogen cycle, influencing the oceanic inventory of fixed nitrogen (Burdige, 2006). Bacteria mediate the bulk of both OC and ON mineralization to CO₂ and N₂, but unlike OC remineralization, the traditionally accepted mechanisms of bacterial N₂ production are mainly confined to anoxic conditions (Burdige, 2006). A proposed alternative pathway of N₂ production in sediments (Devol, 2008) and soils (Yang et al., 2012) involves the direct oxidation of NH₄⁺

by manganese and iron oxides, a thermodynamically feasible process under both oxic and suboxic conditions (Yang et al., 2012). Balanced equations for these processes are shown here:



Redox-sensitive metals, such as iron and manganese, strongly impact the turnover of both OC and ON in marine sediments, but OM also affects the diagenetic cycling of iron. The growth of authigenic amorphous iron oxide phases is, for example, strongly inhibited by OM bound to their surfaces (Schwertmann, 1966). The reduction of oxides in sediments may also be hampered by organic matter (O'Sullivan et al., 1995). Nanophases of iron oxides are the dominant reactive oxides in both marine and lacustrine sediments (Raiswell and Canfield, 2012; Van der Zee et al., 2003) and these redox-sensitive phases, when associated to OM, somehow resist reduction after thousands of years of burial in anoxic sediments (Hease et al., 1997).

Elucidating the role of iron and manganese oxides on the degradation/preservation of OC and ON in sediments is impeded by the intrinsic complexity (e.g., spatial and temporal heterogeneity) of these systems. Benthic macrofauna, for example, affect elemental transport and cycling within the uppermost sediment layers and create microenvironments and lateral variability through burrowing and surface feeding (Aller and Aller, 1998; Aller et al., 1996; Boudreau, 1986; Katsev et al., 2007; Michaud et al., 2005). Additional difficulty is imparted by the poorly characterized nature (chemical structure) and wide-ranging reactivity of sedimentary organic matter (LaRowe and Van Cappellen, 2011). Not only are the latter dictated by OM sources, but also by the depositional setting as well as the intensity and frequency of physical, biological and chemical reworking (Aller et al., 1996). Due to the large range of OM reactivities (half-lives ranging from

10 to 2000 years or longer (Hedges and Keil, 1995)), it is difficult to tease out the environmental and depositional factors that control OM preservation and degradation on the timescales of field observations or laboratory experiments.

This paper describes a long-term (250 days) incubation, carried out under different redox and amendment conditions, that assesses the fate of OM (partitioning, degradation, iron oxide association) over a longer timeframe than typical laboratory experiments. We systematically controlled the incubation conditions to more readily identify differences between oxic and anoxic OM degradation rates as well as the preservative interactions between OM and redox-sensitive minerals. A pulse of labile dissolved organic matter (DOM) derived from ^{13}C - and ^{15}N -depleted algae was added to a natural sediment slurry to study its degradation/preservation. Since there is little isotopic fractionation of the stable carbon isotopic signature ($\delta^{13}\text{C}$) during physical and biological processing of sedimentary OC and given that the $\delta^{13}\text{C}$ signatures of carbon sources are discrete and well constrained, $\delta^{13}\text{C}$ is a sensitive source indicator in this system (Bauer, 2002; Middelburg et al., 2000), allowing us to track the fate of the algal OM pulse within the solid and aqueous phases.

4.3. Materials and methods:

4.3.1. Sampling

Sediment samples were collected at 325 m depth at station 23 (48°42.419'N, 68°38.387'W) in the Lower St. Lawrence Estuary onboard the *R/V Coriolis II* in May 2011. The first \approx 20-25 cm of the grab core sample (fine silt/clay, porosity \approx 0.85) was homogenized, removing visible living macrofauna, seashells and detritus. The wet sediment was transferred to glass jars and stored on-board and in the laboratory at 4°C for less than 4 months in order to preserve the native microbial communities and chemistry of the sediment. The bulk of the sediment remained anoxic

during storage as only the surface of the sediment within the jar was in contact with the atmosphere.

4.3.2. Fresh algal dissolved organic matter

Algal dissolved organic matter (DOM) was liberated from *Nannochloropsis* algae cells (Reed Mariculture) through cell lysis following repeated freezing in liquid nitrogen and thawing. Lysed cells were diluted with deep Pacific seawater (DOM concentration $< 1 \text{ mg L}^{-1}$), centrifuged for 20 minutes at 19,000 g and filtered through a 0.7- μm glass fiber filter to generate a highly concentrated DOM solution. The algal-derived DOM is ^{13}C - and ^{15}N -depleted ($\delta^{13}\text{C} = -41.34 \pm 0.12\text{‰}$, $\delta^{15}\text{N} = -5.12 \pm 0.26\text{‰}$) relative to the natural sedimentary material ($\delta^{13}\text{C} = -24.29 \pm 0.10\text{‰}$, $\delta^{15}\text{N} = +5.67 \pm 0.22\text{‰}$), making it easy to follow its progressive integration into the sediment and degradation during the incubation. For example, a 6% addition of carbon and a 9% addition of nitrogen through the incorporation of algal DOC and DON, respectively results in a 1‰ depletion in sediment $\delta^{13}\text{C}$ and $\delta^{15}\text{N}$.

4.3.3. Slurry incubation setup

The incubation setup is illustrated in Figure 1. The 24 glass amber 250 mL vials (12 duplicate experimental conditions) were filled with wet homogenized sediment (14.6 g dry weight) in 175 mL of seawater giving a total volume of approximately 200 mL. Each vial was sealed with a custom designed PTFE cap lined with a Viton O-ring. Three ports were machined into the caps to accommodate standard PEEK fittings for gas purging and transfer as well as reagent additions. Three parallel sequences of 8 vials (4 amendment conditions done in duplicate) connected in series by PTFE tubing were incubated at 4°C under different redox conditions using a flow-through gas method ($\approx 30 \text{ mL min}^{-1}$). The first two series were maintained either oxic or anoxic

using air or nitrogen gas, respectively. The redox conditions in the third series of incubations alternated monthly between oxic and anoxic conditions for the duration of the experiment.

After one week of redox equilibration, each set of 8 vials was amended with fresh algal DOM (final concentration 36.1 mmol L^{-1}) and/or dissolved ferrous iron ($\text{FeCl}_2 \cdot 4\text{H}_2\text{O}$, final concentration 4.25 mmol L^{-1}), making 4 duplicate experimental scenarios: A. Addition of iron(II) and OM (Fe-OM scenario) B. Addition of iron (II) only (Fe scenario) C. Addition of OM only (OM scenario) and D. Control vials containing only the original sediment and seawater (Control scenario) (Fig. 4-1). Algal DOM and dissolved iron were injected as anoxic solutions through the septum port of each vial. Under oxic conditions, Fe(II) is expected to undergo rapid oxidation and precipitation as an iron oxide.

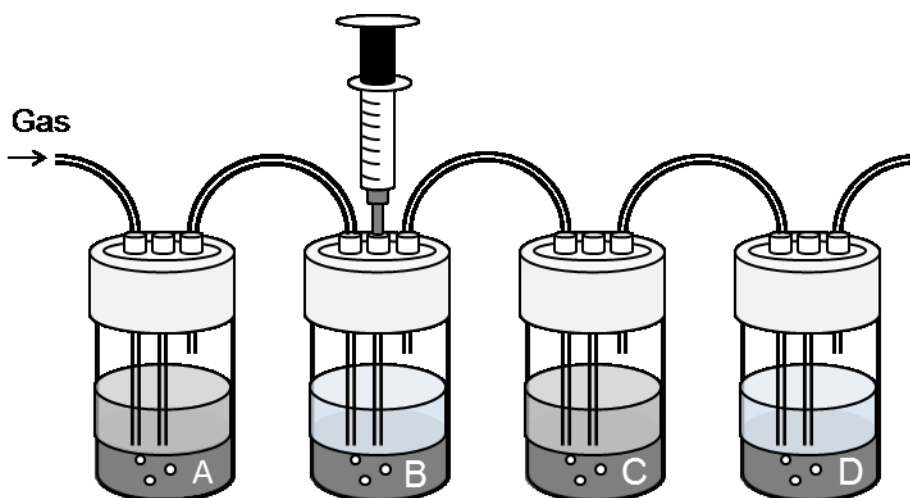


Figure 4-1: Illustration of the incubation setup. Incubations were carried out under 3 different redox conditions (anoxic, oxic, and mixed redox) by purging the overlying water with nitrogen gas, air, or alternating between the two gases. The sediment-seawater incubations were spiked with A) Fe(II) and DOM (Fe-OM scenario), B) Fe(II) only (Fe scenario), C) DOM only (OM scenario) and D) no addition (Control scenario). Note that each vial was duplicated (in series) in this experiment (8 vials per redox condition, 24 vials in total).

Aliquots (5 or 10 mL) of the well-mixed sediment-seawater slurries were extracted at various time intervals from each vial through the septum port using a syringe (shown in Fig. 4-1) and immediately transferred to centrifuge tubes. After centrifugation for 10 minutes (1000 g), the aqueous phase was isolated, acidified to pH < 2 for sample preservation and dissolved organic carbon (DOC) analysis, and stored at 4°C while the solid phase was freeze-dried and stored for later analysis. The overlying water pH at the end of the incubations was measured using an Accumet AB15 pH electrode calibrated using three NIST-traceable buffer solutions (3.95, 7.05 and 10.27 at 5°C).

4.3.4. Analyses

4.3.4.1. Solid Phase Measurements

The OC and TN content as well as the $\delta^{13}\text{C}_{\text{org}}$ and $\delta^{15}\text{N}_{\text{tot}}$ signatures of the solid phase were measured using a CHN analyzer (EuroVector 3028-HT) coupled to an isotope ratio mass spectrometer (IRMS, Isoprime GV Instruments). Prior to the %OC and $\delta^{13}\text{C}_{\text{org}}$ analyses, the samples were decarbonated by fumigation with 12 N HCl for 12 hours followed by a 1-hour heating step at 50°C and 6 hours in a desiccator to remove remaining water/acid.

Elemental and isotopic measurements were calibrated to IAEA-C6 sucrose ($\delta^{13}\text{C} = -10.45 \pm 0.03$), IAEA-N1 ammonium sulfate ($\delta^{15}\text{N} = 0.43 \pm 0.07\text{‰}$), and β -alanine (pre-calibrated in-house; $\delta^{13}\text{C} = -25.98 \pm 0.23\text{‰}$; C = 40.45% and $\delta^{15}\text{N} = -2.21 \pm 0.24\text{‰}$; N = 15.72%). The reproducibility of replicate measurements was better than 1% for OC and TN (relative error), and better than 0.3 and 0.5‰ for $\delta^{13}\text{C}$ and $\delta^{15}\text{N}$ signatures (absolute), respectively.

4.3.4.2. DOC concentrations and isotope analysis

DOC concentrations and $\delta^{13}\text{C}_{\text{DOC}}$ were measured simultaneously using a modified high-temperature catalytic oxidation TOC analyzer (OI Analytical Model 1010, College Station, TX) coupled to an isotope ratio mass spectrometer (IRMS, Isoprime GV Instruments) after acidification and purging of any dissolved inorganic carbon. The TOC analyzer's PTFE tubing was replaced with PEEK tubing to reduce the atmospheric CO_2 background. Repeated blank injections at 680°C under ultra-high purity O_2 (Praxair) were started 12 hours prior to sample analysis in order to desorb atmospheric CO_2 from the combustion column.

The injection volume was adjusted to $750\ \mu\text{L}$, producing enough CO_2 for accurate concentration and isotopic measurements, while maintaining efficient combustion. The CO_2 gas, generated from DOC combustion, was routed to a chemical CO_2 trap (Graden Instruments) before being cleaned of oxygen and sent to the IRMS using helium as the carrier gas. The concentration and $\delta^{13}\text{C}$ signature of the DOC were determined by calibrating the measured infrared peak area and $\delta^{13}\text{C}$ signature to solutions of IAEA-CH-6 certified sucrose and β -alanine. Duplicate sample measurements give a mean error of $\pm 2.15\%$ in DOC concentration (relative) and $\pm 0.15\%$ for the $\delta^{13}\text{C}$ signature (absolute).

4.3.4.3. Dissolved iron measurements:

Soluble iron was measured spectrophotometrically (Pharmacia Biotech Novaspec II) at $562\ \text{nm}$ using a modified version of the ferrozine method (Stookey, 1970). Briefly, each sample was filtered through a $0.2\ \mu\text{m}$ PTFE filter before adding $25\ \mu\text{L}$ of the hydroxylamine hydrochloride reducing agent ($1.40\ \text{mol L}^{-1}$), $100\ \mu\text{L}$ of the ferrozine complexing agent ($0.01\ \text{mol L}^{-1}$) and $50\ \mu\text{L}$ of a pH 5.5 ammonium acetate buffer ($1\ \text{mol L}^{-1}$, to maintain pH between 5 and 7). A solution of bathophenanthroline in isoamyl alcohol ($6\ \text{mmol L}^{-1}$) was used to strip off iron

contamination in the hydroxylamine reducing agent and buffer solution using a repeated (3x) solvent-solvent extraction. Using iron-extracted reagents, the limit of detection for this ferrous iron determination method is $0.3 \mu\text{mol L}^{-1}$ (Viollier et al., 2000) and the precision is better than $\pm 5\%$.

4.3.4.4. Tracking the fate of pulsed algal DOM

The incorporation and degradation of fresh algal DOC in the sediment and overlying water was quantified using a two-component mixing model (Eq. 4-3).

$$\delta^{13}\text{C}_{pooled} = f_{algal} \delta^{13}\text{C}_{algal} + (1 - f_{algal}) \delta^{13}\text{C}_{native} \quad (\text{Eq. 4-3}).$$

where the f_{algal} refers to the fractional contribution of algal OC to the total OC pool. As we have access to both solid phase and aqueous phase OC concentrations and their respective isotopic $\delta^{13}\text{C}$ compositions, we can trace the disappearance of the algal OC through decomposition, remineralization and gas phase transfer/escape from the system. This mass balance was done by calculating the fractional contribution of algal carbon in both the solution and solid phase at each sampling interval as a percentage of the initially added algal OC. Isotopic fractionation caused by the mineralization/alteration of components of the algal pool were not accounted for in isotopic mass balances as shifts in $\delta^{13}\text{C}$ are typically minimal ($\pm 1\%$, (Bauer, 2002)), in comparison to $\delta^{13}\text{C}$ differences between the algal tracer and native sediment OC.

4.3.4.5. Algal DOM partitioning coefficients:

Adsorption-desorption isotherms were constructed in order to derive equilibrium partitioning coefficients for algal DOC on oxic and anoxic sediments. Initial algal DOC concentrations of 0, 2, 4, 6, 8 and 10 mg L^{-1} were allowed to equilibrate with oxic surface sediments (0-0.5 cm) and

deeper anoxic sediments (10-15 cm) collected from the Lower St. Lawrence Estuary. Final DOC concentrations, after an equilibration period of 18 hours at room temperature (≈ 25 °C) and centrifugation (1000 g) of the slurry for 10 minutes, were measured using a high-temperature catalytic oxidation TOC analyzer. Using the slope of the adsorption isotherms, we derived equilibrium partitioning coefficients for the algal DOC ($K = \text{adsorbed concentration/dissolved concentration}$, in L g^{-1} dry weight).

4.3.4.6. Measurement of nitrogen in solution:

Dissolved nitrogen species were determined only on the final centrifuged sample of the time-series incubations owing to water volume constraints. Total dissolved nitrogen (TDN) was measured as nitrate after alkaline persulfate oxidation (0.075 g $\text{K}_2\text{S}_2\text{O}_8$ and 0.015 g NaOH per 10-mL sample) and autoclaving for 90 minutes (Arneel et al., 1993). Nitrate/nitrite and digested TN samples were analyzed by the cadmium reduction method using an automated Alpkem analyzer (Cattaneo and Prairie, 1995). The concentration of dissolved organic nitrogen was determined from the subtraction of the sum of nitrate and nitrite from TDN. Ammonium was not directly measured but is included within the dissolved organic nitrogen pool.

4.4. Results:

The incubation lasted 250 days and each vial was sub-sampled at irregular intervals with higher frequencies in the starting months. Dark, iron sulfide-rich sediments (pungent sulfidic odor) were produced under anoxic conditions in contrast to oxic and mixed redox sediments, which remained odorless and reddish-brown. The darkest sediment, and presumably the greatest amount of iron sulfide, was precipitated anaerobically when both iron and algal OM were added, as there was no shortage of either labile OM for sulfate reducing bacteria or reactive iron oxides for iron sulfide production. Dissolved iron concentrations were measured to verify that the

anoxic redox conditions were properly maintained throughout the incubation and during sampling. In the aerobic scenarios, soluble iron(II) concentrations were below detection limit within one week of the start of the incubations (all amendment scenarios). In contrast, under the anoxic scenario, there was progressive release of dissolved iron from the unamended, natural sediment (Control scenario), to a concentration slightly above $21 \mu\text{mol L}^{-1}$ (data not shown). Dissolved iron(II) concentrations decreased from $4250 \mu\text{mol L}^{-1}$ to about $290 \mu\text{mol L}^{-1}$ upon the addition of iron(II) chloride (Fe and Fe-OM scenarios) to the reactors maintained under anoxic conditions, demonstrating the strong affinity of iron(II) for sedimentary mineral surfaces (Burdige, 1993), its precipitation as sulfides throughout the incubation, as well as its oxidation to iron(III) by electron acceptors other than oxygen, such as manganese oxides and nitrate, at the start of the incubation (Magen et al., 2011). Dissolved iron profiles for all redox conditions of the control and iron-amended scenarios are available in section 2 of the Supplementary Material of this paper.

The pH remained circumneutral throughout the incubation; between 6.5 and 7.9 in the anoxic vials and between 7.3 and 7.9 in the oxic vials, within the range of pH conditions observed in natural sediment porewaters (Burdige, 2006). Under all conditions, the solution pH decreased progressively during the incubation from its initial seawater value ($\text{pH} \approx 8$) likely due to OM degradation, concomitantly releasing metabolic CO_2 and H^+ to the solution (Burdige, 2006; Mucci et al., 2000). These marginal shifts in pH do not modify the speciation (protonation/deprotonation) of OM functional groups, therefore abiotic processes such as adsorption, co-precipitation and aggregation are not affected (protonation of negatively charged functional groups such as carboxyls (pK_a 1.9-4.3) would cause an enhancement in the affinity of

DOM for particle surfaces whereas protonation of neutral groups such as histidine (pKa = 6.0) would reduce affinity).

4.4.1. Control and Fe Scenarios

Based on depositional data, the average accumulation age of the incubated sediments is already approximately 20-25 yrs (Smith and Schafer, 1999), therefore the OC and ON native to these sediments was not anticipated to be reactive during the timeframe of this relatively short incubation (250 days). The unreactive nature of the native sediment OM, relative to the timeframe of this incubation experiment, is demonstrated by the unchanging sediment OC and N content in the unamended control scenario (ranging from $1.54 \pm 0.01\%$ to $1.58 \pm 0.02\%$ for carbon and 0.163 ± 0.002 to $0.161 \pm 0.010\%$ for TN). Also reflecting the refractory nature of the native sediment OM, was the stability of the $\delta^{13}\text{C}_{\text{org}}$ and $\delta^{15}\text{N}_{\text{tot}}$ values in the control scenario which remained constant at $\delta^{13}\text{C} = -24.29 \pm 0.10\text{‰}$ and $\delta^{15}\text{N} = 5.67 \pm 0.22\text{‰}$ throughout the incubation.

The %OC and $\delta^{13}\text{C}$ of organic carbon in the solid phase of sediments supplemented with freshly precipitated iron oxides were statistically equivalent to control sediments throughout the incubation. However, the addition of Fe to the oxic and mixed redox condition caused a significant decrease in the sediment %TN from $0.163 \pm 0.002\%$ initially to $0.142 \pm 0.003\%$ under oxic conditions and $0.141 \pm 0.007\%$ under the mixed redox conditions, corresponding to a $11.65 \pm 4.83\%$ decrease in sediment nitrogen content respectively (Fig. 4-2). Removal of the native sediment nitrogen only occurred in the Fe amended scenarios under oxic and mixed redox conditions, and despite this loss of sediment nitrogen, no significant isotopic fractionation was observed ($\delta^{15}\text{N}$, $p = 0.0443$). It is noteworthy that under anoxic conditions and/or upon addition of the algal tracer this N removal process was not detected (Fig. 4-2).

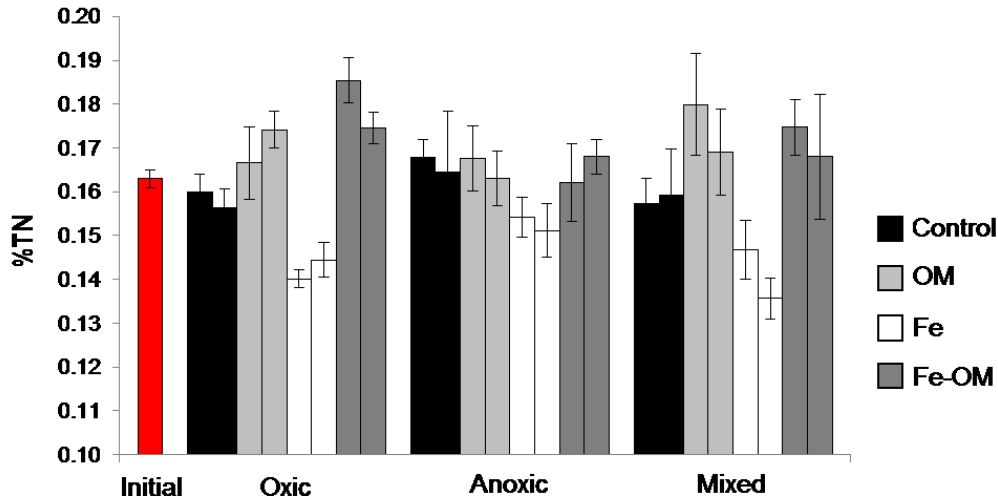


Figure 4-2 Final nitrogen concentration (%TN) of the sediment under different redox conditions for the different amendment scenarios.

In order to better understand the decrease in sediment nitrogen content in the iron amended (oxic and mixed redox) scenarios, the concentration of products formed during typical sediment N removal processes such as nitrite, nitrate and organic nitrogen were measured in the aqueous phase at the end of the incubation (Table 4-1). Nitrite was only detectable in the mixed redox incubation scenario, with the most abundant concentrations found for the Fe and Fe-OM scenarios. The highest nitrate concentration was detected in oxic and mixed redox conditions, but interestingly no nitrate was found in iron amended mixed redox incubation vials. Neither nitrate nor nitrite was detected in the anoxic redox conditions (Table 4-1). Total organic nitrogen, defined here as TDN - (nitrate + nitrite) (total organic nitrogen also includes dissolved ammonium, since ammonium was not measured directly), did not show any obvious relationship to redox condition or amendment.

Table 4-1: Concentrations of dissolved species at the end of the incubations (250 days, asymptotic value) in $\mu\text{mol L}^{-1}$. Standard deviations are shown in brackets when available.

	Oxic				Mixed				Anoxic			
	DON + NH ₄ ⁺	NO ₂ ⁻	NO ₃ ⁻	DOC	DON + NH ₄ ⁺	NO ₂ ⁻	NO ₃ ⁻	DOC	DON + NH ₄ ⁺	NO ₂ ⁻	NO ₃ ⁻	DOC
Control	122	<i>n.d.</i>	472	829 (200)	12	4	1042	1207 (143)	732	<i>n.d.</i>	<i>n.d.</i>	864 (329)
Fe	81	<i>n.d.</i>	490	557 (200)	107	256	<i>n.d.</i>	471 (143)	674	<i>n.d.</i>	<i>n.d.</i>	500 (100)
OM	388	<i>n.d.</i>	346	2214 (371)	122	11	821	2257 (271)	345	<i>n.d.</i>	<i>n.d.</i>	2629 (643)
Fe-OM	420	<i>n.d.</i>	321	921 (157)	459	201	843	764 (57)	217	<i>n.d.</i>	<i>n.d.</i>	2014 (693)

*n.d. = not detected

We also measured the DOC content of the control and Fe amended scenarios. Although the native sediment OM appears unreactive when looking at the solid phase carbon and nitrogen content, the composition of the slurry water is more sensitive to diagenetic changes with DOC concentrations drifting progressively during the course of the experiment from $233 \pm 75 \mu\text{mol L}^{-1}$ up to $1125 \pm 475 \mu\text{mol L}^{-1}$ across all control scenarios, mirroring the progressive release of OM from sediment particles. The Fe scenario follows a similar trend (climbing from $191 \pm 75 \mu\text{mol L}^{-1}$ to $594 \pm 208 \mu\text{mol L}^{-1}$) although DOC concentrations remain lower throughout the experiment, possibly showing increased partitioning of DOC onto solid particles. Final DOC concentrations are shown in Table 4-1 and all profiles of DOC concentration and $\delta^{13}\text{C}$ are shown in section 1 of the supplementary material.

4.4.2. OM Amended Scenarios

Despite the addition of fresh organic matter, the final sediment %OC in the OM amended incubation scenarios (OM and Fe-OM) are not significantly different from those of unamended scenarios (Control and Fe). However, the large differences in isotopic signature between the

native OM ($\delta^{13}\text{C} = -24.29 \pm 0.10\text{‰}$) and the OM tracer ($\delta^{13}\text{C} = -41.34 \pm 0.12\text{‰}$) allows the incorporation and retention of the algal OM to be tracked throughout the incubation using $\delta^{13}\text{C}$ measurements and isotopic mass balance calculations. For example, the incorporation of about 20% of the added algal tracer would cause an increase in the sediment OC content by 0.09%. This difference would not be detected from OC content measurements alone, as the average precision over the 4 final timepoints (%OC over these timepoints is stable), was $\pm 0.06\%$. An equivalent incorporation of the tracer would give rise to a significant drop in the bulk sediment $\delta^{13}\text{C}$ signature (1‰) compared to the average precision of the final timepoints for the bulk solid phase $\delta^{13}\text{C}$ measurements ($\pm 0.17\text{‰}$).

From the isotopic mass balance calculations about 50% of the added algal DOC was integrated into the solid phase within the first two hours of the amendment (First timepoint, Fig. 4-3). The initial algal OM incorporation was greater for the oxic Fe-OM scenario compared to all other OM amended scenarios and redox conditions (Fig. 4-3). The incorporated algal material had a C:N molar ratio of 5.13 ± 1.04 , this is slightly richer in nitrogen than the bulk algal C/N (7.58 ± 0.32). The degradation/disappearance of the algal tracer was monitored through the progressive recovery of the bulk $\delta^{13}\text{C}$ over the 250 days following amendment, starting at a fairly depleted signature (tracer/native OM mix) to a signature that approaches that of the native sediment. At the end of the incubation the $\delta^{13}\text{C}$ signature of the solid phase was $-25.08 \pm 0.12\text{‰}$ for all OM amended scenarios (Fig. 4-4). This significant depletion in $\delta^{13}\text{C}$ compared to the native sediment OM corresponds to a retention of $10.91 \pm 2.49\%$ of the total added algal OC at the end of the incubation (Fig. 4-3 and 4-4).

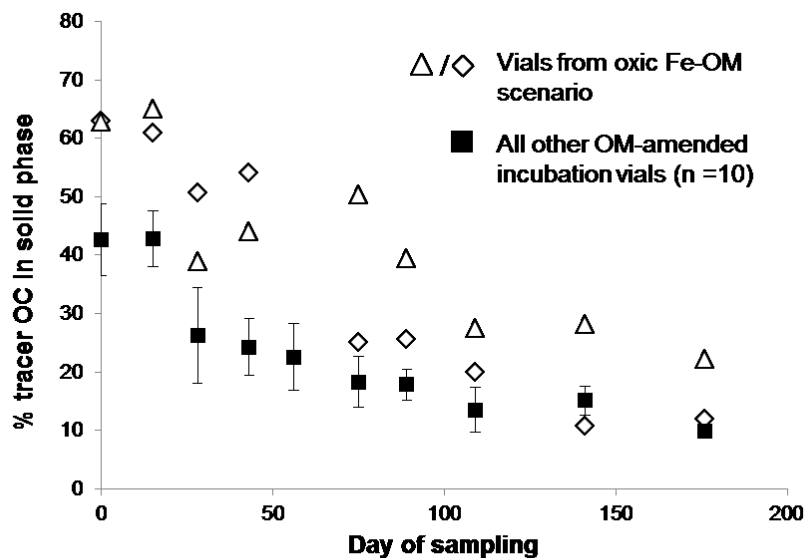


Figure 4-3: Incorporation of the algal tracer in the sediment for OM and Fe-OM scenarios based on carbon isotope mass balance calculations. Black squares show the average incorporation of all redox conditions except the oxic Fe-OM scenario. White diamonds and triangles each represent a duplicate vial of the oxic Fe-OM condition. Error bars represent standard deviation.

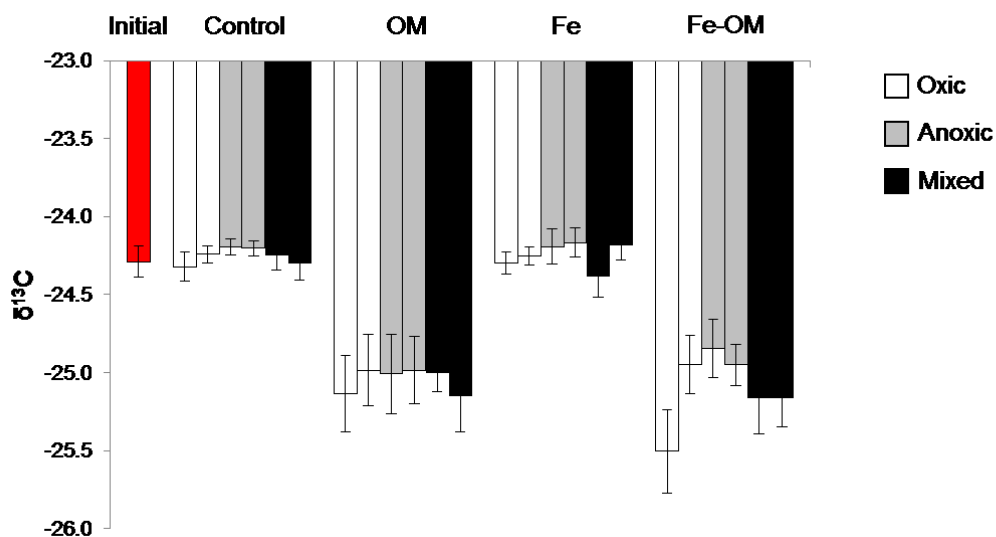


Figure 4-4: Final stable carbon isotope signature ($\delta^{13}C_{org}$) of the sediment (last 4 time points). Error bars represent the standard deviation of the last 4 time points.

The concentration of the algal tracer in solution decreases throughout the incubation, following first order kinetics down to a stable (Fig. 4-5, Appendix 2), asymptotic value, attained within 30 to 150 days of the start of the incubation, depending on redox condition (Table 4-2). The half-life of DOC is 2 to 3 times shorter under oxic rather than anaerobic conditions. Oscillating redox conditions causes a segmented decrease in DOC concentration with an abrupt increase in DOC consumption following the switch from anoxic to oxic conditions. Rate constants and half-lives corresponding to the mixed redox condition were therefore not included in Table 4-2. The rate of DOC decomposition of the algal tracer is similar to rates reported for porewater DOC from seasonally anoxic shallow sediments (Burdige, 2002) but much faster than the more recalcitrant porewater DOC collected typical coastal sediments (Burdige, 2002; Komada et al., 2013).

Despite stable DOC concentrations within the asymptotic segment, $\delta^{13}\text{C}$ drifts from the depleted signature of the tracer ($-41.34\text{‰} \pm 0.12\text{‰}$) to a more enriched signature ($-33.4\text{‰} \pm 0.53\text{‰}$), demonstrating partial degradation, release and desorption of soluble material from the native sediment organic matter ($\delta^{13}\text{C} = -24.29 \pm 0.10\text{‰}$) into solution.

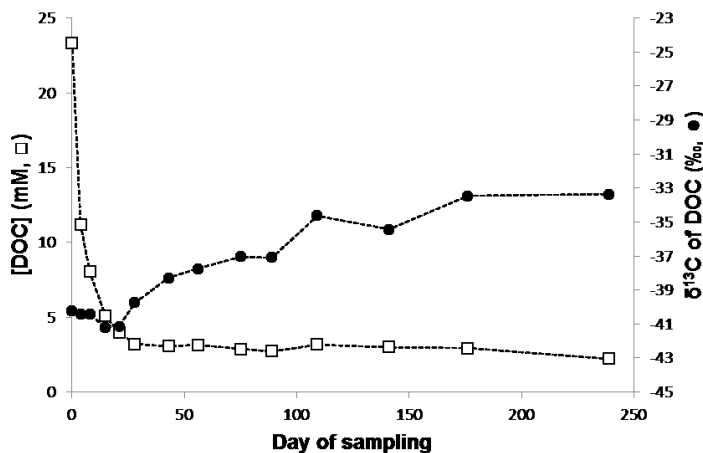


Figure 4-5: Temporal evolution of the DOC concentration and isotopic signature ($\delta^{13}\text{C}_{\text{DOC}}$) in duplicate incubation vials (OM scenario, oxic conditions).

Table 4-2: Pseudo first-order degradation rate constants and half-lives of DOC in oxic and anoxic incubations. Standard deviations are shown in brackets.

	Oxic				Anoxic			
	Fe-OM		OM		Fe-OM		OM	
Rate constant (d ⁻¹)	0.061	(0.0014)	0.068	(0.0014)	0.032	(0.0058)	0.019	(0.0035)
half-life (d)	11.46	(0.28)	10.25	(0.22)	21.46	(3.88)	37.28	(7.16)

4.5. Discussion

4.5.1. Role of iron in OM preservation and DOM shuttling:

Nearly two decades ago, Keil et al. (1994) and Mayer (1994) hypothesized that sorption of OM to mineral surfaces stabilizes the sorbed molecules, a mechanism that was proposed to account for the enigmatic preservation of intrinsically labile organic compounds in marine sediments, such as those in our algal tracer. This hypothesis was founded on the strong association of sedimentary OM with the mineral matrix. Mechanistically, the process of adsorption implies that the particulate OM reaching the seafloor initially undergoes degradation and is broken into smaller, soluble fragments that readily adsorb to mineral phases (Hedges and Keil, 1995) or can co-precipitate with metal oxides at anoxic/oxic interfaces (Lalonde et al., 2012). Algal DOM, injected into the overlying water of the incubated sediments, was rapidly incorporated into the solid phase, leading to a shift in the sediment's stable carbon isotope signature. Isotopic mass balance calculations reveal that approximately 50% of the added DOC was incorporated within the first two hours (Fig. 4-3). The rapid timeframe for this incorporation is consistent with adsorption or co-precipitation (with metal oxides) of the algal DOM into the solid sediment phase (Fig. 4-6, pathways 1 & 2), in agreement with previous studies (Arnarson and Keil, 2000; Berner, 1980). Note that the incorporation of the algal tracer was also accompanied by an

increase in the day to day scatter as well as the variability in solid phase $\delta^{13}\text{C}$ measurements between twin vials (OM and FeOM scenarios: $\sigma = 0.36\text{‰}$; versus control and Fe scenarios: $\sigma = 0.093\text{‰}$), which could be attributed to the heterogeneous distribution of algal DOC on sediment particles.

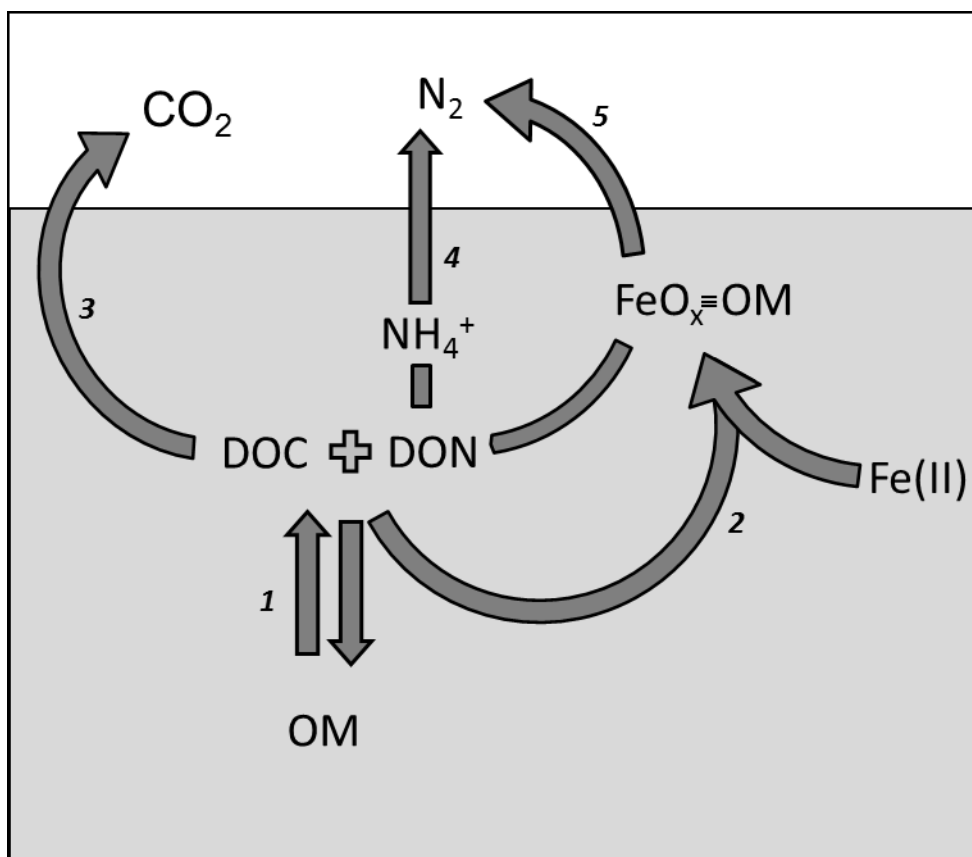


Figure 4-6: Simplified pathways of DOM incorporation (1. Adsorption/Desorption and 2. Co-precipitation during Fe(II) oxidation) 3. Organic carbon remineralization to CO₂, 4. Bacterial denitrification/anammox, and 5. Iron mediated N₂ production) in marine sediments.

Irreversibly mineral-bound molecules are more likely to resist prolonged degradation (>250 days) and thus account for the $\delta^{13}\text{C}$ signature of algal OM preserved in the incubated sediment. The final incubation time-series sample (250 days) shows the retention of approximately 10% of the total added algal OC (OM and Fe-OM scenarios) (Eq. 4-1 and Fig. 4-4). DOM surface

binding is controlled by the availability of sorption sites which is likely a function of sediment particle surface area (Mayer, 1994; Mayer, 1995) as well as mineralogy (Lalonde et al., 2012; Ransom et al., 1998b). Hydroxylated iron and manganese oxides are known to strongly adsorb and retain soluble organic compounds through ligand-exchange and inner-sphere complexation (Gu et al., 1995; Ransom et al., 1998b). These surface interactions favour nitrogen and oxygen-rich organic molecules which typically carry more functional groups that bind covalently to mineral surfaces (Arnarson and Keil, 2000). This preference of electronegative groups possibly explains why the composition of the preserved OM is different from that of the bulk algal DOM with C:N molar ratio of the fraction of the algal material incorporated into the sediment at 5.13 ± 1.04 , which is slightly richer in nitrogen than the bulk algal C/N (7.58 ± 0.32).

To further probe the effect of metal oxides on DOM binding in natural sediments, we derived equilibrium partitioning coefficients ($K = \text{adsorbed concentration/dissolved concentration}$, in L g^{-1} dry weight) for algal DOC adsorbing to iron oxide-rich surficial sediment (0-1 cm depth) and underlying anoxic sediments (10-13 cm depth). K values of surficial sediments ($0.038 \pm 0.0075 \text{ L g}^{-1}$) exceed those of the underlying anoxic deposits ($0.0052 \pm 0.00036 \text{ L g}^{-1}$) approximately 8-fold, indicating that authigenically-produced metal oxides greatly increase DOM partitioning onto solid surfaces. Reactive iron oxides, produced in our oxic incubated slurries upon amendment with Fe(II), also promote the transfer of DOC to particle surfaces, lowering DOC concentrations most likely through sorption or co-precipitation of DOM (Table 4-1; the reader should compare Fe to Control scenarios as well as Fe-OM to OM scenarios). The efficacy of solution-solid transfer by metal oxides possibly affects the turnover of carbon and nitrogen in natural sediments through the modification of DOM fluxes through oxide-rich surface sediments and the enhancement of OM preservation (Lalonde et al., 2012). Once sorbed to the solid phase,

molecules become more resistant to microbial decay since only DOC is amenable to bacterial uptake (only molecules <600 Da can cross cell membranes through porins; Arnosti, 2011) and degradation (Fig. 4-6, pathway 3). Molecules that are only weakly-bound to the sediment are shuffled between the particulate and aqueous phase, which over time leads to their degradation (Henrichs, 1995) (Fig. 4-3 and 4-5).

The make-up of porewater DOC is likely altered by re-equilibration with the much larger mineral-bound OC pool (Hedges and Keil, 1995). The relationship between the dissolved and solid OC pools is however seldom obvious and can be further obscured by transport processes that lead to the addition or removal of DOC (diffusion, bioirrigation, remineralization) and particulate OC (sedimentation, burial, bioturbation) (Berner, 1980). The use a ¹³C-depleted isotopic algal tracer allows us to circumvent some of the intrinsic complexity of the sediment and to demonstrate the sorption of dissolved and colloidal (<0.7 μm) organic molecules onto sediment particles (Fig. 4-6, pathways 1 & 2), as well as to track its decomposition and mineralization from both the solid sediment and the aqueous phase.

The degradation of our algal tracer in the aqueous phase (Fig. 4-5 and Fig. 4-6, pathway 3) follows first-order kinetics down to asymptotic but variable DOC concentrations. These final concentrations vary with redox conditions and amendment scenario (Table 4-1) with the lowest concentrations found in oxic and mixed redox conditions. The final asymptotic concentrations observed in these incubations are analogous to the constant DOC concentrations found at depth in sediment cores which result from (i) the production of DOC at these depths being equal to its consumption or (ii) the production and consumption of DOC at depth approaches zero, entailing that porewater DOC at depth is effectively unreactive and therefore preserved indefinitely (Burdige, 2002). In this work, we show a gradual substitution of algal DOC by reversibly-bound

autochthonous OC through $\delta^{13}\text{C}_{\text{DOC}}$ measurements (increasing $\delta^{13}\text{C}_{\text{DOC}}$ signature, implying the release of native OM into sediment porewaters; Fig. 4-5). This is the first direct demonstration of a surface exchange between porewater DOM and adsorbed OM and supports a steady-state condition of production/consumption of porewater DOC. Labile algal molecules are more amenable to bacterial decomposition, which allows more recalcitrant native molecules to become a more important fraction of porewater DOC and leads to an overall decrease in the reactivity of porewater DOM over the timeframe of the incubation.

First order degradation kinetics of the algal marker is consistent with most early diagenetic models (Berner, 1980). All incubation conditions had a pool of DOM that was essentially unreactive during the course of the experiment (corresponding to the final asymptotic DOC concentration, Fig. 4-5). As consumption equals production during the asymptotic segment (the overall rate of DOC disappearance is zero), asymptotic/refractory DOC concentrations can be subtracted from rate calculations. We began measuring the kinetics of OM degradation at the second timepoint (day four), excluding microbial degradation of the extremely labile DOM pool (this DOM pool is typically respired in the water column before reaching the sediment and is not representative of typical marine sedimentary OM) as well as adsorption/desorption of DOM (reaching equilibrium within 2-3 hours (Arnarson and Keil, 2000)) from rate calculations. These processes are rapid compared to the degradation of the added OM tracer, making them negligible in the degradation rate calculation (Berner, 1976). According to first order kinetic rate laws ($dC/dt = -kC_t$), rate constants (k) and half-lives ($t_{1/2} = \ln(2)/k$) for algal DOC were determined for the different redox and amendment conditions (Table 4-2). The half-life of DOC is 2 to 3 times shorter under oxic rather than anaerobic conditions. This, along with lower asymptotic DOC concentrations measured in the oxic and mixed redox conditions (Table 4-1), likely results from

more effective utilization of the DOC produced during mineralization by oxic bacteria (Burdige, 2002). Anaerobic decomposition of DOM is less efficient, requiring a consortium of bacteria; with fermenters, for example, supplying DOM substrates to sulfate reducers (Burdige, 2006).

Results of our incubation experiments demonstrate the preservative effect of iron oxides on sediment-bound organic matter through increased OM retention and reduced microbial degradation likely owing to strong complexation (Lalonde et al., 2012). The highest OM incorporation of the algal tracer occurred as a result of DOM-iron co-precipitation upon amendment with both iron and algal OM under oxic conditions when compared to all other conditions (Fig. 4-3, first time points). The incorporation of DOM into the solid phase results in slower decomposition as microbial degradation is inhibited by the formation of strong bonds to the solid phase. Within natural systems, the preservative effect of iron oxides could allow for the transfer of iron-OM complexes to anoxic sediment layers where OM may be sequestered over geological timescales. The overall extent of OM degradation (observed from the loss of the depleted $\delta^{13}\text{C}$ signature of the algal tracer) is independent of redox conditions as seen by the converging % tracer OC time series (Fig. 4-3, final time points), indicating that even OM strongly bound to iron oxides or other minerals is sensitive to degradation upon continuous exposure to oxygen. Prolonged oxygen exposure is known to lead to the nearly complete degradation of OM, regardless of the extent of physical protection, as seen by the low OC content of turbidites above the oxidation front (Colley et al., 1984; Cowie et al., 1995; Prahl et al., 1997; Thomson et al., 1998).

4.5.2. Accelerated iron-mediated nitrogen removal:

At the end of the incubation period, total dissolved nitrogen (TDN) concentrations were lower than 1.5 mmol L^{-1} and therefore can be excluded from mass balance calculations ($< 4\%$ of the

total mass balance; Table 1). No detectable nitrate or nitrite was measured under anoxic conditions demonstrating the absence of nitrification during ON remineralization or the fast consumption of nitrate/nitrite in the absence of oxygen. Nitrate was the predominant dissolved nitrogen species under oxidizing conditions. In contrast to the other redox conditions, both dissolved nitrate and nitrite were present in the alternating redox system (anoxic at the time of the measurement), with the amended Fe and Fe-OM scenarios having the highest NO_2^- concentrations (Table 4-1).

Without the addition of reactive iron surfaces, solid ON that is native to the sediment is unreactive; no net losses of solid-phase TN were detected in the control incubation under any of the redox conditions. Losses of N as N_2 (sum of all biotic and abiotic denitrification pathways) from the incubation vials can be estimated as the difference between the total initial mass of N (control and amendment scenarios) and the final mass of N (residual solid phase N plus dissolved N species produced upon mineralization of solid-phase organic N, nitrite, nitrate, ammonium and dissolved organic N). The addition of Fe(II) caused the removal of $11.65 \pm 4.83\%$ of the original sediment nitrogen (Fig. 4-2), with the highest losses occurring under oxic and mixed-redox conditions, where iron(II) is immediately precipitated as reactive iron oxides. Bacteria participating in denitrification/anammox are confined to anoxic environments (under $4 \mu\text{mol O}_2 \text{L}^{-1}$ for denitrification and under $10 \mu\text{mol O}_2 \text{L}^{-1}$ for anammox) (Crowe et al., 2012; Hulth et al., 2005) therefore making these biochemical pathways unlikely in oxygenated incubation vials. Traditional nitrification/denitrification pathways in fact require both oxic (for nitrification) and anoxic conditions (for denitrification) to take place. To account for fixed-N deficit observed in our oxic incubations, an alternative biochemical N degradation pathway is required. Luther et al. (1997) were the first to propose a direct mechanism for N_2 production

from NH_4^+ oxidation, coupled to manganese oxide reduction, “short-circuiting” the traditional N intermediates. Though they proposed that this mechanism is also possible using iron oxides as substrates, they did not demonstrate that this reaction occurs. The reason for proposing a link between the N and Mn elemental cycles likely arose from the similarity in the standard reduction potential of NO_3^- and MnO_x (Froelich et al., 1979), (therefore the proximity of nitrate and MnO_x reduction zones in sediments). However, despite the lower free energy yield (Froelich et al., 1979), there is a 1-2 order of magnitude greater abundance of reactive Fe compared to Mn in the St. Lawrence Estuary and Gulf sediments (Anschutz et al., 2000) and in most other coastal sediments (Mason, 1966). Since the highest abundance of reactive iron oxides is within the oxygen and NO_3^- reduction zones in all coastal sediment cores (Burdige, 1993), we propose that the iron oxide-ammonium redox couple is equally if not more likely to exist than the manganese oxides-ammonium redox couple. Our N mass balances under oxic conditions and the observed losses of native sediment N in the presence of added reactive iron oxides (Fig. 4-2 and Fig. 4-6, pathway 5) possibly demonstrate *in-vitro* evidence of Luther’s and Yang’s proposed aerobic iron-mediated ammonium oxidation pathway.

No significant isotopic fractionation of TN was observed upon nitrogen loss in iron-amended slurries, in contrast to traditional bacterial denitrification pathways that lead to $\delta^{15}\text{N}$ enrichment of the residual nitrogen pool (Mariotti et al., 1981), possibly supporting the occurrence of an alternative N_2 -production mechanism. Iron oxide-mediated mechanisms of NH_4^+ oxidation have been documented in wetland soils (Clément et al., 2005) and wastewater treatment plants (Sawayama, 2006), but their occurrence in marine sediments have yet to be demonstrated.

Proposed mechanisms of NH_4^+ oxidation by Fe(III) (known as Feammox producing either N_2 or NO_2^-) involve (i) NH_4^+ oxidation at reactive iron oxide surfaces, and/or (ii) NH_4^+ oxidation by O_2

from iron oxide surfaces (Yang et al., 2012). Notably, both of these mechanisms can be mediated by sedimentary iron oxides and can be biotic or abiotically-mediated (Luther III et al., 1997). The high NO_2^- concentrations, observed under our iron amended mixed redox incubations are consistent with the iron oxide-induced oxidation of NH_4^+ to NO_2^- proposed by Yang et al. (2012), although they could also result from the decoupling of NO_2^- production from its consumption in these sediments. More work, involving the monitoring of N_2 gas production in sediments spiked with ^{15}N labelled nitrogen substrates alongside dissolved Fe is necessary to positively identify Feammox in sediments.

Along with the algal OC, ON was incorporated into the sedimentary phase. However unlike $\delta^{13}\text{C}$, $\delta^{15}\text{N}$ is sensitive to fractionation during biochemical pathways such as denitrification, and could not be used as a tracer for algal OM degradation. %TN values do however indicate that, in contrast to Fe amendment scenarios, accelerated TN losses were not observed in the Fe-OM amendment scenarios (Fig. 4-2). We propose that this occurs from the shielding of iron oxide surfaces by sorbed fresh OM, which is known to poison iron oxide surfaces in natural conditions and inhibit crystal growth (Schwertmann, 1966), therefore blocking the reactive, hydroxylated iron oxide surfaces from binding other species or being used as catalysts for reactions such as Feammox. The active diagenetic recycling of iron oxides in sediments regenerates reactive iron surfaces (Burdige, 2006) that potentially promotes these reactions. This same surface site inhibition might also occur in the unamended sediment incubations (Control scenario), where nitrogen losses were not detected throughout the 250 day incubation, though it is possible that nitrogen removal reactions may be occurring at rates that are too slow to cause detectable losses in the solid phase. In natural sediments, such as the ones used in these incubations, much of the iron oxide surfaces are also bound to organic molecules. If Feammox and other oxide-mediated

diagenetic pathways such as dissimilatory iron and manganese reduction require unpoisoned oxide surfaces, it is possible that these reactions might be confined to the oxic-anoxic sediment interface, where fresh metal oxides precipitate.

4.6. Conclusions and implications

Organic matter (OC and ON) degradation and preservation are intimately related to other elemental cycles such as those of oxygen, iron and sulfur. Iron plays multiple roles in OM cycling: ferric iron serves as an electron-acceptor in the respiration of OM (Burdige, 1993), but also increases the preservation potential of sedimentary OC through adsorption/complexation. Iron's preservative effect is twofold, shuttling OM from the dissolved to the solid phase in the sediment and, upon burial, from the oxic sediment surface to the deeper anoxic layers, as well as increasing its resistance to microbial decay through strong iron-OM complexation. In combination, these two processes can account for the preservation of up to 20% of the OC in marine and freshwater sediments, thus contributing significantly to the global redox balance (Lalonde et al., 2012).

Interesting preliminary data demonstrates accelerated removal of fixed nitrogen species in the presence of iron oxides in marine sediments though further work must be undertaken to elucidate the exact chemical/biochemical nature of this process. With denitrification in marine sediments as an important component of the global nitrogen cycle, accounting for about half of the oceanic nitrogen removal (Christensen, 1994), it is intriguing to consider that iron may play a role in regulating the oceanic production of reactive nitrogen species as well as controlling nitrogen removal through generation of N_2 , all the while slowing the degradation of OC through the formation of strong Fe-OM complexes. This effective decoupling of the organic carbon and nitrogen elemental cycles is intertwined to the generation of reactive iron oxides, transported to

sediments through continental erosion (Burdige, 2006). This experiment also shows the usefulness of a multi-pronged tracer-based incubation approach to study and model coupled elemental cycles with processes occurring over different timescales that involve labile and refractory components.

Chapter 5: Preservation of organic matter in marine sediments by inner-sphere interactions with reactive iron

Andrew Barber¹, Jay Brandes², Alessandra Leri³, Karine Lalonde¹, Kathryn Balind¹,
Sue Wirick⁴, Jian Wang⁵, and Yves Gélinas^{1*}

¹GEOTOP and the Department of Chemistry and Biochemistry, Concordia University, 7141 Sherbrooke West, Montréal, Quebec, H4B 1R6, Canada.

²Skidaway Institute of Oceanography, University of Georgia, 10 Ocean Science Circle, Savannah, GA 31411, USA.

³Department of Natural Sciences, Marymount Manhattan College, 221 E 71st St., New York, New York 10021, USA.

⁴National Synchrotron Light Source, Brookhaven National Laboratory, Upton, NY 11973, USA

⁵Canadian Light Source Inc, Saskatoon, Saskatchewan S7N 0X4, Canada

*Correspondence to:

Yves Gélinas

E-mail: yves.gelinas@concordia.ca

Phone: 514-848-2424 (3337)

5.1. Abstract

Interactions between organic matter and mineral matrices are critical to the preservation of soil and sediment organic matter. In addition to clay minerals, Fe(III) oxide particles have recently been shown to be responsible for the protection and burial of a large fraction of sedimentary organic carbon (OC). Through a combination of synchrotron X-ray techniques and high-resolution images of intact sediment particles, we assessed the mechanism of interaction between OC and iron, as well as the composition of organic matter co-localized with ferric iron. We present scanning transmission x-ray microscopy images at the Fe L₃ and C K₁ edges showing that the organic matter co-localized with Fe(III) consists primarily of C=C, C=O and C-OH functional groups. Coupling the co-localization results to iron K-edge X-ray absorption spectroscopy fitting results allowed to quantify the relative contribution of OC-complexed Fe to the total sediment iron and reactive iron pools, showing that 25-62% of total reactive iron is directly associated to OC through inner-sphere complexation in coastal sediments, as much as four times more than in low OC deep sea sediments. Direct inner-sphere complexation between OC and iron oxides (Fe-O-C) is responsible for transferring a large quantity of reduced OC to the sedimentary sink, which could otherwise be oxidized back to CO₂.

5.2. Introduction

As the largest sink for organic carbon (OC) on Earth, marine sediments play a major role in the global carbon cycle (Hedges and Keil, 1995). The majority of the OC preserved within sediments is intimately associated to the mineral matrix through sorption on clay minerals and metal oxides (Keil et al., 1994; Mayer, 1994a; Hedges and Keil, 1995; Bock and Mayer, 2000; Arnarson and Keil, 2007). In particular, redox sensitive, nano-scale iron oxides have a strong affinity for OC (Morel, 1993), forming stable Fe-OC complexes that can persist for thousands of years in anoxic

sediments at depths of up to 5 m (Lalonde et al., 2012). These high surface area-to-volume ratio particles readily bind OC and increase its stability, transport and sequestration in sediments (Morel, 1993; Kaiser and Guggenberger, 2003). As such, reactive iron oxides (defined as dithionite reducible iron oxides) constitute a “rusty sink” that accounts for the preservation of $21.5 \pm 8.6\%$ of sediment OC in the global ocean (Lalonde et al., 2012). These Fe-OC interactions must be practically irreversible under natural conditions to account for the long-term preservation of reactive OC (Henrichs, 1995) since reversible binding (i.e., cation bridging, hydrogen bonding, van der Waals and hydrophobic interactions) eventually leads to the solubilisation of OC, ultimately resulting in its enzymatic hydrolysis and biodegradation (Burdige, 2006; Burdige, 2007).

The interactions between Fe and OC in natural settings have been extensively studied in the past, but most research has been conducted using model OC compounds and preformed iron oxides in experiments that cannot fully mimic sediment redox boundaries/microenvironments, formation conditions, the timescales of carbon cycling or the diversity of species participating in these interactions. Iron oxides, for example, can be detrital (preformed lithogenic particles sedimenting from the water column) or authigenic (formed *in-situ* through the oxidation of pore water Fe^{2+} in the presence of OC). Complexation of OC and iron oxides at the sediment redox boundary can result in strong inner-sphere interactions (Keil and Mayer, 2013), poisoning the crystal structure of iron oxides (Zee et al., 2003), while also stabilizing reactive OC. These strong inner-sphere Fe-O-C chemical bonds, also referred to as covalent interactions, act in consort with other sedimentary mechanisms (i.e., sorption by clays, geopolymerisation, intrinsic recalcitrance, and physical protection by biominerals (Hedges and Keil 1995)) to transfer large quantities of

reduced OC from the active surface of the globe to its slowly cycling interior where it remains locked on geological time scales.

Sequential extraction methods used to probe iron-OC interactions involve harsh chemical treatments that target operationally defined iron fractions (Tessier et al., 1979; Lord III, 1982; Poulton and Raiswell, 2005), with the OC:Fe molar ratio of the extracted material being used to infer molecular-level interaction mechanisms (Raiswell and Canfield, 2012; Lalonde et al., 2012). The use of ratios however assumes that the entire iron pool is bound to OC, neglecting the possibility that only a fraction of the extracted reactive Fe is associated with OC. While measuring the percentage of total OC associated to Fe is straightforward (Lalonde et al., 2012), obtaining the percentage of total reactive Fe directly complexed to OC is more challenging.

Here we use Fe K-edge X-ray Absorption Near Edge Structure (XANES) spectroscopy to quantify the proportion of reactive Fe involved in inner-sphere complexation to OC in contrasting sedimentary environments. In conjunction with the XANES spectroscopy, key organic functional groups co-localized with ferric iron were identified using X-ray spectromicroscopy at the C K-edge and Fe L₃-edge. We probed for the first time the actual preservative interactions occurring between iron and OC in chemically unaltered sediments.

5.3. Materials and Methods

5.3.1. Samples

The samples comprise sediments of different composition, accumulating in contrasting depositional regimes under varying redox conditions (Table 5-1). They include highly oxidized, OC poor (<0.33 wt%) pelagic sediments (Equatorial Pacific red clays at 9°N, Equatorial Pacific carbonates at 0°N, an opal-rich sediment from the Southern Ocean, and a highly oxidized

turbidite from the Madeira Abyssal Plain off the Moroccan Coast – MAP2). Also included are a series of coastal samples accumulating under varying redox conditions: Arctic Margin sediments from oxygenated bottom waters close to the Mackenzie River delta, Mexican Margin sediments accumulating under oxic (station 305) and suboxic (station 306) bottom waters conditions offshore from the city of Mazatlan, sediments underlying the perennially hypoxic bottom waters of the St-Lawrence Estuary (Quebec, Canada), oxic sediments collected in the Arabian Sea off the coast of Oman, the seasonally anoxic Saanich Inlet (British Columbia, Canada), and the sulfidic Black Sea samples.

Sediments from oxygen limited (Saanich Inlet and Mexican Margin) and sulfidic environments (Black Sea) have higher OC content compared to the other sediments included in this study (Table 5-1). Of particular interest to this study is the nature of the organic matter which is deposited in these sediments with the Saanich and Mexican Margin samples being dominated by mostly marine inputs while the Black Sea is dominated by terrestrial organic inputs, as shown by their higher atomic C/N ratio and more depleted $\delta^{13}\text{C}$ signatures (Table 5-1). The remaining coastal sediment samples were chosen to represent a wide range of depositional settings along the terrestrial-marine continuum.

5.3.1. Sediment Organic Carbon Content Determination

Sediments were first decarbonated overnight in an acid (12N HCl) fumigation chamber, followed by gentle drying for 1 hour. The organic carbon content of the decarbonated sediment was determined using a CHN analyzer (EuroVector 3028-HT) using β -alanine (40.4% OC) as a calibration standard.

Table 5-1. Composition of the samples and raw sediment Fe K-edge Linear combination fitting results

Sediment	Total OC content (wt%)	C/N ^(a)	$\delta^{13}\text{C}$ (‰)	Sediment total Fe content (mg Fe/g sed)	Free iron oxide contribution to total sediment Fe (wt%)	Iron-OM complex contribution to total sediment Fe (wt%)	Residual non-reactive Fe contribution to total sediment Fe (wt%)	Sum of all fitting components (%)	OC bound to Fe ^(b) (% of total OC)
Saanich Inlet	2.21	7.51	- 22.4	23.1	10.8 ± 2.2 ^(c)	18.1 ± 2.6	72.0 ± 4.9	101	28.09
Arabian Sea	1.11	8.04	- 21.6	17.3	26.5 ± 7.1	16.6 ± 6.3	57.4 ± 1.6	101	26.89
Madeira Abyssal Plain turbidite	0.29	15.04	- 21.9	39.8	68.6 ± 5.7	12.5 ± 6.1	11.7 ± 1.6	93	NA
Black Sea	4.61	15.69	- 26.6	33.3	0.0 ± 3.7	8.1 ± 1.0	90.4 ± 3.4	99	24.98
Mexican Margin (Station 306)	6.66	9.27	- 22.1	30.7	15.1 ± 1.9	7.8 ± 0.7	74.6 ± 2.3	98	22.31
Mexican Margin (Station 305)	2.82	9.00	- 21.5	35.4	19.4 ± 5.0	6.7 ± 0.6	76.0 ± 2.2	102	12.70
Southern Ocean	0.33	8.27	- 20.8	7.7	14.8 ± 4.9	5.3 ± 0.9	82.2 ± 3.9	102	29.00
St. Lawrence Estuary	1.43	12.83	- 24.3	32.6	12.8 ± 0.4	5.1 ± 1.3	80.6 ± 1.6	99	25.13
Equatorial Pacific 0°N	0.27	8.26	- 21.6	3.2	40.4 ± 5.1	- ^(d)	61.1 ± 1.1	102	34.79
Arctic Margin	1.18	7.35	- 26.2	50.9	41.1 ± 3.5	-	56.9 ± 1.3	98	7.60
Equatorial Pacific 9°N	0.30	4.58	- 22.4	35.7	13.9 ± 2.0	-	87.6 ± 4.6	102	12.16

^(a) Atomic C/N ratio

^(b) Percent of total sediment OC associated to reducible iron oxides taken from (7)

^(c) 1 σ errors for the fitting results

^(d) Component not used in the combinatorial linear fitting calculations

5.3.2. Synthetic Fe hydroxides and OC:Fe Complexes

Ferric oxalate ($C_6Fe_2O_{12}$), purchased from Sigma-Aldrich Canada, was used as an inner-sphere OC-substituted Fe(III) model compound. Lepidocrocite ($\gamma\text{-FeO(OH)}$), an OC-free ferric hydroxide, was synthesized following the procedure of Cornell and Schwertmann (Schwertmann and Cornell, 2000). Briefly, ferrous chloride was added in solution and precipitated out as ferric hydroxide through the dropwise addition of 1 M NaOH, maintaining circumneutral pH, while continuously bubbling O_2 through the solution. Precipitation of iron hydroxides was also performed in the presence of varying concentrations of dissolved algal organic matter prepared by repeated freeze/thaw cycles of *Nannochloropsis* cells (Reed Mariculture Inc., CA, USA) in liquid nitrogen, liberating a highly concentrated dissolved OM solution which was filtered using a 0.7- μm glass fiber filter in the same fashion as Barber et al., 2014. While dissolved OM derived from fresh plankton cells might differ from pore water dissolved OM where precipitation of natural OC:Fe takes place, it was used only in this proof-of-concept experiment to show the effect of OM complexation to the XANES Fe spectrum (see below). The quantity of dissolved OM was adjusted in order to have initial OC:Fe molar ratios in solution of 1, 3 and 10. The precipitation reaction was performed by oxidizing ferrous chloride in the dissolved algal OM solution, maintaining a circumneutral pH through dropwise addition of 1 M NaOH, in the same fashion as for the precipitation of lepidocrocite. These synthetic solid phases were transferred to Kapton tape for the Fe K-edge X-ray analyses. In addition to synthetic lepidocrocite, we also analyzed commercial goethite (Sigma-Aldrich), but the acquired Fe K-edge XANES spectrum for goethite was indistinguishable from that of lepidocrocite, as also reported in a previous study (O'Day et al., 2004).

5.3.3. Fe Mass Balance

The Fe present in each sample was apportioned into three different components: first, the reducible (henceforth called “reactive”) iron oxide fraction was determined using the dithionite-citrate-bicarbonate extraction method of Lalonde et al. 2012. The Fe concentration in the extract was measured by ICP-MS following acidification to pH<2 with 16N HNO₃. The reactive iron-free residue was then digested by gentle heating with the addition HCl (12N), HNO₃ (16N) and HF (28N). Following evaporation to near-dryness, the final residue was dissolved in a 10% HNO₃ solution and its iron content was analyzed by ICP-MS. Finally, the XANES spectra acquired for the natural (non-extracted) sediments and their reactive iron-extracted counterpart further allowed quantifying, within the reactive iron fraction, the proportions of OC-free iron oxides and iron oxides associated to OM using a linear combinatorial approach (see below).

5.3.4. Iron X-ray Absorption Near Edge Structure Spectroscopy

XANES and NEXAFS (Near Edge X-ray Absorption Fine Structure) spectroscopy target the same region of the X-ray absorption spectra but the two terms are used separately in this text to distinguish between the results for the hard and soft X-ray experiments, respectively. Iron K-edge XANES spectra were collected at beamline X26A at the National Synchrotron Light Source (BNL, NY, USA) using an Si(111) monochromator. To minimize beam damage, the beam was slightly de-focused, giving a spot size of 50 μm^2 . Each end-member used for spectral deconvolution was the averaged XANES spectra from at least 3 different locations on the sample. Two or three replicate X-ray spectra for the raw sediment samples were collected and averaged prior to spectral deconvolution. The beamline energy was calibrated by repeated measurements of an iron foil with a known K-edge absorption band at 7112.0 eV and a nontronite (Fe-rich smectite) standard was run intermittently throughout the runs to account for

any energy drift during the data acquisition. The XANES spectra were normalized using a polynomial fit in order to compare samples of different thicknesses and Fe content, and finally background corrected using the built-in Rbkg algorithm prior to the linear combination fitting. All Fe K-edge data reduction was performed using the ATHENA software package (Ravel B., 2005).

5.3.5. Iron K-edge XANES Linear Combination Fitting

Raw sediment Fe spectra were fit using a linear combination of iron XANES spectra from selected iron reference compounds and treated sediments. The fitting was performed from 20 eV below E_0 to 35 eV above E_0 , without forcing the sum of each component to be equal to 1. The sum of all fitting components for each sample can be found in Table 5-1. Each raw sediment spectrum was fitted in a combinatorial fashion using the XANES spectra for the following three end-members: goethite/lepidocrocite, ferric oxalate and the reactive iron extracted sediment residue. The best fits were selected to match the experimentally determined proportion of Fe remaining after the Dithionite-Citrate-Bicarbonate (DCB) treatment with the spectral deconvolution results (Fig. 5-1). In all cases, the selected fit had a Fe percent contribution for the residual sediment within error from the actual measured Fe content. A similar approach using *a priori* knowledge of a sample to simplify complex systems has been exploited before (Lengke et al., 2007; Revesz et al., 2015), although not by using a post extraction residue as one of the end-members. The 1σ errors for each fitting component can be found in Table 5-1 and represent the error associated to using model compounds in order to deconvolute the XANES spectra of natural samples from complex biogeochemical cycle such as the sediment iron cycle.

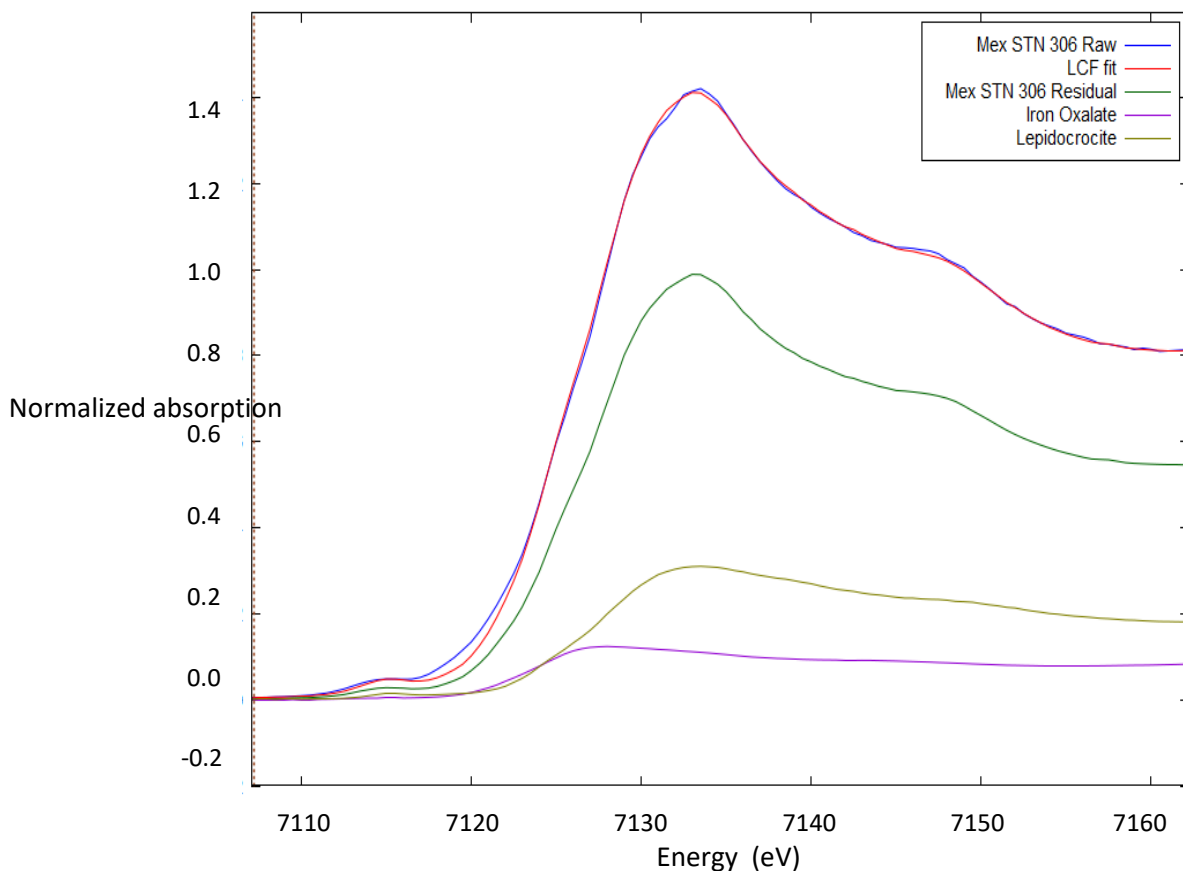


Figure 5-1. Iron K-edge XANES Linear Combination Fitting of the raw sediment Fe spectra for the Mexican 306 sediment using three end-members: goethite/lepidocrocite, ferric oxalate and the reactive iron extracted sediment residue. The best fit (red trace) is almost superimposed on the spectra for the raw, untreated sediment (blue trace).

5.3.6. STXM Sample Preparation and Mapping

Freeze-dried, homogenized sediment samples were embedded in an elemental sulfur resin in place of the typical epoxy resin workup, to minimize sample oxidation. A 1:5 ratio of sediment to sulfur was heated to ~ 140 °C, and allowed to cool/solidify. The solidified sediment sulfur mixture was then sliced using an ultra-microtome to a thickness of 80 to 120 nm and plated on a Transmission Electron Microscopy (TEM) grid for analysis at the beamline.

Initial X-ray “Scan Maps” were collected over a larger portion of the sample at 280 and 288.6 eV as well as 700 and 710 eV for C and Fe determination, respectively. After normalization to the intensity at the empty areas of the measured sample region, the pre-edge images collected at 280 eV and 700 eV were subtracted from the images collected at 288.6 and 710.0 eV (Fig. 5-2), which correspond to absorption bands for carbonyl and the dominant Fe L₃ edge peak for ferric minerals, respectively. These species are ubiquitous in marine sediments and were thus used as indicators for the presence or absence of OC and Fe in these samples. From these images we selected regions where OC was found co-localized to Fe (found in all samples) and regions where OC was not found to be co-localized to Fe (when possible) in order to compare Fe-associated and Fe-free organic functionalities.

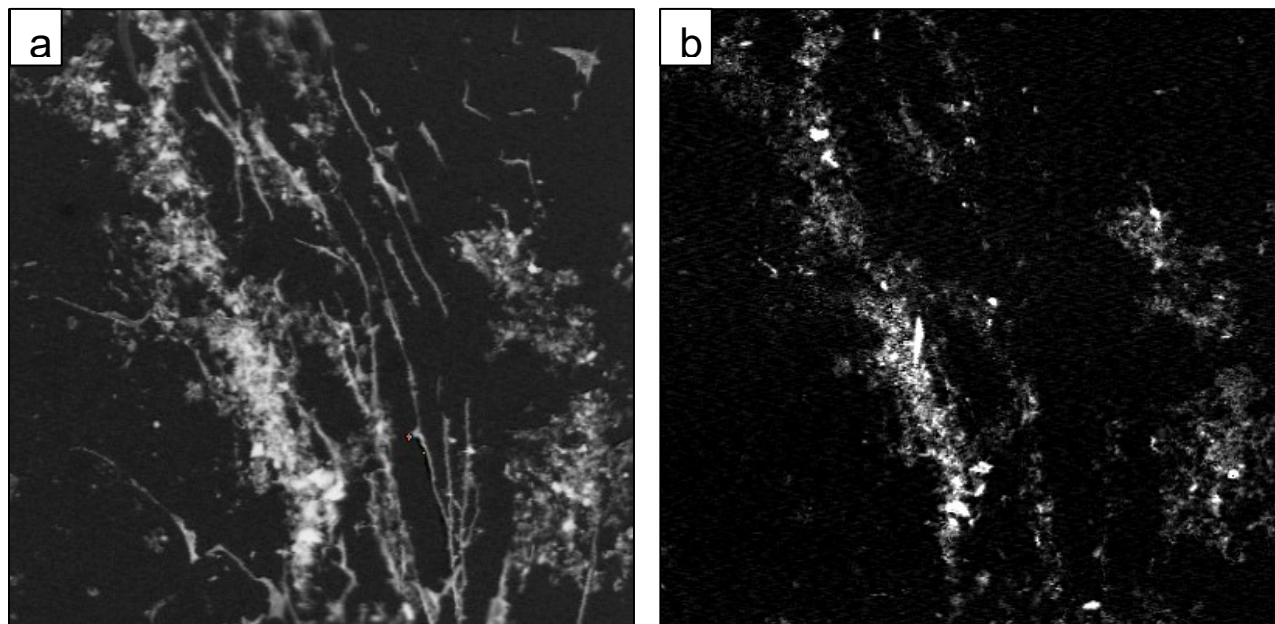


Figure 5-2. STXM “Scan Maps” collected between (a) 280 and 288.6 eV for carbon, and (b) between 700 and 710 eV for iron, respectively. These maps allowed selecting areas where OC and Fe were co-localized in our samples for NEXAFS collection.

5.3.7. Near Edge X-ray Absorption Fine Structure Spectroscopy

C and Fe NEXAFS image stacks were collected from 280-320 eV and 700-735 eV. Despite the nano-scale thickness of the samples, several regions showing co-localization of OC to Fe were characterized by a dip centered around 284 eV in the spectrum and a secondary, less pronounced dip around 290 eV. These dips likely are caused by a loss in signal intensity arising from contaminant organic matter present on the mirrors and lenses of the beamline, absorbing a portion of the incoming beam flux. High OC content samples did not show this feature. The presence of these dips was minimized using ultra-thin sliced samples (80-120 nm). Note that for the Madeira Abyssal Plain turbidite sample, the absolute amount of C was too low to allow acquiring useful NEXAFS spectra.

NEXAFS image stacks were collected every 40-60 nm over the regions of interest. The image stacks were aligned along the X and Y axis, using each preceding image and the “Stack Analyze” software from (Jacobsen et al., 2000). The X-ray image stacks were simplified using the PCA GUI software (Lerotic et al., 2004; Lerotic et al., 2005) in order to cluster the data into regions with similar spectral properties. This was done first by normalizing to the background (I_0) X-ray spectrum from the previously aligned stacks of spectra, then running a cluster analysis following the procedure of Lerotic et al. 2005.

5.3.8. Redox Calculations

A rough assessment of the burial of reducing power stemming from the protection of OM through OC:Fe interactions was calculated from our dataset, using the following redox data. First, the average oxidation state of marine OC was calculated to be -0.48 based on the average elemental composition of fresh planktonic OM ($C_{106}H_{177}O_{37}N_{17}S_{0.4}$), as determined by Nuclear

Magnetic Resonance (Hedges et al., 2002). Since this marine OC is oxidized to CO₂ (oxidation state of +4) when the organic matter is completely remineralized under oxic conditions, the complete oxidation of one mole of OC involves the transfer of 4.48 electrons to electron acceptor species such as dissolved O₂. Note that the reduction of ferric iron to ferrous iron is mediated through the transfer of only one electron.

5.4. Results and Discussion

5.4.1. XANES Analyses

Iron K-edge XANES spectra were collected for the pure iron materials (lepidocrocite and ferric oxalate) and the three synthetic Fe-OC complexes, precipitated from solutions with initial OC:Fe ratios of 1, 3 and 10, respectively (Fig. 5-3A). A key feature of these Fe spectra is the ~4 eV difference between the absorption maxima for pure iron oxides and ferric oxalate, an inner-sphere (Fe-O-C) complex whose coordination environment is dominated by σ and π covalent interactions (Hocking et al., 2010). The lower-energy feature was also observed for synthetic Fe-OC co-precipitates, with its relative intensity increasing when iron oxides were formed in the presence of more dissolved OC (Fig. 5-3A). This systematic increase in intensity of the low-energy Fe-OC feature allowed determining the proportion of iron complexed to OC through inner-sphere interactions using spectral deconvolution and linear combination fitting.

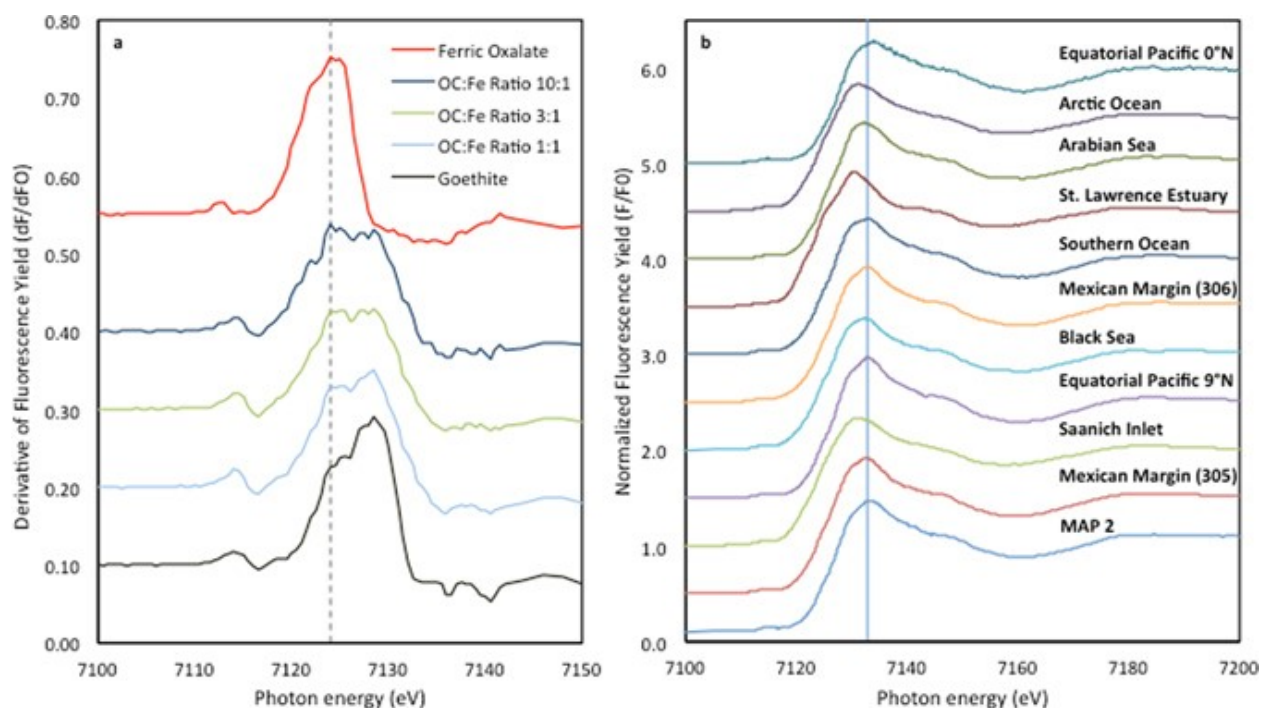


Figure 5-3. Iron K-edge spectra for the samples analyzed in this study. (a) First derivative of Fe 1s XANES spectra for goethite, ferric oxalate and synthetic lepidocrocite with initial solution OC:Fe Molar ratios of 1, 3, and 10. The intersecting line at 7124.5 eV highlights the shift in absorbance maxima for ferric oxalate; (b) Normalized Fe 1s XANES spectra for raw sediments with the vertical line at 7132.8 eV representing the absorption maximum for goethite/lepidocrocite.

Iron K-edge XANES spectra were then collected for a series of sediments and for their residues following extraction of reactive iron oxides (Fig. 5-3B). These spectra were fitted using three end-members: (1) OC-free reactive iron oxides, (in-house synthesized lepidocrocite and commercial goethite from Sigma Aldrich); (2) inner-sphere OC-substituted Fe(III) (ferric oxalate); and (3) residual unreactive iron, corresponding to post reduction sediment residue from each individual sample, as several less reactive iron species not targeted by the reactive iron removal procedure, such as iron-containing silicates or iron sulfides, may be present in varying proportions in the residue. Such differences in composition and relative abundances of non-

reactive Fe-bearing minerals would make the selection of an adequate synthetic end-member for non-reactive iron extremely challenging (Cismasu et al., 2015).

5.4.2. Iron data by XANES

Linear combinatorial fitting calculations revealed that the bulk of the sedimentary iron (56.9 to 90.4 %) is found in the residual non-reactive fraction, with the exception of the extensively oxidized MAP2 turbidite ($11.7 \pm 1.6\%$) (Fig. 5-4, Table 5-1). Total reactive iron, which is the sum of the relative contributions from OC-free iron oxides (Table 5-1 Column 6) and OC-complexed iron (Table 5-1, Column 7) to total Fe, accounts for 8.1 to 43.1% of total Fe, with variable proportions of OC-free iron oxides and OC-complexed iron. The MAP2 sample again is an outlier with 81.1 wt% of total iron found in the reactive iron pool. The relative contribution of OC-complexed Fe accounts for 0 to 18.1 wt% to total iron in the sample. The selected linear combination fitting results for the Equatorial Pacific and Arctic sediments did not include the OC-complexed Fe component, a sharp contrast to Black Sea where this component accounts for 100% of reactive Fe. Interestingly, the highest relative contribution of OC-bound Fe to total reactive Fe is found in the only sulfidic sediment (Black Sea). Although more work is needed to confirm this hypothesis, this result could be due to the fact that reactive iron oxides are not expected to survive in sulfidic environments unless stabilized by organic matter or other surface reactive compounds (Haese et al., 1997; Zee et al., 2003).

Conversely, the non-detectable contribution of the Fe-OC fraction in the Equatorial Pacific and Arctic samples can be explained by their very low OC content (~ 0.30 wt%) (Table 5-1) and high Fe content, respectively (Table 5-1). The OC-bound Fe contribution to total reactive iron in the coastal samples (Saanich, Arabian Sea, Mexican Margin and St. Lawrence Estuary) varies between 25.7 and 62.6 %, supporting earlier results that highlighted the role of iron in the

preservation of organic matter in coastal sediments (Lalonde et al., 2012), where the bulk of the sedimentary OC pool is sequestered globally (Hedges and Keil 1995). The high proportion of reactive Fe covalently bound to OC likely reflects the fact that these interactions take place both at the surface and within iron oxide particles or aggregates.

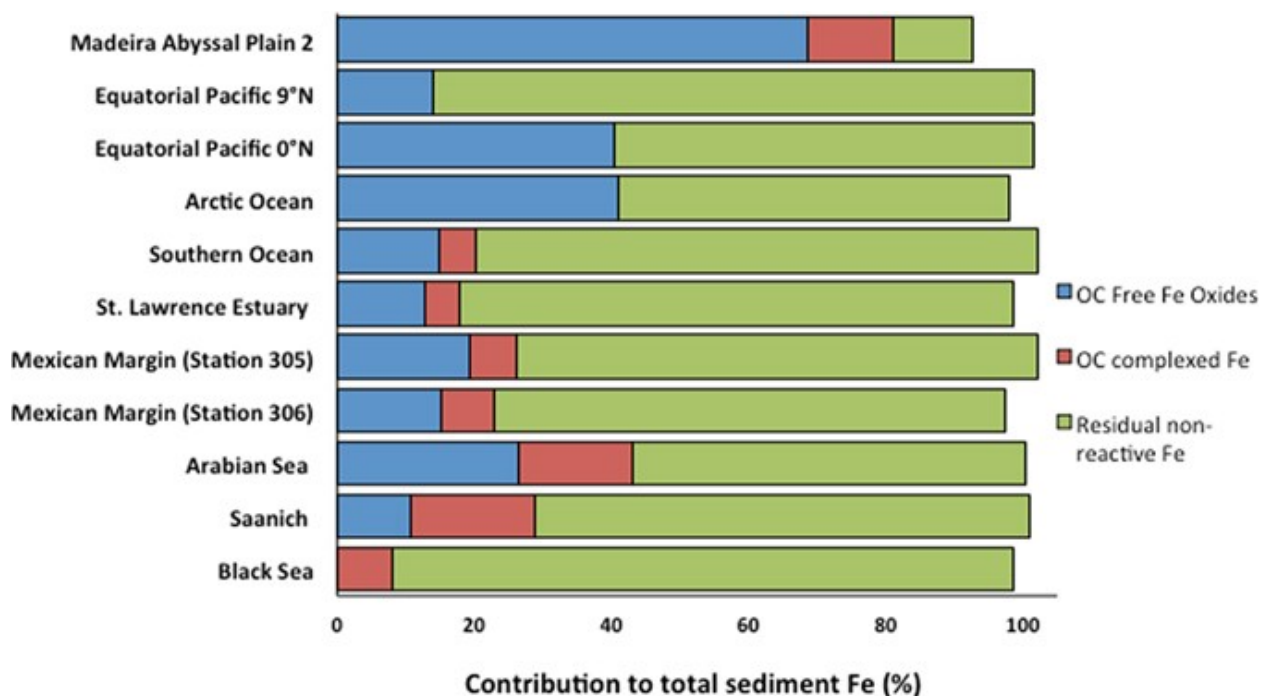


Figure 5-4. Iron K-edge XANES linear combination fitting results showing the OC-free iron oxides (blue), OC-complexed reactive iron (brown), and residual sediment iron (green) contributions to the total sediment Fe pool.

5.4.3. Co-localization of OC and Fe by STXM

Using Scanning Transmission X-ray Microscopy (STXM; Canadian Light Source beamline 10ID-1), a subset of the samples were analyzed to assess OC co-localization with iron, and to determine whether specific OC functionalities are preferentially co-localized with Fe oxides in sediments. Carbon K-edge and Fe L₃-edge X-ray absorption spectra (XAS) coupled to x-ray microscopy images of the sulfur-embedded samples were collected at a 40-nm resolution (Fig. 5-5A). X-ray absorption image stacks were then acquired in OC- and Fe-rich regions allowing

identification of the OC functionalities and determination of the oxidation state of Fe (Fig. 5-5B and E). The XAS for most OC co-localized with Fe is dominated by peaks around 285.3 eV (aromatic, alkene C=C) and 288.5-288.6 eV (carboxyl/carbonyl) in these sediments (Brandes et al., 2004; Solomon et al., 2012a) (mapped areas similar spectral properties, or clusters, in Fig. 5-5F, G and H with corresponding traces in Fig. 5-5E). Another peak of interest at 289.5 eV suggests the presence of alcohols (C-OH; (Solomon et al., 2012a)) co-occurring in most cases alongside aromatic and carbonyl functional groups. Overall, the absorption bands observed for these sediments are similar to those observed for complex soils and synthetic co-precipitates, with the notable absence of peaks at 286.6 eV commonly attributed to ketone (Lehmann et al., 2009; Solomon et al., 2012a; Lv et al., 2016). Note that absorption bands in the post-edge region found at ~297 and 300 eV correspond to the potassium L-edge X-ray absorption bands (Lee et al., 2009), but are not discussed further in this text.

The Fe L₃-edge spectra provide information on the oxidation state of iron based on the relative intensities of two absorption bands (708 and 710 eV) representing the dominant absorption bands for ferrous and ferric iron respectively (Solomon et al., 2012a). The majority of sediment OC was found co-localized to areas dominated by Fe (III) phases (Fig. 5-5B; in this figure, both traces show predominant Fe(III) phases, with a lower intensity peak corresponding to Fe(II)). Across all analyzed sediments, ranging from highly oxidized to fully anoxic environments, the co-localized OC functionalities correspond to chemical groups (carbonyls, alcohols, alkenes and aromatics) that have a high affinity iron oxides (Gu et al., 1995), and are similar to those reported for OC-rich soils (Lehmann et al., 2005; Solomon et al., 2012a). Although co-localization does not necessarily reflect direct inner-sphere complexation, the Fe K-edge deconvolution data presented in this study, as well as several publications (reviewed in (Keil and

Mayer 2013)) provide strong evidence for direct inner-sphere complexation between organic matter and iron in marine sediments. The presence of these ubiquitous functionalities raises interesting questions regarding the factors that promote the complexation of OC with reactive iron oxides. One of the most important is the affinity of carbonyl- and hydroxyl-containing aromatic acids, which bind to iron (oxy)hydroxides via a ligand exchange mechanism (Gu et al., 1995), with organic matter displacing the hydroxyl surfaces from the reactive iron species. The mixed σ and π bond characteristic of these organic compounds readily allows for the formation of a highly stable OC:Fe complexes, similar to the interactions of iron with siderophores.

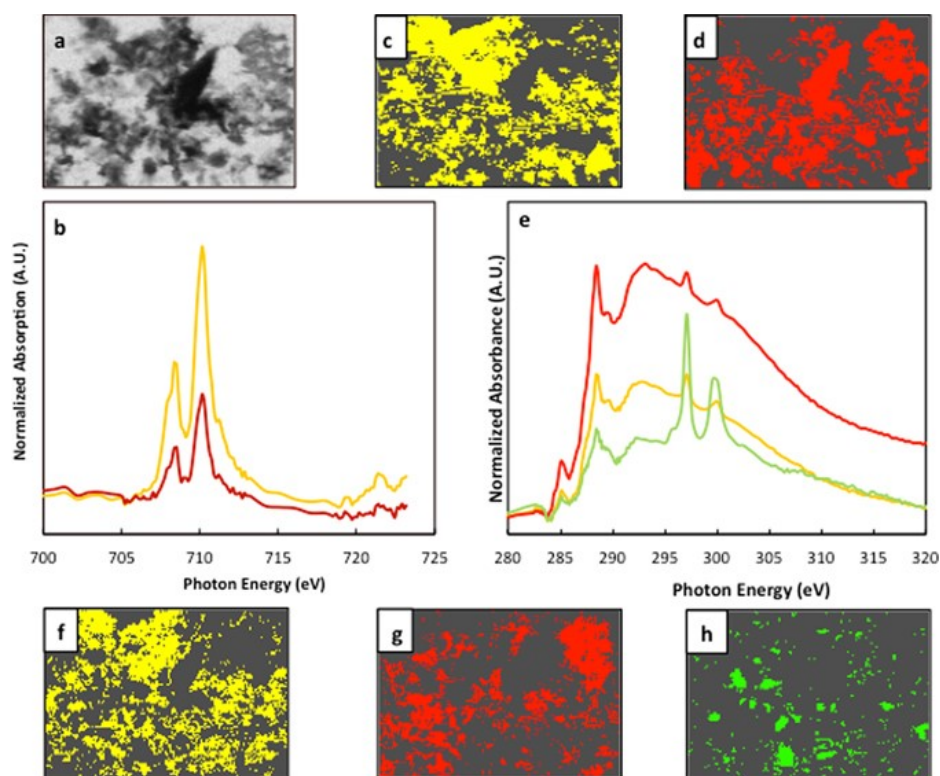


Figure 5-5. Chemical composition of co-localized iron (panels a and b-d) and organic matter (panels A and E-H). (a) Representative 12 x 8 μm X-ray microscopy image from the Mexican Margin sediment (Station 306); (b) Iron L3 edge XAS spectra for the Fe cluster maps in panels (c) and (d); (e) Carbon K-edge XAS spectra for the (c) cluster maps in panels (f), (g) and (h). Note that colored traces in panels (b) and (e) correspond to the different coloured carbon clusters in panels (c-d), and (f-h), respectively. Each cluster was identified using the PCA and clustering analysis described in the methods section.

5.5. Implications

Our findings have important implications with respect to the global Fe and OC cycles, with ramifications that extend to the marine sediment organic carbon sink and global climate change. First, while the nano-scale co-localization of sediment OC and Fe has been reported before, we show for the first time the importance of direct inner-sphere complexation involving aromatic, carbonyl and alcohol groups in unaltered natural samples (Fig. 5-5). We also provide the first direct assessment of the percentage of reactive Fe involved in strong Fe-O-C bonds, and find that between 25.7 and 62.6% of reactive iron is directly bound to OC in coastal settings, emphasizing the importance of Fe-OC interactions not only for the OC cycle but also for the Fe cycle.

The fact that only a fraction of reactive iron is covalently bound to OC suggests that using OC:Fe ratios to infer binding mechanism (Wagai and Mayer, 2007; Raiswell and Canfield, 2012; Lalonde et al., 2012) should be avoided, as a quantitatively important fraction of reactive iron is not complexed to OC through inner-sphere interactions. For the coastal and deep-sea sediments studied here (excluding the Black Sea and Saanich Inlet sediments accumulating under anoxic conditions; see below), a strong linear trend was observed between the moles of OC associated to iron oxides per gram of sediment, measured following wet chemical extraction (from Lalonde et al., 2012), and the moles of reactive iron complexed to OC per gram of sediment, measured by XANES (this work; Fig. 5-6). The slope of ~ 5 observed in Fig. 5-6 represents the molar ratio of Fe-complexed OC to OC-complexed Fe (OC:Fe molar ratio). OC:Fe ratios have previously been used to infer bonding mechanisms between OC and Fe with OC:Fe ratios of ~ 1 indicating simple mono-layer sorption, while higher OC:Fe ratios being indicative of coprecipitation (Wagai and Mayer, 2007). When determined using chemical extractions, the amount of OC-complexed Fe is overestimated as all reactive iron is extracted (OC-free iron oxides and OC-complexed iron). By

providing an estimate of the fraction of reactive iron that is complexed to OC, the linear combination fitting results allow to correct for this bias. The slope of ~ 5 from Fig. 5-6 thus represents a more accurate estimate of the OC-to-Fe molar ratio characteristic of these inner-sphere complexes and agrees with the existence of agglomerates containing iron that is interweaved between layers of organic molecules, analogous to the onion model of Mackey and Zirino (Mackey and Zirino, 1994), as opposed to the monolayer sorption hypothesis in which OC:Fe ratios of ~ 1 are expected.

The two sediments accumulating under anoxic conditions gave OC:Fe ratios of about 30, a value that suggests the existence of other OC stabilization mechanism(s) in which Fe is involved. Alternatively, such high ratios might also reflect the fact that large organic biomolecules may be only partly associated to iron oxides through only one or a few functional groups, a hypothesis that is more plausible under anoxic conditions (see below). The organic functionalities observed from the C K_{1s} X-ray absorption experiments could be indicative of large aromatic acids complexing Fe(III) via a ligand exchange mechanism. In such complexes only a fraction of the carbon atoms would be directly bound to Fe but would still allow for the OC:Fe molar ratios observed in the reducing environments studied here. Notably, these sediments also have much higher OC surface loadings (mg OC per square meter of surface area) compared to normal coastal sediments (Keil and Cowie, 1999). More work is needed to explain these high OC:Fe ratios.

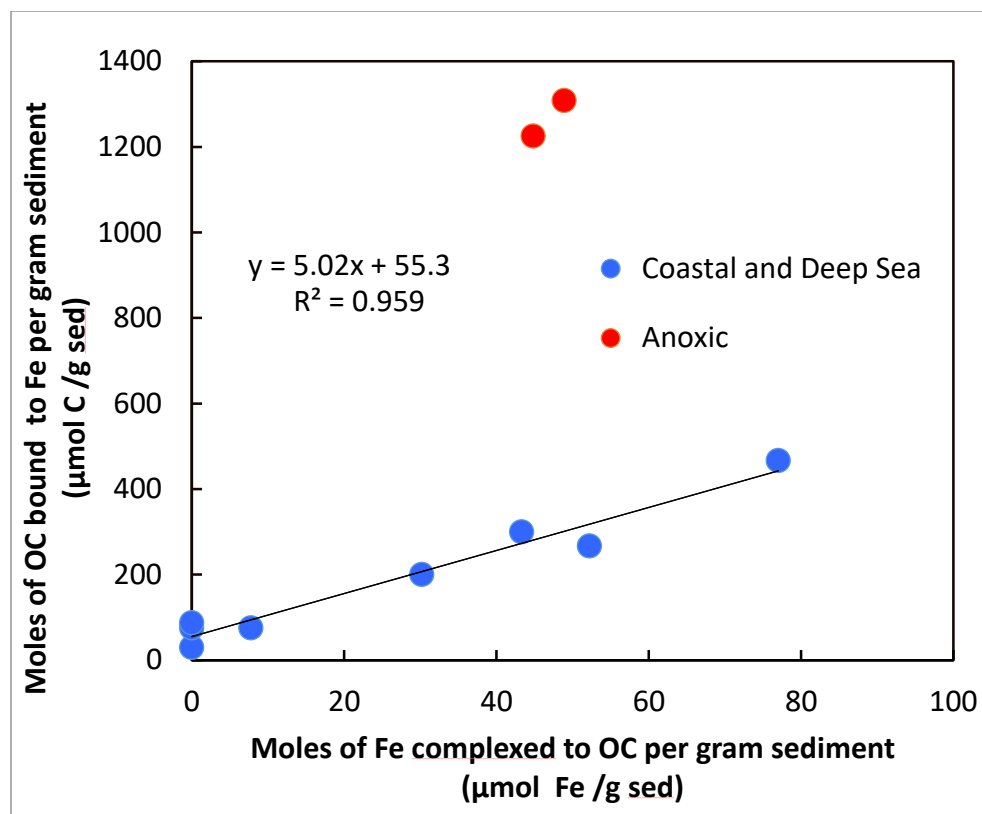


Figure 5-6. Correlation between the quantity of OC associated to iron oxides measured by wet chemical extraction (Lalonde et al., 2012), and the quantity of Fe found complexed to OC measured by XANES (this work) for the samples studied in this work. Sediments accumulating under anoxic conditions are excluded from the regression (see text for explanations).

Second, XANES analysis and spectral deconvolution show that the proportion of reactive Fe complexed to OC increases with decreasing oxygen exposure. The fraction of OC-complexed Fe negligible in low OC, highly oxidized deep-sea sediments and accounts for 100% of the reactive iron pool in sulfidic black sea sediments. The same relative enrichment in OC-complexed Fe was found in Fe-bearing minerals in soils exposed to prolonged regular alternation of redox conditions (Vogelsang et al., 2016). The irreversible nature of binding is particularly important for OC preservation in anoxic sediments where biological degradation first proceeds through solubilisation followed by enzymatic hydrolysis (Keil et al., 1994). Anoxic respiration is less

efficient and pervasive than oxic degradation in which reactive oxygen species lead to extensive and non-specific OC oxidation (Hartnett et al., 1998). In such oxic environments, only physically shielded, inaccessible OC is efficiently preserved on a long-term basis (Ransom et al., 1998), partly explaining the very low OC concentrations and accumulation rates measured in pelagic settings.

Physical shielding of OC by iron oxides is best achieved in redox transition zones within sediments where dissolved Fe(II), a product of the reduction of iron oxides in the deep, anoxic sediment layers, diffuses upwards towards the oxic-to-anoxic sediment transition layer. Upon coming into contact with dissolved O₂, which diffuses downward into the sediment from the water column, Fe(II) is oxidized and precipitates as Fe(III) oxides in the presence of dissolved or colloidal porewater OC, forming mixed mineral-organic co-precipitates aggregating on the surface of other mineral particles (Riedel et al., 2013). The degradation rate of OC complexed to Fe within these aggregates is much slower than those of dissolved or reversibly sorbed OC (Arnarson and Keil 2007).

Co-precipitation of Fe-OC aggregates also influences the fate of iron oxides in sediments. Free iron oxides are not thermodynamically stable under anoxic conditions and are thus reduced to soluble Fe(II). Complexation with OC physically protects iron oxides, sterically inhibiting their enzymatic and reductive dissolution, likely explaining the persistence of metastable reactive Fe(III) on very long time scales in reduced sediments (as long as 400 kyrs (Haese et al., 1997)). Although more work is needed to confirm this hypothesis, our interpretation agrees with the lack of organic-free iron oxides as a significant contributor to total Fe in the Black Sea sediment. This mechanism is analogous to a synergistic transport mechanism, or synergistic ferric OC shuttle,

which, in conjunction with other OC preservation pathways, protects OC during its critical passage through the sediment oxic layers and facilitates its transfer to the deeper, anoxic layers.

Notably, the formation of OC-Fe aggregates results in a net gain for the global redox balance at the surface of the Earth as the reduction of one mole of iron consumes one mole of electrons, while the oxidation of one mole of reduced OC liberates on average about 4.48 moles of electrons (Hedges et al., 2002). Using a conservative estimate for the total amount of OC sequestered in marine sediments via direct bonding to iron oxides as 19×10^{15} g of C (Lalonde et al., 2012), this mass of reduced C amounts to the burial of 7.1×10^{15} moles of electrons. This value is corrected by also considering the burial of OC-complexed oxidized iron, which would otherwise be reduced via the transfer of one electron per mole of Fe(III). Using the average corrected OC:Fe molar ratio of 5.02 obtained from the slope of Fig. 5-6, we find that the stabilized Fe that escapes reduction amounts to 3.2×10^{14} electrons, giving a total corrected transfer of 6.8×10^{15} electrons via this synergistic ferric organic carbon shuttle. Such back-of-the-envelope calculation is an oversimplification of a very complex system but it provides a rough estimate of the importance of this mechanism in the transfer of reducing power from the surface of the Earth to the slowly cycling sedimentary rock carbon pool, contributing to the stability of the global redox balance and the Earth's oxygenated atmosphere.

The strong inner-sphere complexes formed between OC and Fe(III) in marine sediments play a critical role in the sequestration of organic matter. These interactions are mutually beneficial as they allow for the stabilization and burial of OC, which would otherwise be mineralized back to CO₂ or CH₄, while also stabilizing reactive iron in low oxygen environments (such as the Black Sea). Protection of OC and stabilization of reactive iron within sediments allows for these complexes to escape reductive dissolution, which occurs near the sediment oxic/anoxic redox

boundary. This protection mechanism allows for both reactive and intrinsically stable organic matter to escape degradation over very long timescales.

Chapter 6: Redox Conditions Influence the Chemical Composition of Iron-Associated Organic Matter in Boreal Lake Sediments: a Synchrotron-Based NEXAFS Study

Andrew Barber¹, Jay Brandes², Azadeh Joshani¹, Charles Gobeil³, André Tessier³, Yves Gélinas¹

¹ GEOTOP and Department of Chemistry and Biochemistry, Concordia University, 7141 Sherbrooke West, Montreal, QC, Canada, H4B 1R6

² Skidaway Institute of Oceanography and Department of Marine Sciences, University of Georgia Athens, 10 Ocean Science Circle, Savannah, GA 31411, USA

³ INRS-Eau Terre Environnement, 490 rue de la Couronne, Université du Québec, QC, Canada, G1K 9A9

* Corresponding author:

Yves Gélinas

Department of Chemistry and Biochemistry

Concordia University

7141 Sherbrooke Street West

Montréal, QC, Canada, H4B-1R6

Tel.: 514-848-2424, ext. 3337

Email: yves.gelinas@concordia.ca

6.1. Abstract

The global carbon and iron cycles are intimately linked as redox-sensitive iron oxides readily bind organic matter in a variety of environmental settings, including marine and lacustrine sediments. Although iron-organic matter complexes sequester important quantities of organic carbon, the composition of the organic matter in such complexes remains poorly defined. Here we present C K_{1s} and Fe L_{3,2} edge Near Edge X-ray Absorption Fine Structure (NEXAFS) spectra of surface sediments (0–0.5 cm) material precipitated onto inert Teflon sheets deployed across the sediment-water interface from two adjacent basins of a pristine boreal lake located in Québec, Canada, exposed to contrasting oxygen exposure regimes. One of the basin is perennially oxygenated whereas the other becomes anoxic for a short time period once a year at the end of the high primary production season. In addition to the sediments, NEXAFS spectra were collected for samples of authigenic material precipitated onto inert Teflon sheets deployed across the sediment-water interface for several years in the perennially oxygenated basin. We demonstrate marked differences in organic carbon speciation in sediments from both basins, as well as co-localization of organic carbon and iron at a sub-micron scale in microtomed samples. Reactive organic molecules such as polysaccharides were found preferentially associated to iron in the sediments of the perennially oxic basin compared to more phenol rich organics in the sediments of the seasonally anoxic basin. Traces of aliphatic carbon were observed in sediments from the sporadically anoxic basin, alongside carboxyl and aromatic functionalities. This carboxyl-rich aliphatic material could interact with the sediment mineral matrix either through a ligand exchange mechanism between the mineral phases and the carboxyl functionalities, or via non-specific hydrophobic interactions between the mineral matrix and aliphatic moieties We

conclude that a short period of anoxia in hypolimnetic waters over an annual cycle significantly modified the type of OM associated with Fe oxyhydroxides in lake sediments.

6.2. Introduction

Natural organic matter (OM) is compositionally complex, difficult to characterize and pervasive in all natural settings including soils and sediments from both freshwater and marine environments (Hedges et al., 2000). The different pools of organic carbon (OC) combine with the sizeable inorganic carbon pools to form the major compartments of the global carbon cycle (Hedges and Keil, 1995). Together, they profoundly modulate the environmental conditions at the surface of our planet, as shown by the current CO₂-driven changing climate, or by the fact that the burial of massive amounts of natural reduced organic molecules was necessary for the rise in atmospheric oxygen (Bernier, 1989). As such, the sequestration and long-term preservation of organic matter (OM) has been and remains an area of interest for both fundamental and applied research alike. For example, the study of complex natural OM can be of interest to soil scientist in the context of regulating soil fertility via bio-char amendments but these studies also raise fundamental questions regarding the mechanisms which sequester OC in such environments as well as their impact on the soil OM composition (Eckmeier et al., 2007; Laird, 2008; Riedel et al., 2014)., as well as investigations on the physico-chemical processes that allow for the preservation of a small fraction (< 1%) of OM photosynthesized in the open ocean (Martin et al., 1987). A comprehensive understanding of OM preservation mechanisms and factors that influence the long-term sequestration of OM is vital to constraining the evolution of the Earth's climate. More carbon is sequestered within soils and sediments than is present in the Earth's atmosphere making these environmental compartments of utmost importance to the study of the global carbon cycle (Hedges and Keil, 1995; Falkowski et al., 2000; Tranvik et al., 2009).

In this respect, the oxygen exposure regimes play a critical role on the sequestration of OM via interactions with mineral phases in lacustrine sediments.

Recent work has revealed the importance of lacustrine sediments in the cycling of OC on a global scale (Pace and Prairie, 2005; Cole et al., 2007; Ferland et al., 2012). Only through the inclusion of carbon rich sediments of small (< 1 km²) boreal lakes such as those found along the Canadian Shield, in regional and global carbon compilations did their importance become apparent for OM sequestration (Roehm et al., 2009; Brothers et al., 2012; Ferland et al., 2012). So far however, very little work has been done on the mechanisms that promote OM sequestration in sediments from these small lakes, in particular with respect to the preservative interactions between OM and the sediment mineral phases, which have been shown to be instrumental to the long-term (geologic timescale) preservation of OM in marine settings (Mayer, 1994b; Hedges and Keil, 1995; Ransom et al., 1998).

The high affinity of many organic functionalities towards iron oxyhydroxide (hereafter simply identified as oxide) oxide surfaces has been repeatedly demonstrated in adsorption and co-precipitation experiments involving synthetic iron oxides (Gu et al., 1996a; Gu et al., 1996b), as well through the compositional analysis of the OM liberated upon reductive dissolution of iron oxides (Lalonde et al., 2012; Shields et al., 2016). Notably, for marine sediments, the fact that redox sensitive species such as iron (Lalonde et al., 2012; Barber et al., 2014) and manganese oxides (Estes et al., 2017) readily bind large portions of the sediment OM pool has driven researchers towards characterizing the OM associated to these metal oxide species.

One drawback of many of these studies is the need to chemically or physically separate the OM from the sediment mineral matrix losing in the process any spatially relevant findings.

Characterization of bulk OM and its extracts is commonly performed using a variety of techniques including, but not limited to, nuclear magnetic resonance spectroscopy (e.g. Preston, 1996; Chen et al., 2002; Dickens et al., 2006; Cao et al., 2016), Fourier transform infrared spectroscopy (e.g. Gu et al., 1995; Celi et al., 1997; Chen et al., 2002; Hatcher et al., 2014), and mass spectrometry (e.g. Colombo et al., 1996a; Colombo et al., 1996b; Caupos et al., 2015).

Even other, relatively novel methods such as electrospray ionization Fourier transform ion cyclotron resonance mass spectrometry (ESI-FT-ICR-MS; Riedel et al., 2014) do not allow for the characterization of intact sediment material, preventing the acquisition of spatially resolved data relating to the interactions between the sediment mineral matrix and OM.

Recent instrumental and analytical advances coupled with the widespread use of modelling techniques have led to important findings regarding OM diagenesis and sequestration (Burdige et al., 2016; Clayer et al., 2016; Couture et al., 2016). In addition, the advent of spectromicroscopic imaging techniques such as scanning transmission X-ray microscopy (STXM), have allowed for the characterization of OM associated with intact soil (Lehmann et al., 2008; Solomon et al., 2012a) and sediment particles (Chen et al., 2014). STXM allows for mapping and simultaneous collection of X-ray absorption spectra across a given sample. One of the most powerful features of STXM analysis is the ability to collect X-ray absorption spectra for multiple elements of interest in the same sample, namely C and Fe in this study. This allows for identification of micron-size regions of the sediment samples where these elements are co-localized, while also providing information about their speciation/oxidation state. These advances help bridge the gap between bulk chemical extraction experiments and the interactions that occur between OM and

sediment/soil mineral phases at the nanometer scale (Lehmann et al., 2008; Lalonde et al., 2012). High spatial resolution carbon characterization methods such as nanoscale secondary ion mass spectrometry (Vogel et al., 2014) and STXM (Lehmann et al., 2005; Chen et al., 2014; Barber et al., 2017) are also opening new avenues of research into the decades old topic of organo-mineral assemblages in natural environments.

The primary goal of this study is to probe the impact of seasonal variations in oxygen exposure on the composition of sediment OM and specifically the OM sequestered via interactions with redox sensitive components of the sediment mineral matrix, such as iron oxides. Here, we compare the chemical composition of sediment OM from two basins of a pristine boreal lake (Lake Tantaré) with seasonal variations in oxygen exposure regimes. Additionally, we assess the impact of such variations on the co-localization of OC and Fe at a sub-micron scale using STXM, as well as on the chemical composition of OM co-localized with Fe. From the observed chemical functionalities, we infer possible bonding mechanisms that may be responsible for the co-localization and co-extraction of OC and Fe. As OM reaching the sediment water interface interacts strongly with the mineral phases, we also compare the sediment OM composition to that of OM co-precipitated and/or adsorbed on authigenic iron oxides collected at the sediment water interface. Lake Tantaré sediments and these authigenic iron oxides have been extensively studied in terms of trace metal diagenesis (Laforte et al., 2005; Chappaz et al., 2008a; Couture et al., 2008; Chappaz et al., 2008b; Chappaz et al., 2010; Feyte et al., 2010; Tessier et al., 2014), yet little work has focussed on OM speciation, let alone on interactions between OM and the sediment mineral phases in these samples.

6.3. Materials and Methods

6.3.1. Study Site

Lake Tantaré (47°04'N, 71°33'W) is a 1.16 km² oligotrophic boreal lake located about 38 km northwest of Québec City. Comprising 4 basins, each separated by shallow sills, this lake has remained relatively undisturbed by anthropogenic activities including wood harvesting because it is located within the boundaries of an ecological reserve. This study took place in the two westernmost basins (A and B), with Basin A being shallower (15-m water column) and perennially oxygenated, while the deeper Basin B (21-m water column) can undergo short periods of seasonal anoxia in the fall. Iron recycling is observed in the profundal sediments of the perennially oxic Basin A due to the reduction of reactive Fe(III) in the lower sediment strata, upward diffusion of porewater Fe(II), and its oxidation and precipitation as authigenic Fe(III) oxyhydroxides in the top sediment layers and above the sediment-water interface (Fig. 6-1a, b). The sharp positive [Fe] gradient close to the sediment-water interface (Fig. 6-1b) coupled to the large {Fe} excess just below the sediment surface (Fig. 6-1b) reflects the intensity of the Fe recycling in this lake basin. It should be noted that the authigenic Fe oxyhydroxides that are normally deposited to sediment particles close to the sediment-water interface as shown in Fig. 6-1a can also be collected by Teflon sheets inserted vertically in the sediments, as demonstrated by Belzile et al. (1989). In contrast, the features, i.e., sharp [Fe] gradients and significant {Fe} excess observed in basin A are nearly absent in the sediments of the occasionally anoxic Basin B (Fig. 6-1 c,d).

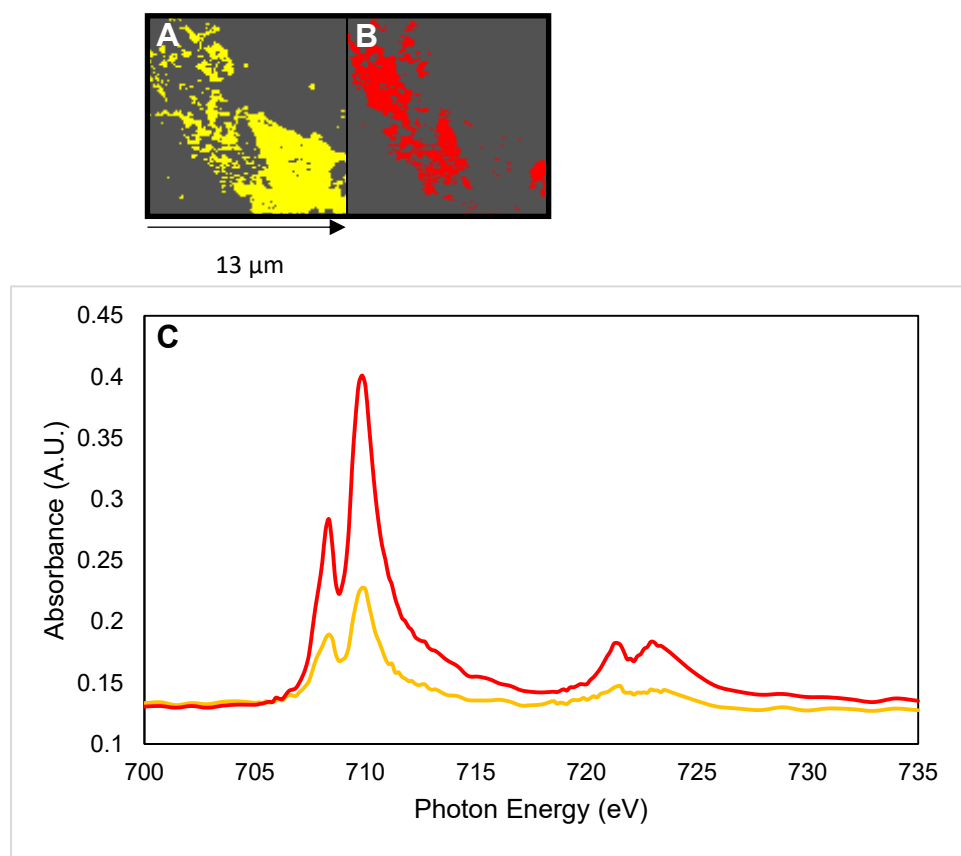


Figure 6-1: (A and B) Fe L_{3,2} edge cluster maps (13 x 13 μm) for sediments from the oxic basin of Lake Tantaré. (C) Fe L_{3,2} NEXAFS spectra corresponding to the individual cluster maps.

6.3.2. Sample Collection and Preparation

Sediment cores were obtained in August 2013 by divers with 9.5-cm internal diameter butyrate tubes at the deepest part of Basins A and B. The cores were sectioned on the shore at 0.5-cm intervals, and here we present data from the top 0-0.5 cm depth interval herein referred to as surface sediment. The sediment samples were kept at 4 °C until their return to the lab, where they were lyophilized and subsequently homogenized using a mortar and pestle. Sheets of skived Teflon (7 cm × 15 cm) inserted by divers across the sediment-water interface at the coring site in Basin A were retrieved after a 13-yr deployment, rinsed with lake water to remove sediment particles and stored in polyethylene containers.

The sediment OC content, determined by elemental analysis (Eurovector 3000), is high ($24.2 \pm 0.5\%$ and $26.8 \pm 0.3\%$ OC (wt/wt) for Basins A and B, respectively). Carbonates were removed from the sediment samples prior to determining the carbon content (but not for STXM analysis) using an acid fumigation chamber (12 N HCl, overnight) followed by gentle heating to evaporate any remaining acid (Hedges and Stern, 1984).

The freeze-dried sediments, as well as the material deposited on the Teflon sheet, which was scraped off using a scalpel, were embedded into elemental sulfur and sliced to a thickness of ~ 100 nm for X-ray analysis at the beamline. Each sediment sample was mixed with powdered elemental sulfur in a 1:5 ratio, heated at 140 °C and fused onto the surface of an elemental sulfur block. This sediment:sulfur mixture solidified upon cooling to room temperature, at which point it was thinly sliced to a thickness of 80, 100 or 120 nm using a Leica Ultracut™ ultra-microtome equipped with a Diatome™ sonic diamond knife. Sample sections were then placed on SiN-support transmission electron microscopy (TEM) grids for STXM analysis.

6.3.3. Sample Mapping and NEXAFS Stack Collection

All STXM analyses were performed at beamline SM 10ID-I at the Canadian Light Source (SK, Canada). Upon arrival at the beamline, each sample was scanned at the carbon K_{1s} and iron $L_{3,2}$ edges. Relatively large portions of the samples (about 200×200 μm) were quickly raster scanned to positively identify the presence of carbon and iron. Spectra were collected for the pre-edge and at a photon energy corresponding to ubiquitous spectral features expected for sediments. Previous studies involving X-ray analysis of soils (Lehmann et al., 2008; Solomon et al., 2009; Solomon et al., 2012a) and marine sediments (Barber et al., 2017) have identified the absorption band at 288.6 eV as a common dominant spectral feature for OC and the band near 710 eV as indicative of ferric iron. The pre-edge features were then subtracted from the images

collected at these photon energies in order to ensure that other components from the sediment were not misinterpreted as either C or Fe.

Sample areas of interest for NEXAFS measurements/analysis were identified based on the co-localization of OC and Fe. Smaller (generally 8 x 8 μm) sections of the sample were then analyzed with higher spatial and energy resolutions to acquire “stacks” of images (Thieme et al., 2010 and references therein). Each image is composed of a series of X-ray absorption data points collected at a given photon energy every 30-40 nm going across the sample. These images can then be sandwiched together in order to provide an X-ray absorption spectra for each individual pixel. For carbon, the images are collected between 280 and 320 eV, with the finest energy resolution of 0.15 eV being used between 282 and 292 eV, where the absorption bands of interest to this study are found. The Fe absorption spectra were collected between 700 and 735 eV, with the finest energy resolution (0.15 eV) targeting important features occurring between 705 to 713 eV and between 718 to 723.5 eV.

The collected stacks were aligned in the X and Y plane using the “Stack Analyze” software, where each image is aligned based on the previous image. After alignment, the background (I_0) spectrum is selected based on regions where no sample was observed. The rest of the spectrum is then normalized to this background. Further data reduction is performed by principal component analysis and a subsequent clustering analysis using the PCA GUI software (Lerotic et al., 2004; Lerotic et al., 2005) allowing for the separation of the bulk images into regions with similar spectral features, including the presence or absence of specific absorption bands, as well as regions of differing OC and Fe content. Additionally, the photon energy was calibrated daily with gaseous CO_2 based on the dominant 3p Rydberg peak for CO_2 to 294.96 eV (Benzerara et al., 2004).

6.4. Results

6.4.1. Fe L_{3,2} edge NEXAFS Spectroscopy

Sediments from both basins as well as the authigenic iron oxides precipitated on the surface of the Teflon sheets were analyzed at the Fe L_{3,2} edge. In all cases the spectra were marked by the presence of two absorption bands centered near 708.4 eV and 709.9 eV. The relative proportion of these two peaks varied between the two basins, with the strongest absorbance band observed at 709.9 eV for the oxic Basin A (Fig. 6-1) and 708.4 eV for the anoxic Basin B (Fig. 6-2). The dominant absorption band in this region can be used as an indicator of the oxidation state of iron, with the peaks at 709.9 and 708.0 eV being indicative of Fe(III) and Fe(II), respectively.

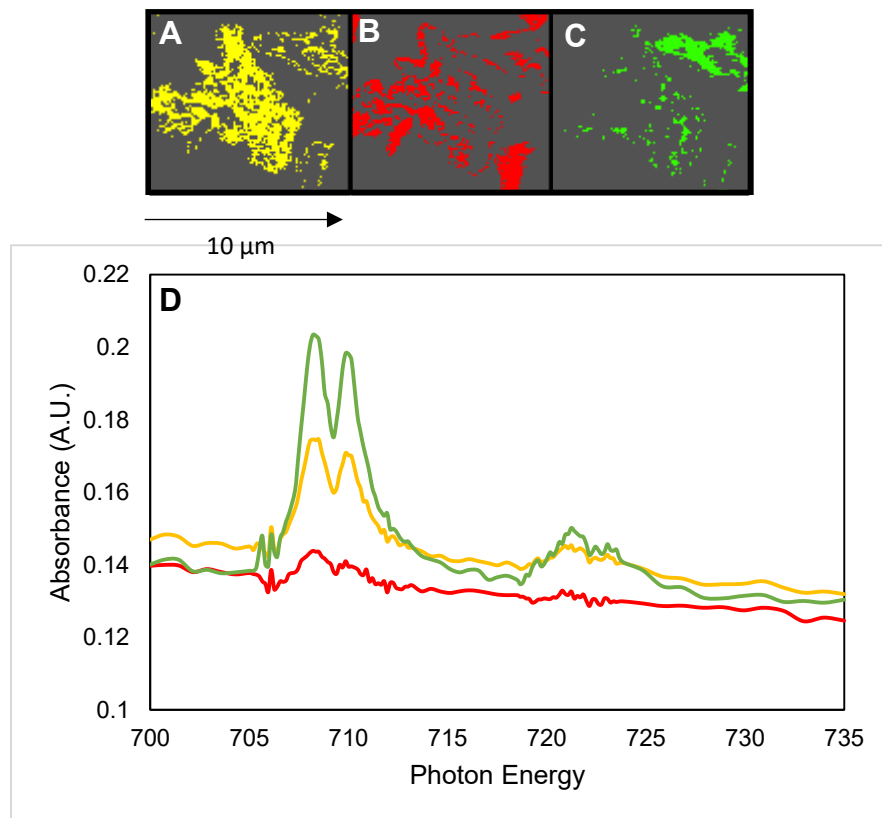


Figure 6-2: (A, B and C) Fe L_{3,2} edge cluster maps (10 x 10 μm) for sediments from the anoxic basin of Lake Tantaré. (D) Fe L_{3,2} NEXAFS spectra corresponding to the individual cluster maps.

6.4.2. C K_{1s} NEXAFS Spectroscopy

The C NEXAFS images were collected between 280 and 320 eV, with the important features corresponding to OC functionalities absorbing between ~284 and 290 eV. For sediments from the perennially oxic Basin A, three distinct absorption bands were observed at 285.1 eV, 288.6 eV and 289.5 eV (Fig. 6-3), corresponding to aromatic C=C, carbonyl C=O and alkyl C-OH functionalities, respectively (Lehmann et al., 2009). Near the dominant absorption band found at 288.6 eV in most traces, a secondary downshifted absorption band was observed near 288.0 eV (most evident on trace H, Fig. 6-3). This value is at the lower range of expected absorption band energies for carbonyl functionalities (Solomon et al., 2012a), although the shift to lower energies suggests differences in the vicinal functional groups. Additionally, an unresolved shoulder was observed at 286.6 eV for several of the regions where C was co-localized to Fe (Fig. 6-3). Absorption bands within this region have previously been attributed to the presence of either ketonic compounds, or OH-substituted aromatic compounds (Lehmann et al., 2008; Solomon et al., 2012a).

Several C K_{1s} NEXAFS spectral features were common to sediment OM from both basins. These include the clearly resolved peaks centered near 285.1 eV likely representing aromatic C=C functionalities as well as at 288.6 eV representing carbonyl C=O carbon (Fig. 6-3 and 6-4). Unlike in the oxic basin, the absorption band near 286.6 was fully resolved in most sample locations/clusters of the anoxic basin (Fig. 6-4). Additionally, a novel peak shoulder was visible at 287.4 eV in clusters D and F from the anoxic basin (Fig. 6-4), which can be attributed to aliphatic C-H functionalities. Another distinction between the two basins is the presence of a strong absorbance band at 290.2 eV in all clusters observed for the anoxic basin which we

attribute to carbonates present within the sediment mineral matrix (Benzerara et al., 2004).

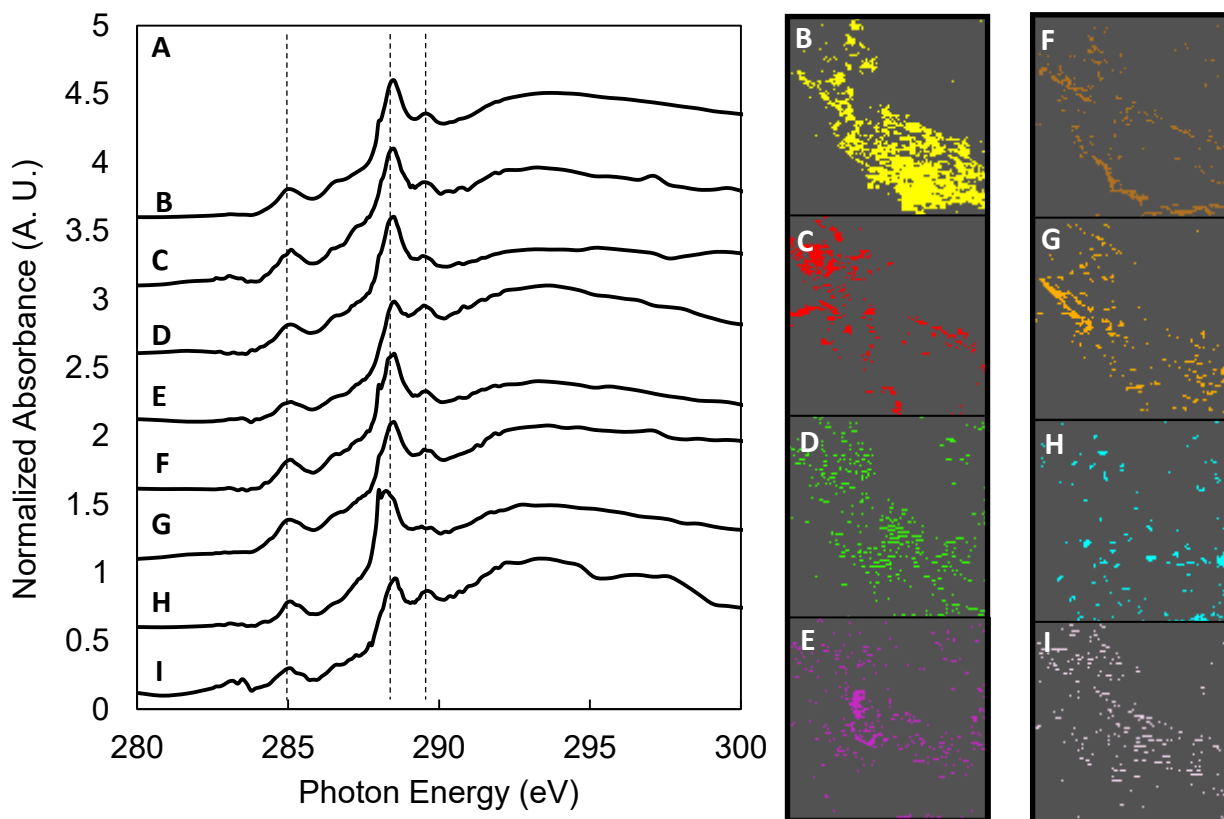


Figure 6-3: (A) C K_{1s} edge NEXAFS spectra for the oxic surface sediments. Each spectra corresponds to the similarly labelled cluster maps (B-I). The dashed vertical lines are located at photon energies of interest (285.1 eV, 288.6 eV and 289.5 eV).

C NEXAFS were also collected for the authigenic iron oxides adsorbed on the Teflon plate inserted in the oxic basin of Lake Tantaré. Similar NEXAFS spectra were obtained for the OM associated with these authigenic iron species, with X-ray absorption bands centered at 285.1 eV, 288.6 eV and 289.5 eV (Fig. 6-5). Unlike in the oxic surface sediments, the peak at 286.6 eV was sometimes found as a distinct absorption band (Trace C, Fig. 6-5). Alongside the differences in observed functional groups, the relative quantity of specific functional groups varied across the different observed clusters, as best observed by comparing traces B and C in Fig. 6-5.

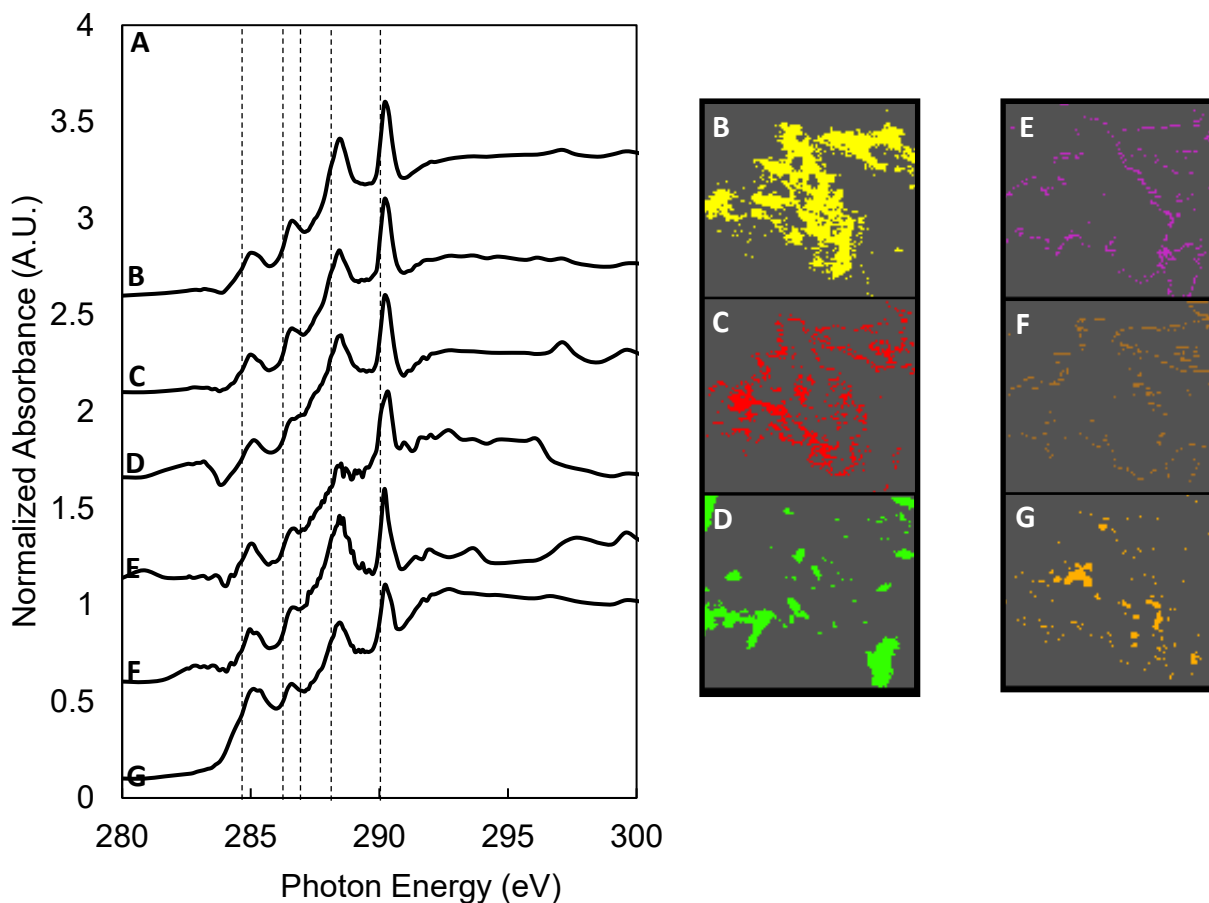


Figure 6-4: (A) C K_{1s} edge NEXAFS spectra for the anoxic surface sediments. Each spectra corresponds to the similarly labelled cluster maps (B-G). The dashed vertical lines are located at photon energies of interest (285.1 eV, 286.6 eV, 287.4 eV, 288.6 eV and 290. 2 eV).

6.5. Discussion:

6.5.1. Co-localization of OC and Fe

Previous work on Lake Tantaré sediments using dithionite as a chemical reducing agent showed that about 30% of total OC is co-extracted alongside iron in sediments from Lake Tantaré (Joshani, 2015), although co-extraction on its own does not demonstrate co-localization nor direct bonding. Despite similar total OC contents in the surface (0-0.5 cm) sediments from both basins, more Fe-associated OC was co-extracted in the oxic Basin A compared to the anoxic

Basin B (40.7 % vs. 28.6 % of total OC), alongside about 1.6 fold more reducible iron (Joshani, 2015).

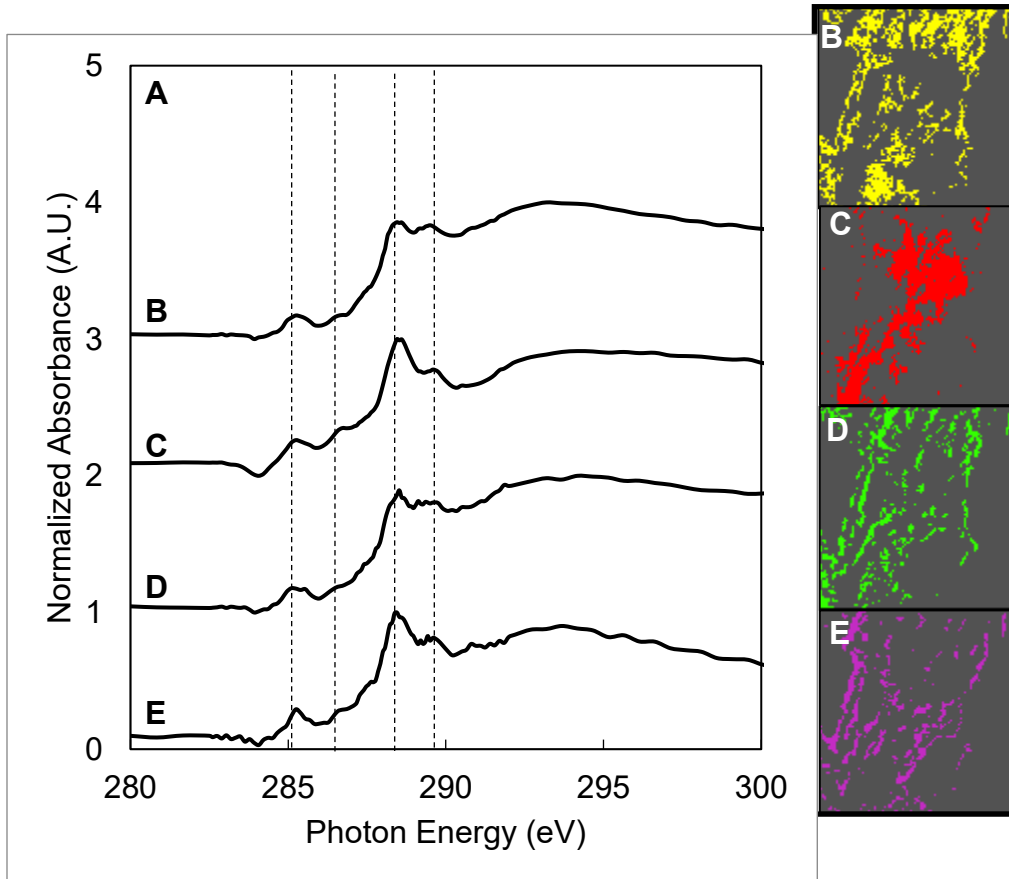


Figure 6-5: (A) C K_{1s} edge NEXAFS spectra for the authigenic iron complexes from the Teflon plate material. Each spectra corresponds to the similarly labelled cluster maps (B-E). The dashed vertical lines are located at photon energies of interest (285.1 eV, 286.6 eV, 288.6 eV and 289.5 eV).

Below a depth of 1 cm, these percentages remained lower in both basins (averages of 30.1 ± 4.9 % and 29.3 ± 7.7 % for basins A and B, respectively) (Joshani, 2015). Localization of OC onto sediment mineral surfaces was first observed at submicron scales using transmission electron microscopy (Ransom et al., 1997; Ransom et al., 1998). A practical limitation of these studies was the inability to probe the composition of the mineral matrix and associated OM, but these images were still instrumental to refuting the then generally accepted mono-layer sorption

hypothesis, which proposed that OM was sequestered in marine sediments via thin and quasi-uniform coatings on the surface of the minerals (Ransom et al., 1997). Nanoscale secondary ion mass spectrometry (NanoSIMS) has also been useful to examine organic-mineral interactions with the required resolution and showed spatial heterogeneity at sub-micron scales, improving upon previous microscopic images on soil/sediment particles by directly identifying regions containing soil OM (Mueller et al., 2012; Vogel et al., 2014). The NanoSIMS data did not provide molecular level information regarding the composition of OM or the mineral matrix in such samples, but it did confirm the presence of C and N through the measurement of soil OM secondary ions (e.g. $^{12}\text{C}^-$, $^{13}\text{C}^-$, $^{12}\text{C}^{14}\text{N}^-$ and $^{12}\text{C}^{15}\text{N}^-$) every 50 nm across the sample (Mueller et al., 2012). Recent work using STXM led a step further by demonstrating co-localization of specific elements within the mineral matrix to specific organic functionalities in a variety of sample types including soils (Lehmann et al., 2008; Solomon et al., 2012a; Chen et al., 2014) and marine sediments (Barber et al., 2017). We used this approach to show nm-scale co-localization of OC and Fe in lake Tantaré sediments, as well as in authigenic iron oxides accumulating through precipitation and/or sorption on Teflon plates just above the sediment water interface.

In sediments from the oxic Basin A, OC was unsurprisingly found co-localized to ferric iron, contrasting the anoxic Basin B, where OC was co-localized to mixed oxidation state iron. As the samples were lyophilized, it is likely that a portion of the ferrous iron was oxidized to ferric iron before X-ray analysis. However, the similar intensities of the absorption bands at 708 eV and 710 eV indicate that the sample initially contained an important proportion of ferrous iron. Low dissolved O_2 concentrations in the hypolimnion caused by seasonal redox oscillations allows for the reduction of ferric iron oxides near the sediment water interface, likely creating this pool of ferrous iron (Barber et al., 2014). Also, the presence of sorbed OM has long been shown to

poisons iron oxide crystal structures (Schwertmann, 1966) protecting them from reductive dissolution, making the presence of metastable iron oxides possible in anoxic sediments, as demonstrated for sediments from the Black Sea (Barber et al., 2017). These metastable iron oxides could trap Fe(II) into/onto Fe(III) oxides, giving rise to mixed Fe(II)/Fe(III) particles or coatings observed in this study.

A portion of the iron released during the dithionite reduction treatment of Lalonde et. al., (2012) could also be derived from Fe(II) minerals, possibly leading to an overestimation of the quantity of ferric iron associated to OM. A potentially important source of ferrous iron in these anoxic surface sediments are Fe(II) sulfur minerals such as mackinawite, greigite or pyrite. In fact, the potential existence of these species in these seasonally anoxic surface sediments supports the hypothesis of Joshani (2015), who suggested that ferrous iron phases may be artificially decreasing the measured OC:Fe molar ratios when chemically reducing sediments using the dithionite, citrate, buffer method (Lalonde et al., 2012). This potential bias affects the usefulness of OC:Fe ratios when trying to infer molecular level bonding mechanisms (Barber et al., 2017), however with little to no influence regarding the importance of this OC sequestration mechanism.

6.5.2. OC:Fe complexes in the perennially oxic Basin A

A difficulty associated with STXM analyses performed at multiple elemental edges on a single sample is the delicate balance between sample thickness and sample composition. When examining OC-mineral interactions by X-ray analysis, there must be a compromise in sample thickness to acquire high quality NEXAFS spectra, in order to look at multiple elements in a given sample. If the sample is too thick, the carbon K-edge data becomes unusable owing to the inability of these low energy X-rays to penetrate through the mineral matrix, while samples that

are too thin can lead to signal intensities that are barely above the lower limit of detection for elements with lower absorption cross-sections and molar absorptivity constants. The high OC content of the sediment samples presented here allowed for collection of higher quality NEXAFS image stacks compared to those acquired for low OC coastal and pelagic sediments (Barber et al., 2017).

From the C K_{1s} NEXAFS stacks several C organic functionalities were found co-localized to Fe(III) in the oxic basin. The absorption bands observed have been traditionally attributed to the presence of certain specific functional groups, yet in reality they arise from specific molecular orbital transitions. The absorption band at 285.1 eV arises from the $1s-\pi^*$ transitions of conjugated C=C bonds found in aromatic ring structures (Lehmann et al., 2009), or possibly from alpha carbon atoms in phenolic molecules (Solomon et al., 2012a). The absorption band observed at 286.6 eV also falls within the expected absorption band range for phenolic compounds (Lehmann et al., 2008), such as those found in lignin/tannin and their degradation products. This absorption band could also be attributed to $1s-\pi^*$ transitions for C=O bonds in ketones or even $1s-\sigma^*$ transitions for C-N bonds in pyrrolic molecules (Solomon et al., 2012a). In lacustrine sediments from regions surrounded in boreal forest, the presence of lignin/tannin and their degradation products in the form of (poly)phenols is expected, as shown recently by Guilmette et al. (2017). Interestingly, the relative proportion of these functional groups to the post-edge region of the X-ray spectra was greater for the anoxic basin compared to the oxic one (discussed further below).

The absorption band at 288.6 eV was the dominant spectral feature in all but one cluster of the sample from the oxic basin. This ubiquitous absorption band can be attributed to $1s-\pi^*$ transitions from C=O functionalities found in several organic molecules. These include carbonyl

functionalities from individual amino acids, peptides, polysaccharides, lignin/tannin, as well as the condensation products formed through interactions between these macromolecules and alteration products resulting from the partial oxidation of common biochemicals. Although, the high C/N molar ratios commonly observed for terrestrial dissolved organic matter precludes the existence of amino acids and peptides as a dominant fraction of the total sediment organic matter pool. The downshifted absorption bands at 288.0 eV in traces F and H of the anoxic basin B still falls within the expected energy range for C=O functional groups, but some feature of the surrounding C atoms is driving this absorption band to lower energies. The increased stability imparted by electron withdrawing conjugate double bond systems could explain these shifts in absorption band energies. The absorption band at 289.5 eV lends credence to the possibility of such molecules as it can arise from the 1s- σ^* or 3p transitions for carbon molecules within primary and secondary alcohols as well as from 1s- π^* transitions for C=N functionalities in amides.

There was no clear trend with specific organic functionalities being preferentially associated to ferric iron. The surface sediments from the oxic basin of Lake Tantaré are rich in iron oxides (6.3% wt/wt; Joshani, 2015), and as such the OM observed by X-ray was always found co-localized to Fe(III). Using carbon stable isotope and OC to total nitrogen (OC:TN) molar ratios, Lalonde et al. (2012) showed that iron oxides preferentially associate with specific macromolecules such as proteins and polysaccharides, although the differences were small for the only lacustrine sample included in that study. The functional groups that we found co-localized to Fe(III), namely hydroxyls and carbonyls, are similar to what has been observed in studies targeting the adsorption of model compounds to iron oxide surfaces via ligand exchange reactions (Gu et al., 1994; Gu et al., 1995). Additionally, recent work combining multiple X-ray

based techniques, including STXM and hard X-ray microprobe analysis, has demonstrated the importance of direct inner-sphere complexation between OC and Fe in a series of marine sediments from around the globe (Barber et al., 2017).

6.5.3. Authigenic OC:Fe complexes

Authigenic iron oxides were precipitated on the surface of Teflon plates inserted into the sediments from the oxic basin of Lake Tantaré. These authigenic iron oxide complexes have previously been characterized as mainly lepidocrocite and ferrihydrite (Fortin et al., 1993). In agreement with these results, the Fe L_{3,2} edge spectrum for the authigenic OC:Fe complexes was dominated by Fe(III), with the most intense spectral feature being the absorption band at ~710 eV (data not shown), in-line with the previous characterization of Fortin et al. (1993). Below, we focus on the speciation of carbon associated to these authigenic ferric iron oxides.

Interestingly, although the same OC absorption bands were observed across the surface sediments and authigenic iron oxides, the changes in the relative intensity of each absorption band suggest that the molecules they represent are different or that they are present in different proportions. Specifically, the relative intensity of the peaks at 288.6 eV and 289.5 eV vary considerably, indicating differing proportions of carbonyl and O-alkyl carbon (Solomon et al., 2012a). Trace B from Fig. 6-5 in particular is very different compared to the majority of the OM observed for the surface sediments, with the relative intensity of the 288.6 eV and 289.5 eV absorption bands being practically equal. Although similar C NEXAFS spectra were observed in Trace E from Fig. 3 (i.e., the oxic sediment), this cluster only covers a small percentage of the total mapped sample, as opposed to the authigenic iron samples in which it is the most abundant cluster (representing 37% of the mapped OM x-ray absorption spectra collected for this sample). The higher contribution of O-alkyl groups, such as primary alcohols, could be indicative of the

presence of polysaccharides (Solomon et al., 2012a). These labile organic molecules likely are stabilized by the ferric iron oxides deposited on the surface of the Teflon sheet, revealing their high affinity towards iron oxides. The affinity of polysaccharides towards ferric iron has long been observed (Jones et al., 2000; Chan et al., 2004; Ingalls et al., 2004; Chan et al., 2009), and could explain their persistence in sedimentary environments.

Additional differences in OC speciation between the oxic surface sediments and these authigenic iron-OC complexes include the presence of an additional peak at 286.6 eV (Trace C, Fig. 6-5) which has previously been attributed to phenolic or ketonic carbon (Lehmann et al., 2008; Solomon et al., 2012a). This points towards preferential binding of specific, more electron withdrawing carbon functional groups to freshly oxidized iron species. The potential sequestration of polysaccharides, amino acids and phenols by iron oxides suggests the preservation of cellulose and lignin/tannin degradation products, bio-molecules originating from woody trees.

6.5.4. OC:Fe complexes in the seasonally anoxic basin

Notable differences were observed between samples from the oxic and anoxic basins, including the resolved peak observed near 286.6 eV as well as the lack of an absorption band at 289.5 eV. As discussed above, the absorption band centered around 286.6 eV can be attributed to the presence of several functional groups including ketones, pyrroles or phenolic carbon (Lehmann et al., 2008; Solomon et al., 2012a). The lack of an aliphatic alcohol moiety is interesting, as the carbon within these molecules is more reduced than their carbonyl/carbonyl counterparts. We cannot discount the possibility that these aliphatic alcohols are just less abundant in these samples, preventing them from appearing as distinct absorbance bands and are instead masked due to other peaks in this region. Also, alcohol functionalities can still be present as phenols

absorbing around 286.6 eV. The presence of lignin/tannin (poly)phenols in such environments is likely, due to the surrounding catchment being dominated by woody gymnosperms for which lignin phenols (Hedges and Mann, 1979) and condensed tannins (Hernes and Hedges, 2004) have been used as a biomarkers.

The absorption band at 287.4 eV, attributed to aliphatic C, most apparent as a shoulder on traces D and F (Fig. 6-4) in the anoxic Basin B is notable from an OM sequestration perspective. It opens up the possibility of non-specific OM sequestration of aliphatic moieties co-precipitating along iron oxides during oscillating redox cycling. Aliphatic carbon has recently been shown to not bind to iron oxide surfaces and persists in anoxic interstitial waters (Riedel et al., 2013). The incorporation of such moieties into iron-OM complexes seems more likely in oscillating redox scenarios, such as in Basin B, where these molecules may co-precipitate alongside iron oxides. As opposed to the other observed functional groups co-localized to Fe, aliphatic functionalities do not act as molecular “latches” which could readily bind to iron oxides via the commonly proposed ligand exchange mechanism (Gu et al., 1994; Barber et al., 2017), but they could however contribute to a significant fraction of large, mostly hydrophilic macromolecules such as the carboxylic-rich aliphatic materials (CRAM) that account for a large fraction of the refractory oceanic dissolved organic carbon pool (Hertkorn et al., 2006).

Clearly, these absorption spectra represent a mixture of complex organic (macro)molecules. Compared to reference spectra for organic molecules typically associated to natural OM (Solomon et al., 2009), the spectra collected here are not easily deciphered, as is expected for natural OM. One possible macromolecular structure which could be associated with these absorbance bands would be lignin or tannin (poly)phenols and their chemically reworked

degradation products, which are likely to be present in sediments from forested Lake Tantaré Ecological Reserve (Houle, 1992).

Finally, the presence of carbonate minerals in the anoxic Basin B only is not particularly surprising as the dissolved inorganic carbon content of the sediment porewaters and overlying waters are an order of magnitude higher compared to in the perennially oxic Basin A (Clayer et al., 2016). Only the anoxic basin has porewaters saturated with respect to siderite, which is possibly the carbonate species we have observed in this study (Clayer et al., 2016). The precise nature of these carbonate minerals could not be ascertained from the C NEXAFS analysis and is outside the scope of this study.

6.6. Conclusions

Similar absorption C NEXAFS spectra have been obtained for soil OM colloids (Schumacher et al., 2005), dissolved OM from boreal forest catchments (Schumacher et al., 2006), and soils from a variety of locations (Lehmann et al., 2008) compared to the seasonally anoxic basin of Lake Tantaré. This is in contrast to the spectra obtained for the oxic basin and authigenic sediment material analyzed in this study, as well as for a series of marine sediments collected across a variety of depositional settings around the globe (Barber et al., 2017). The contrast between these studies coupled with the differences observed between basins here demonstrates potential effects of oxygen exposure regimes on organo-mineral interactions in lacustrine sediments. The presence of a permanent oxic/anoxic redox boundary within the sediments in Basin A compared to an oscillating redox boundary in Basin B could have a drastic effect on the composition of the OM sequestered via interactions with redox sensitive metal oxides (observed as Fe(III) in this study).

The OC functional groups observed in these lacustrine environments can bind readily to iron oxides through ligand exchange reactions. The surficial Fe-OH bonds from the iron oxides can be replaced with Fe-O-C bonds. These strong covalent interactions could allow for the long-term preservation of OC in boreal lakes. The observed functional groups suggest that either polysaccharides (based on the carbonyl C=O and aliphatic alcohol C-OH absorption bands), amino acid (based on the aromatic and carbonyl absorption bands), or phenolic lignin/tannin degradation products (based on the aromatic C=C, carbonyl C=O and phenolic C-OH groups) are bound to Fe oxides. This is in line with recent Fe K-edge NEXAFS analysis showing that the iron oxides complex specific OC functionalities via direct inner-sphere bonding (Barber et al., 2017).

The differences in OM composition from the oxic sediments and the authigenic iron precipitates on the Teflon plates poses an interesting question regarding whether ferric iron oxides bind to specific organic functionalities and the effect these OC:Fe complexes have on the preservation of certain organic compounds. From the data presented here, there seems to be binding of specific functionalities to the reactive iron species on the Teflon plate and some of these species survive within the sediment, indicating that only certain functionalities are actually sequestered into the sediment matrix. Even larger differences in OM speciation were observed across the sediments from the two different basins, with more polysaccharide rich OM present in the oxic sediments, and more phenolic and carboxylic functionalities in the anoxic sediments. This is in-line with previous work demonstrating that lignin phenols are degraded via non-specific oxidation reactions in oxygenated waters and sediments, while the more reactive organic species are susceptible to degradation with similar rates in both oxic and anoxic environments (Burdige,

2007). The redox cycling that occurs at the surface of the sediments from the seasonally anoxic basin allows for the possibility of different binding mechanisms between OC and Fe. Many of the functional groups observed here show a strong affinity for iron oxide surfaces and others, specifically the aliphatic moieties, are associated to iron oxides either via non-specific interactions that occur during periods of oscillating redox conditions, or because they are part of large molecules that also contain moieties with a high affinity to iron oxides. It must be noted however, that the aliphatic carbon was always observed alongside carboxyl and aromatic functional groups. The existence of CRAM as a major constituent in lacustrine organic matter has been demonstrated before (McCaul et al., 2011), yet here we show that this material is co-localized with the sediment mineral matrix. This CRAM therefore likely binds with the mineral matrix via strong inner-sphere interactions formed via ligand exchange mechanism.

The importance of iron in the diagenesis of numerous trace metals (Laforte et al., 2005; Chappaz et al., 2008a; Chappaz et al., 2008b; Feyte et al., 2010; Feyte et al., 2012) and sulfur species (Couture et al., 2016) and OM (Joshani, 2015) is well documented in Lake Tantaré. The differences in redox conditions across the two basins mimic the conditions used in a slurry incubation experiment, which showed the effect of iron oxides on the diagenesis of C and N in marine sediments (Barber et al., 2014), although in a natural setting. Here we have explored differences in OM composition across the different basins, while also comparing the OM co-localized to primarily Fe(III). Our results indicate that the redox conditions of lacustrine sediments have an impact on OM composition, yet questions still remain regarding the linkages between OM, trace metals and the bulk of the sediment mineral matrix. A combination of synchrotron approaches would be required to further address these issues.

Chapter 7: Conclusions, Perspectives and Future Work

The overall goal of this has been to better understand the fate of OM in aquatic systems, particularly focusing on its degradation and preservation during deposition and burial in marine sediments. We chose to use two different approaches: 1) using stable isotope analysis to track OM in the St. Lawrence Estuary and in slurry incubation experiments and 2) coupling multiple synchrotron x-ray based techniques in order to probe the interactions between OM and the sediment mineral matrix. The most important findings include evidence that direct covalent, inner-sphere, complexation is involved in the interactions between OM and iron oxides in marine sediments. The mutually beneficial (i.e. stabilizing both OM and Fe) nature of these interactions allows for their transport from the water column to surface sediments and possibly through the sediment oxic/anoxic redox boundary. For decades sediment geochemists have tried to probe the mechanism of interaction between OM and the sediment mineral matrix. The approach of combining linear combination fitting of X-ray absorption data with constraints derived from wet chemistry is one that could be applied to answer similar questions about the mechanism of interaction between OM and other components of the sediment mineral matrix. Specifically, this type of work could be applied to probe the interactions between organic ligands and redox sensitive manganese species, where a similar synergistic stabilization mechanism could exist (Madison et al., 2013) Recent studies showing the importance of manganese oxides on the sequestration and preservation of OM were unable to directly probe the mechanism of these interactions (Estes et al., 2017), but this could likely be accomplished using x-ray absorption spectroscopy with similar linear combination fitting constraints as those presented in this work.

The common questions binding the work presented in this thesis have revolved around elucidating the fate of OM in the water column and in surface sediments. Particular emphasis of

better understanding the mechanisms by which OM is either stabilized or remineralized. A particularly powerful finding is presented in Figure 5-6 showing the linear relationship between the amount of carbon associated to iron and the amount of iron associated to carbon across the series of coastal sediments. The data used for this figure includes a combination of synchrotron fitting results with the wet chemical measurements from Lalonde et al., 2012. The observed relationship is made more convincing by the fact that it involves data collected by two separate individuals on identical samples, using completely different approaches. The slope of 5 observed for the relationship in Figure 5-6 is essentially a molar OC:Fe ratio. Interestingly this matches well with the theoretical OC:Fe molar ratios sometimes used as an indicator of co-precipitation being the dominant interaction mechanism between OC and Fe (Poulton and Raiswell, 2005; Wagai and Mayer, 2007).

Combining the results from Chapters 4 through 6 we can begin to form a clearer understanding about the interactions between sediment OC and Fe. We show that the presence of iron oxides increases the sequestration of OM into marine sediments in the short term, while also increasing OM preservation over the course of the incubation. The Fe K-edge X-ray data shows that the interactions between OC and Fe are strong, covalent bonds that may inhibit the reductive dissolution of iron oxides while also stabilizing OM. Such strong inner-sphere interactions would be necessary for iron oxides to play a role in the preservation of OM over geologic timescales. We propose that OC and Fe form a synergistic relationship where one stabilizes the other and allows for their transport from the water column, through oxic surface sediments to the anoxic deeper sediment layers.

In addition to this geochemical message discussed above we have attempted to demonstrate the importance of proper analytical constraints when interpreting both stable isotope and synchrotron

X-ray measurements. There is an abundance of stable isotope work being done on DOC which inadequately describes or grossly underestimates the error associated with such measurements, particularly for salt water measurements. In fact while presenting the stable isotope work presented in Chapter 3 at international conferences, several researchers were shocked by the number of replicate injections being used for each datapoint. We anticipate that the inter-laboratory comparison study presented in Chapter 2 will have far reaching implications, much like the work of Sharp et al., 2002 focussing on DOC concentration measurements did in the 1990's and early 2000's. The $\delta^{13}\text{C}$ -DOC analysis method presented in this work can still be improved upon. Possible avenues of improvement include the use of a different oxidation catalyst or decreasing the volume of the Graden Instrument chemical trap. The use of less packing material would decrease void volume, decreasing the IRMS peak width. Additionally, this would allow for a lower flow of helium to be used, reducing the amount of time required to flush the chemical trap.

We hope that our work promotes the idea of wet chemistry with X-ray fitting results in order to improve the validity of such findings. This is particularly important when trying to deconvolute Fe K-edge data using linear combination fitting (Chapter 5) where there are an abundance of potential iron species that must be taken into consideration. We circumvent such limitations by using the x-ray absorption spectra from the post reduction treated sediment as a component in our fitting results, accounting for the iron species not targeted by the reduction method. It would be interesting to try and use a more refined sequential extraction procedure in order to probe the importance of OC:Fe interactions in other fractions of the sediment OC pool.

One of the major conclusions of this work involves the role of iron in the transport of OM across the oxic/anoxic redox boundary in marine sediments. A major question that remains unanswered

is the fate of OM that passes through this redox boundary and specifically the potential interactions between reduced iron species and OM. Although likely less important on a mole to mole basis, the total amount of reduced iron species observed at depth in marine sediments, most commonly in the form of iron sulfur compounds (pyrite, mackinawite and greigite) could allow for the sequestration of vast amounts of OM. Tackling this question poses a series of challenges. First, the collection of sediment samples in a truly anoxic environment is not a simple task, even using anoxic glove boxes (Edenborn et al., 1986) for sample collection is imperfect as there is still the possibility of sample oxidation during storage and transport. Ideally, the smelly (sulfide rich) anoxic muds collected during sampling cruises ought to be treated directly onboard in order to prevent this type of sampling artefact but this becomes infeasible when trying to characterize OM using powerful mass spectrometric or x-ray based analysis. On top of sampling issues, the need to maintain anoxic conditions over the course of the analysis can also raise issues. For STXM analysis, sample oxidation (by oxygen, not beam damage) over the course of the analysis can be overcome through the advent of ultra-high vacuum endstations such as the one recently installed at the Canadian Lightsource.

The use of ultra-high vacuum STXM endstations will ensure that no air is present during the analysis while also allowing for the collection of high quality nitrogen NEXAFS spectra. The addition of nitrogen, sulfur and phosphorous NEXAFS analysis, in addition to carbon and iron, will provide a comprehensive understanding of the interactions between the key components of OM and iron in the sediment mineral matrix. This ties in well with the hypothesis put for in chapter 4 regarding the potential for increased nitrogen removal by iron oxides and is something to be pursued in future studies using STXM to better understand sediment OM dynamics.

Overall, the work presented in this thesis represents an advancement in our knowledge regarding the processes that affect the preservation of OM in aquatic environments. We have explored possible OM degradation mechanisms as OM sinks within the water column of the St. Lawrence Estuary using carbon stable isotope analysis on DOC. Similarly, we used stable isotopes in order to track the fate of a pulse OM in slurry incubation experiments, finding that iron oxides help transport OM from the water column into the solid phase sediment matrix while also being the first to show an exchange between the freshly deposited and native sediment OM pool. Finally, we used a combination of synchrotron X-ray analyses in order to better understand the role of differences in bottom water oxygen content on the sequestration of OM demonstrating the importance of strong covalent inner-sphere interactions in the transport and subsequent burial/sequestration of OM in both marine and lacustrine sediments.

References

- Aiken G. R. (1992) Chloride interference in the analysis of dissolved organic carbon by the wet oxidation method. *Environ. Sci. Technol.* **26**, 2435–2439.
- Albéric P. (2011) Liquid chromatography/mass spectrometry stable isotope analysis of dissolved organic carbon in stream and soil waters. *Rapid Commun. Mass Spectrom.* **25**, 3012–3018.
- Alkhatib M., Schubert C. J., del Giorgio P. A., Gelinás Y. and Lehmann M. F. (2012) Organic matter reactivity indicators in sediments of the St. Lawrence Estuary. *Estuar. Coast. Shelf Sci.* **102**, 36–47.
- Arnarson T. S. and Keil R. G. (2007) Changes in organic matter–mineral interactions for marine sediments with varying oxygen exposure times. *Geochim. Cosmochim. Acta* **71**, 3545–3556.
- Barber A., Brandes J., Leri A., Lalonde K., Balind K., Wirick S., Wang J. and Gélina Y. (2017) Preservation of organic matter in marine sediments by inner-sphere interactions with reactive iron. *Sci. Rep.* **7**, 366.
- Barber A., Lalonde K., Mucci A. and Gélina Y. (2014) The role of iron in the diagenesis of organic carbon and nitrogen in sediments: A long-term incubation experiment. *Mar. Chem.* **162**, 1–9.
- Bauer J. E. (2002) Carbon isotopic composition of DOM. *Biogeochem. Mar. Dissolved Org. Matter*, 405–453.
- Bauer J. E. and Druffel E. R. M. (1998) Ocean margins as a significant source of organic matter to the deep open ocean. *Nature* **392**, 482–485.
- Bauer J. E., Druffel E. R., Wolgast D. M. and Griffin S. (2002) Temporal and regional variability in sources and cycling of DOC and POC in the northwest Atlantic continental shelf and slope. *Deep Sea Res. Part II Top. Stud. Oceanogr.* **49**, 4387–4419.
- Bentley S. J. and Kahlmeyer E. (2012) Patterns and mechanisms of fluvial sediment flux and accumulation in two subarctic fjords: Nachvak and Saglek Fjords, Nunatsiavut, Canada. *Can. J. Earth Sci.* **49**, 1200–1215.
- Benzerara K., Yoon T. H., Tyliszczak T., Constantz B., Spormann A. M. and Brown G. E. (2004) Scanning transmission X-ray microscopy study of microbial calcification. *Geobiology* **2**, 249–259.
- Berner R. A. (1999) A new look at the long-term carbon cycle. *Gsa Today* **9**, 1–6.
- Berner R. A. (1989) Biogeochemical cycles of carbon and sulfur and their effect on atmospheric oxygen over Phanerozoic time. *Palaeogeogr. Palaeoclimatol. Palaeoecol.* **75**, 97–122.

- Berner R. A. (2003) The long-term carbon cycle, fossil fuels and atmospheric composition. *Nature* **426**, 323–326.
- Berner R. A. (2004) *The Phanerozoic Carbon Cycle: CO₂ and O₂*, Oxford University Press.
- Bianchi T. S., Lambert C. D., Santschi P. H. and Guo L. (1997) Sources and transport of land-derived particulate and dissolved organic matter in the Gulf of Mexico (Texas shelf/slope): the use of ligninphenols and loliolides as biomarkers. *Org. Geochem.* **27**, 65–78.
- Blough N. and Del Vecchio R. (2002) Chromophoric DOM in the coastal environment. In *Biogeochemistry of marine dissolved organic matter* (eds. D. A. Hansell and D. E. Canfield). Elsevier, San Diego.
- Bock M. J. and Mayer L. M. (2000) Mesodensity organo–clay associations in a near-shore sediment. *Mar. Geol.* **163**, 65–75.
- Bouillon S., Dehairs F., Schiettecatte L.-S. and Vieira Borges A. (2007) Biogeochemistry of the Tana estuary and delta (northern Kenya). *Limnol. Oceanogr.* **52**, 46–59.
- Bouillon S., Korntheuer M., Baeyens W. and Dehairs F. (2006) A new automated setup for stable isotope analysis of dissolved organic carbon. *Limnol. Oceanogr. Methods* **4**, 216–226.
- Bouillon S., Yambélé A., Spencer R. G. M., Gillikin D. P., Hernes P. J., Six J., Merckx R. and Borges A. (2012) Organic matter sources, fluxes and greenhouse gas exchange in the Oubangui River (Congo River basin). *Biogeosciences* **9**, 2045–2062.
- Bourgault D., Galbraith P. S. and Winkler G. (2012) Exploratory observations of winter oceanographic conditions in the Saguenay Fjord. *Atmosphere-Ocean* **50**, 17–30.
- Brand W. A. (2004) Mass spectrometer hardware for analyzing stable isotope ratios. *Handb. Stable Isot. Anal. Tech.* **1**, 835–856.
- Brandes J. A., Lee C., Wakeham S., Peterson M., Jacobsen C., Wirick S. and Cody G. (2004) Examining marine particulate organic matter at sub-micron scales using scanning transmission X-ray microscopy and carbon X-ray absorption near edge structure spectroscopy. *Mar. Chem.* **92**, 107–121.
- Brothers S. M., Prairie Y. T. and Giorgio P. A. (2012) Benthic and pelagic sources of carbon dioxide in boreal lakes and a young reservoir (Eastmain-1) in eastern Canada. *Glob. Biogeochem. Cycles* **26**.
- Bugden G. L. (1981) Salt and heat budgets for the Gulf of St. Lawrence. *Can. J. Fish. Aquat. Sci.* **38**, 1153–1167.
- Burdige, D.J., 1993. The biochemistry of manganese and iron reduction in marine sediments. *Earth-Sci. Rev.* **35**, 249-283.

- Burdige D. J. (2006) *Geochemistry of marine sediments*, Princeton University Press Princeton.
- Burdige D. J. (2007) Preservation of organic matter in marine sediments: controls, mechanisms, and an imbalance in sediment organic carbon budgets? *Chem. Rev.* **107**, 467–485.
- Burdige D. J., Komada T., Magen C. and Chanton J. P. (2016) Carbon cycling in Santa Barbara Basin sediments: A modeling study. *J. Mar. Res.* **74**, 133–159.
- Cai W.-J. (2011) Estuarine and coastal ocean carbon paradox: CO₂ sinks or sites of terrestrial carbon incineration? *Annu. Rev. Mar. Sci.* **3**, 123–145.
- Cao X., Aiken G. R., Spencer R. G. M., Butler K., Mao J. and Schmidt-Rohr K. (2016) Novel insights from NMR spectroscopy into seasonal changes in the composition of dissolved organic matter exported to the Bering Sea by the Yukon River. *Geochim. Cosmochim. Acta* **181**, 72–88.
- Caupos E., Touffet A., Mazellier P. and Croue J.-P. (2015) Partitioning of the pesticide trifluralin between dissolved organic matter and water using automated SPME-GC/MS. *Environ. Sci. Pollut. Res.* **22**, 4201–4212.
- Celi L., Schnitzer M. and Nègre M. (1997) Analysis of carboxyl groups in soil humic acids by a wet chemical method, Fourier-transform infrared spectrophotometry, and solution-state carbon-13 nuclear magnetic resonance. A comparative study. *Soil Sci.* **162**, 189–197.
- Chan C. S., De Stasio G., Welch S. A., Girasole M., Frazer B. H., Nesterova M. V., Fakra S. and Banfield J. F. (2004) Microbial polysaccharides template assembly of nanocrystal fibers. *Science* **303**, 1656–1658.
- Chan C. S., Fakra S. C., Edwards D. C., Emerson D. and Banfield J. F. (2009) Iron oxyhydroxide mineralization on microbial extracellular polysaccharides. *Geochim. Cosmochim. Acta* **73**, 3807–3818.
- Chappaz A., Gobeil C. and Tessier A. (2010) Controls on uranium distribution in lake sediments. *Geochim. Cosmochim. Acta* **74**, 203–214.
- Chappaz A., Gobeil C. and Tessier A. (2008a) Geochemical and anthropogenic enrichments of Mo in sediments from perennially oxic and seasonally anoxic lakes in Eastern Canada. *Geochim. Cosmochim. Acta* **72**, 170–184.
- Chappaz A., Gobeil C. and Tessier A. (2008b) Sequestration mechanisms and anthropogenic inputs of rhenium in sediments from Eastern Canada lakes. *Geochim. Cosmochim. Acta* **72**, 6027–6036.
- Chen C., Dynes J., Wang J., Karunakaran C. and Sparks D. L. (2014) Soft X-ray Spectromicroscopy Study of Mineral-Organic Matter Associations in Pasture Soil Clay Fractions. *Environ. Sci. Technol.* **48** (12), 6678–6686.

- Chen J., Gu B., LeBoeuf E. J., Pan H. and Dai S. (2002) Spectroscopic characterization of the structural and functional properties of natural organic matter fractions. *Chemosphere* **48**, 59–68.
- Cismasu A. C., Williams K. H. and Nico P. S. (2015) Iron and carbon dynamics during aging and reductive transformation of biogenic ferrihydrite. *Environ. Sci. Technol.* **50**, 25–35.
- Clayer F., Gobeil C. and Tessier A. (2016) Rates and pathways of sedimentary organic matter mineralization in two basins of a boreal lake: Emphasis on methanogenesis and methanotrophy. *Limnol. Oceanogr.* **61** S131–S139.
- Coffin R. B. and Cifuentes L. A. (1999) Stable isotope analysis of carbon cycling in the Perdido Estuary, Florida. *Estuaries Coasts* **22**, 917–926.
- Cole J. J., Prairie Y. T., Caraco N. F., McDowell W. H., Tranvik L. J., Striegl R. G., Duarte C. M., Kortelainen P., Downing J. A., Middelburg J. J. and others (2007) Plumbing the global carbon cycle: integrating inland waters into the terrestrial carbon budget. *Ecosystems* **10**, 172–185.
- Collins M. J., Bishop A. N. and Farrimond P. (1995) Sorption by mineral surfaces: Rebirth of the classical condensation pathway for kerogen formation? *Geochim. Cosmochim. Acta* **59**, 2387–2391.
- Colombo J. C., Silverberg N. and Gearing J. N. (1996a) Biogeochemistry of organic matter in the Laurentian Trough, II. Bulk composition of the sediments and relative reactivity of major components during early diagenesis. *Mar. Chem.* **51**, 295–314.
- Colombo J. C., Silverberg N. and Gearing J. N. (1996b) Lipid biogeochemistry in the Laurentian Trough: I—fatty acids, sterols and aliphatic hydrocarbons in rapidly settling particles. *Org. Geochem.* **25**, 211–225.
- Conley D. J., Björck S., Bonsdorff E., Carstensen J., Destouni G., Gustafsson B. G., Hietanen S., Kortekaas M., Kuosa H., Markus Meier H. E. and others (2009) Hypoxia-related processes in the Baltic Sea. *Environ. Sci. Technol.* **43**, 3412–3420.
- Cornell R. M. and Schwertmann U. (2006) *The iron oxides: structure, properties, reactions, occurrences and uses.*, John Wiley & Sons.
- Couture R.-M., Fischer R., Van Cappellen P. and Gobeil C. (2016) Non-steady state diagenesis of organic and inorganic sulfur in lake sediments. *Geochim. Cosmochim. Acta* **194**, 15–33.
- Couture R.-M., Gobeil C. and Tessier A. (2008) Chronology of atmospheric deposition of arsenic inferred from reconstructed sedimentary records. *Environ. Sci. Technol.* **42**, 6508–6513.

- Déry S. J., Stieglitz M., McKenna E. C. and Wood E. F. (2005) Characteristics and trends of river discharge into Hudson, James, and Ungava Bays, 1964-2000. *J. Clim.* **18**, 2540–2557.
- Dickens A. F., Baldock J. A., Smernik R. J., Wakeham S. G., Arnarson T. S., Gélinas Y. and Hedges J. I. (2006) Solid-state ¹³C NMR analysis of size and density fractions of marine sediments: Insight into organic carbon sources and preservation mechanisms. *Geochim. Cosmochim. Acta* **70**, 666–686.
- Dickens A. F., Gélinas Y., Masiello C. A., Wakeham S. and Hedges J. I. (2004) Reburial of fossil organic carbon in marine sediments. *Nature* **427**, 336–339.
- Druffel E. R. M., Griffin S., Glynn C. S., Benner R. and Walker B. D. (2017) Radiocarbon in dissolved organic and inorganic carbon of the Arctic Ocean. *Geophys. Res. Lett.* **44**(5), 2369-2376.
- Druffel E. R. and Williams P. M. (1992) Importance of isotope measurements in marine organic geochemistry. *Mar. Chem.* **39**, 209–215.
- Eckmeier E., Rösch M., Ehrmann O., Schmidt M. W. I., Schier W. and Gerlach R. (2007) Conversion of biomass to charcoal and the carbon mass balance from a slash-and-burn experiment in a temperate deciduous forest. *The Holocene* **17**, 539–542.
- Edenborn H. M., Mucci A., Belzile N., Lebel J., Silverberg N. and SUNDBY B. (1986) A glove box for the fine-scale subsampling of sediment box cores. *Sedimentology* **33**, 147–150.
- Elliott D. L. and Short S. K. (1979) The northern limit of trees in Labrador: a discussion. *Arctic*, 201–206.
- El-Sabh M. I. and Silverberg N. (2012) *Oceanography of a large-scale estuarine system: the St. Lawrence.*, Springer Science & Business Media.
- Emerson S. and Hedges J. (2003) Sediment diagenesis and benthic flux. *Treatise Geochem.* **6**, 293–319.
- Estes E. R., Andeer P. F., Nordlund D., Wankel S. D. and Hansel C. M. (2017) Biogenic manganese oxides as reservoirs of organic carbon and proteins in terrestrial and marine environments. *Geobiology* **15**, 158–172.
- Etheridge D. M., Steele L. P., Langenfelds R. L., Francey R. J., Barnola J.-M. and Morgan V. I. (1996) Natural and anthropogenic changes in atmospheric CO₂ over the last 1000 years from air in Antarctic ice and firn. *J. Geophys. Res. Atmospheres* **101**, 4115–4128.
- Falkowski P., Scholes R. J., Boyle E., Canadell J., Canfield D., Elser J., Gruber N., Hibbard K., Högberg P., Linder S., Mackenzie F. T., Iii B. M., Pedersen T., Rosenthal Y., Seitzinger S., Smetacek V. and Steffen W. (2000) The Global Carbon Cycle: A Test of Our Knowledge of Earth as a System. *Science* **290**, 291–296.

- Farquhar G. D., Ehleringer J. R. and Hubick K. T. (1989) Carbon isotope discrimination and photosynthesis. *Annu. Rev. Plant Biol.* **40**, 503–537.
- Federherr E., Cerli C., Kirkels F., Kalbitz K., Kupka H. J., Dunsbach R., Lange L. and Schmidt T. C. (2014) A novel high-temperature combustion based system for stable isotope analysis of dissolved organic carbon in aqueous samples. I: development and validation. *Rapid Commun. Mass Spectrom.* **28**, 2559–2573.
- Ferland M.-E., Giorgio P. A., Teodoru C. R. and Prairie Y. T. (2012) Long-term C accumulation and total C stocks in boreal lakes in northern Québec. *Glob. Biogeochem. Cycles* **26**.
- Feyte S., Gobeil C., Tessier A. and Cossa D. (2012) Mercury dynamics in lake sediments. *Geochim. Cosmochim. Acta* **82**, 92–112.
- Feyte S., Tessier A., Gobeil C. and Cossa D. (2010) In situ adsorption of mercury, methylmercury and other elements by iron oxyhydroxides and organic matter in lake sediments. *Appl. Geochem.* **25**, 984–995.
- Fortin D., Leppard G. G. and Tessier A. (1993) Characteristics of lacustrine diagenetic iron oxyhydroxides. *Geochim. Cosmochim. Acta* **57**, 4391–4404.
- Fry B., Brand W., Mersch F., Tholke K. and Garitt R. (1992) Automated analysis system for coupled $\delta^{13}\text{C}$ and $\delta^{15}\text{N}$ measurements. *Anal. Chem.* **64**, 288–291.
- Geldern R., Verma M. P., Carvalho M. C., Grassa F., Delgado-Huertas A., Monvoisin G. and Barth J. A. (2013) Stable carbon isotope analysis of dissolved inorganic carbon (DIC) and dissolved organic carbon (DOC) in natural waters—Results from a worldwide proficiency test. *Rapid Commun. Mass Spectrom.* **27**, 2099–2107.
- Gélinas Y., Baldock J. A. and Hedges J. I. (2001) Demineralization of marine and freshwater sediments for CP/MAS ^{13}C NMR analysis. *Org. Geochem.* **32**, 677–693.
- Gilbert D. and Pettigrew B. (1997) Interannual variability (1948–1994) of the CIL core temperature in the Gulf of St. Lawrence. *Can. J. Fish. Aquat. Sci.* **54**, 57–67.
- Gilbert D., Sundby B., Gobeil C., Mucci A. and Tremblay G.-H. (2005) A seventy-two-year record of diminishing deep-water oxygen in the St. Lawrence estuary: The northwest Atlantic connection. *Limnol. Oceanogr.* **50**, 1654–1666.
- Goñi M. A. and Eglinton T. I. (1996) Stable carbon isotopic analyses of lignin-derived CuO oxidation products by isotope ratio monitoring-gas chromatography-mass spectrometry (irm-GC-MS). *Org. Geochem.* **24**, 601–615.
- Granskog M. A. (2012) Changes in spectral slopes of colored dissolved organic matter absorption with mixing and removal in a terrestrially dominated marine system (Hudson Bay, Canada). *Mar. Chem.* **134**, 10–17.

- Granskog M. A., Macdonald R. W., Mundy C.-J. and Barber D. G. (2007) Distribution, characteristics and potential impacts of chromophoric dissolved organic matter (CDOM) in Hudson Strait and Hudson Bay, Canada. *Cont. Shelf Res.* **27**, 2032–2050.
- Gregorio D., Bradley T., Stroud R. M., Cody G. D., Nittler L. R., David Kilkoyn A. and Wirick S. (2011) Correlated microanalysis of cometary organic grains returned by Stardust. *Meteorit. Planet. Sci.* **46**, 1376–1396.
- Gu B., Mehlhorn T. L., Liang L. and McCarthy J. F. (1996a) Competitive adsorption, displacement, and transport of organic matter on iron oxide: I. Competitive adsorption. *Geochim. Cosmochim. Acta* **60**, 1943–1950.
- Gu B., Mehlhorn T. L., Liang L. and McCarthy J. F. (1996b) Competitive adsorption, displacement, and transport of organic matter on iron oxide: II. Displacement and transport. *Geochim. Cosmochim. Acta* **60**, 2977–2992.
- Gu B., Schmitt J., Chen Z., Liang L. and McCarthy J. F. (1995) Adsorption and desorption of different organic matter fractions on iron oxide. *Geochim. Cosmochim. Acta* **59**, 219–229.
- Gu B., Schmitt J., Chen Z., Liang L. and McCarthy J. F. (1994) Adsorption and desorption of natural organic matter on iron oxide: mechanisms and models. *Environ. Sci. Technol.* **28**, 38–46.
- Guéguen C., Granskog M. A., McCullough G. and Barber D. G. (2011) Characterisation of colored dissolved organic matter in Hudson Bay and Hudson Strait using parallel factor analysis. *J. Mar. Syst.* **88**, 423–433.
- Guo L. and Macdonald R. W. (2006) Source and transport of terrigenous organic matter in the upper Yukon River: Evidence from isotope ($\delta^{13}\text{C}$, $\Delta^{14}\text{C}$, and $\delta^{15}\text{N}$) composition of dissolved, colloidal, and particulate phases. *Glob. Biogeochem. Cycles* **20**.
- Guo L., Santschi P. H., Cifuentes L. A., Trumbore S. E. and Southon J. (1996) Cycling of high-molecular-weight dissolved organic matter in the Middle Atlantic Bight as revealed by carbon isotopic (^{13}C and ^{14}C) signatures. *Limnol. Oceanogr.* **41** 1242–1252.
- Guy R. D., Fogel M. L. and Berry J. A. (1993) Photosynthetic fractionation of the stable isotopes of oxygen and carbon. *Plant Physiol.* **101**, 37–47.
- Haese R. R., Wallmann K., Dahmke A., Kretzmann U., Müller P. J. and Schulz H. D. (1997) Iron species determination to investigate early diagenetic reactivity in marine sediments. *Geochim. Cosmochim. Acta* **61**, 63–72.
- Hansell D. A. and Carlson C. A. (2014) *Biogeochemistry of marine dissolved organic matter.*, Academic Press.
- Hartland A., Baker A., Timms W., Shutova Y. and Yu D. (2012) Measuring dissolved organic carbon $\delta^{13}\text{C}$ in freshwaters using total organic carbon cavity ring-down spectroscopy (TOC-CRDS). *Environ. Chem. Lett.* **10**, 309–315.

- Hartnett H. E., Keil R. G., Hedges J. I. and Devol A. H. (1998) Influence of oxygen exposure time on organic carbon preservation in continental margin sediments. *Nature* **391**, 572–575.
- Hatcher P. G., Ravin A., Behar F. and Baudin F. (2014) Diagenesis of organic matter in a 400 m organic rich sediment core from offshore Namibia using solid state ¹³C NMR and FTIR. *Org. Geochem.* **75**, 8–23.
- Hedges J. I., Baldock J. A., Gélinas Y., Lee C., Peterson M. L. and Wakeham S. G. (2002) The biochemical and elemental compositions of marine plankton: A NMR perspective. *Mar. Chem.* **78**, 47–63.
- Hedges J. I., Baldock J. A., Gelinias Y., Lee C., Peterson M. and Wakeham S. G. (2001) Evidence for non-selective preservation of organic matter in sinking marine particles. *Nature* **409**, 801–804.
- Hedges J. I., Eglinton G., Hatcher P. G., Kirchman D. L., Arnosti C., Derenne S., Evershed R. P., Kögel-Knabner I., de Leeuw J. W., Littke R., Michaelis W. and Rullkötter J. (2000) The molecularly-uncharacterized component of nonliving organic matter in natural environments. *Org. Geochem.* **31**, 945–958.
- Hedges J. I. and Keil R. G. (1995) Sedimentary organic matter preservation: an assessment and speculative synthesis. *Mar. Chem.* **49**, 81–115.
- Hedges J. I., Keil R. G. and Benner R. (1997) What happens to terrestrial organic matter in the ocean? *Org. Geochem.* **27**, 195–212.
- Hedges J. I. and Mann D. C. (1979) The characterization of plant tissues by their lignin oxidation products. *Geochim. Cosmochim. Acta* **43**, 1803–1807.
- Hedges J. I. and Stern J. H. (1984) Carbon and nitrogen determinations of carbonate-containing solids. *Limnol. Oceanogr.* **29**, 657–663.
- Hélie J.-F. (2004) *Geochemistry and Fluxes of Organic and Inorganic Carbon in Aquatic Systems of Eastern Canada: Examples of the St. Lawrence River and Robert-Bourassa Reservoir: Isotopic Approach*. Thesis. UQAM,
- Henrichs S. M. (1995) Sedimentary organic matter preservation: an assessment and speculative synthesis—a comment. *Mar. Chem.* **49**, 127–136.
- Hernes P. J. and Hedges J. I. (2004) Tannin signatures of barks, needles, leaves, cones, and wood at the molecular level. *Geochim. Cosmochim. Acta* **68**, 1293–1307.
- Hertkorn N., Benner R., Frommberger M., Schmitt-Kopplin P., Witt M., Kaiser K., Kettrup A. and Hedges J. I. (2006) Characterization of a major refractory component of marine dissolved organic matter. *Geochim. Cosmochim. Acta* **70**, 2990–3010.

- Hocking R. K., DeBeer George S., Raymond K. N., Hodgson K. O., Hedman B. and Solomon E. I. (2010) Fe L-edge X-ray absorption spectroscopy determination of differential orbital covalency of siderophore model compounds: electronic structure contributions to high stability constants. *J. Am. Chem. Soc.* **132**, 4006–4015.
- Houle G. (1992) The Reproductive Ecology of *Abies Balsamea*, *Acer Saccharum* and *Betula Alleghaniensis* in the Tantare Ecological Reserve, Quebec. *J. Ecol.* **80**, 611–623.
- Ingalls A. E., Aller R. C., Lee C. and Wakeham S. G. (2004) Organic matter diagenesis in shallow water carbonate sediments. *Geochim. Cosmochim. Acta* **68**, 4363–4379.
- Jacobsen C., Wirick S., Flynn G. and Zimba C. (2000) Soft X-ray spectroscopy from image sequences with sub-100 nm spatial resolution. *J. Microsc.* **197**, 173–184.
- Jones F., Cölfen H. and Antonietti M. (2000) Iron oxyhydroxide colloids stabilized with polysaccharides. *Colloid Polym. Sci.* **278**, 491–501.
- Joshani A. (2015) Investigating organic matter preservation through complexation with iron oxides in Lake Tantaré. Concordia University.
- Kaiser K. and Guggenberger G. (2003) Mineral surfaces and soil organic matter. *Eur. J. Soil Sci.* **54**, 219–236.
- Kaznatcheyev K., Blomqvist I., Hallin E., Urquhart S., Loken D., Tyliczszak T., Warwick T. and Hitchcock A. P. (2004) Principles of optical design of the SM beamline at the CLS. In *SYNCHROTRON RADIATION INSTRUMENTATION: Eighth International Conference on Synchrotron Radiation Instrumentation* AIP Publishing. **8**, 1303–1307..
- Kaznatcheyev K. V., Karunakaran C., Lanke U. D., Urquhart S. G., Obst M. and Hitchcock A. P. (2007) Soft X-ray spectromicroscopy beamline at the CLS: commissioning results. *Nucl. Instrum. Methods Phys. Res. Sect. Accel. Spectrometers Detect. Assoc. Equip.* **582**, 96–99.
- Keil R. G. and Cowie G. L. (1999) Organic matter preservation through the oxygen-deficient zone of the NE Arabian Sea as discerned by organic carbon: mineral surface area ratios. *Mar. Geol.* **161**, 13–22.
- Keil R. G. and Mayer L. M. (2013) Mineral matrices and organic matter. *Treatise Geochem.* **2**.
- Keil R. G., Montluçon D. B., Prahl F. G. and Hedges J. I. (1994) Sorptive preservation of labile organic matter in marine sediments. *Nature.* **370**, 549-552
- Knicker H. (2004) Stabilization of N-compounds in soil and organic-matter-rich sediments—what is the difference? *Mar. Chem.* **92**, 167–195.
- Knicker H. and Hatcher P. G. (1997) Survival of protein in an organic-rich sediment: possible protection by encapsulation in organic matter. *Naturwissenschaften* **84**, 231–234.

- Laforte L., Tessier A., Gobeil C. and Carignan R. (2005) Thallium diagenesis in lacustrine sediments. *Geochim. Cosmochim. Acta* **69**, 5295–5306.
- Laird D. A. (2008) The Charcoal Vision: A Win–Win–Win Scenario for Simultaneously Producing Bioenergy, Permanently Sequestering Carbon, while Improving Soil and Water Quality. *Agron. J.* **100**, 178–181.
- Laidler, K.J. and Meiser, J.H., (1999) Physical Chemistry. Houghton Mifflin, Boston
- Lalonde K., Mucci A., Ouellet A. and Gélinas Y. (2012) Preservation of organic matter in sediments promoted by iron. *Nature* **483**, 198–200.
- Lalonde K., Middlestead P. and Gélinas Y. (2014a) Automation of $^{13}\text{C}/^{12}\text{C}$ ratio measurement for freshwater and seawater DOC using high temperature combustion. *Limnol Ocean. Methods* **12**, 816–829.
- Lalonde K., Vähätalo A. and Gélinas Y. (2014b) Revisiting the disappearance of terrestrial dissolved organic matter in the ocean: a $\delta^{13}\text{C}$ study. *Biogeosciences* **11**, 3707–3719.
- Laruelle G. G., Lauerwald R., Rotschi J., Raymond P. A., Hartmann J. and Regnier P. (2015) Seasonal response of air-water CO_2 exchange along the land-ocean aquatic continuum of the northeast North American coast. *Biogeosciences* **12**, 1447.
- Lee V., Whittaker L., Jaye C., Baroudi K. M., Fischer D. A. and Banerjee S. (2009) Large-area chemically modified graphene films: electrophoretic deposition and characterization by soft X-ray absorption spectroscopy. *Chem. Mater.* **21**, 3905–3916.
- de Leeuw J. W., Versteegh G. J. and van Bergen P. F. (2006) Biomacromolecules of algae and plants and their fossil analogues. In *Plants and Climate Change* Springer. 209–233.
- Lehmann J., Liang B., Solomon D., Lerotic M., Luizão F., Kinyangi J., Schäfer T., Wirick S. and Jacobsen C. (2005) Near-edge X-ray absorption fine structure (NEXAFS) spectroscopy for mapping nano-scale distribution of organic carbon forms in soil: Application to black carbon particles. *Glob. Biogeochem. Cycles* **19**.
- Lehmann J., Solomon D., Brandes J., Fleckenstein H., Jacobsen C. and Thieme J. (2009) Synchrotron-based near-edge X-ray spectroscopy of natural organic matter in soils and sediments. *Biophys.-Chem. Process. Invol. Nat. Nonliving Org. Matter Environ. Syst.*, 729–781.
- Lehmann J., Solomon D., Kinyangi J., Dathe L., Wirick S. and Jacobsen C. (2008) Spatial complexity of soil organic matter forms at nanometre scales. *Nat. Geosci.* **1**, 238–242.
- Lengke M. F., Ravel B., Fleet M. E., Wanger G., Gordon R. A. and Southam G. (2007) Precipitation of gold by the reaction of aqueous gold (III) chloride with cyanobacteria at 25–80 °C—studied by X-ray absorption spectroscopy. *Can. J. Chem.* **85**, 651–659.

- Lerotic M., Jacobsen C., Gillow J. B., Francis A. J., Wirick S., Vogt S. and Maser J. (2005) Cluster analysis in soft X-ray spectromicroscopy: finding the patterns in complex specimens. *J. Electron Spectrosc. Relat. Phenom.* **144**, 1137–1143.
- Lerotic M., Jacobsen C., Schäfer T. and Vogt S. (2004) Cluster analysis of soft X-ray spectromicroscopy data. *Ultramicroscopy* **100**, 35–57.
- Lilliefors H. W. (1967) On the Kolmogorov-Smirnov test for normality with mean and variance unknown. *J. Am. Stat. Assoc.* **62**, 399–402.
- Locat J. and Levesque C. (2009) Le fjord du Saguenay: une physiographie et un registre exceptionnels. *Rev. Sci. Eau/Journal Water Sci.* **22**, 135–157.
- Lord III C. J. (1982) A selective and precise method for pyrite determination in sedimentary materials: Research-method paper. *J. Sediment. Res.* **52**.
- Louchouart P. and Lucotte M. (1998) A historical reconstruction of organic and inorganic contamination events in the Saguenay Fjord/St. Lawrence system from preindustrial times to the present. *Sci. Total Environ.* **213**, 139–150.
- Louchouart P., Lucotte M., Canuel R., Gagné J.-P. and Richard L.-F. (1997) Sources and early diagenesis of lignin and bulk organic matter in the sediments of the Lower St. Lawrence Estuary and the Saguenay Fjord. *Mar. Chem.* **58**, 3–26.
- Luther III, G.W., Sundby, B., Lewis, B.L., Brendel, P.J. and Silverberg, N., (1997) Interactions of manganese with the nitrogen cycle: Alternative pathway to dinitrogen. *Geochimica et Cosmochimica Acta*, 61(19): 4043-4052
- Lv J., Zhang S., Wang S., Luo L., Cao D. and Christie P. (2016) Molecular-scale investigation with ESI-FT-ICR-MS on fractionation of dissolved organic matter induced by adsorption on iron oxyhydroxides. *Environ. Sci. Technol.* **50**, 2328–2336.
- Mackey D. J. and Zirino A. (1994) Comments on trace metal speciation in seawater or do “onions” grow in the sea? *Anal. Chim. Acta* **284**, 635–647.
- Madison A. S., Tebo B. M., Mucci A., Sundby B. and Luther G. W. (2013) Abundant Porewater Mn(III) Is a Major Component of the Sedimentary Redox System. *Science* **341**, 875–878.
- Magen, C., Mucci, A. and Sundby, B., (2011). Reduction Rates of Sedimentary Mn and Fe Oxides: An Incubation Experiment with Arctic Ocean Sediments. *Aquatic Geoch.* **17** , 629-643.
- Martin J. H., Knauer G. A., Karl D. M. and Broenkow W. W. (1987) VERTEX: carbon cycling in the northeast Pacific. *Deep Sea Res. Part Oceanogr. Res. Pap.* **34**, 267–285.
- Mayer L. M. (1994a) Relationships between mineral surfaces and organic carbon concentrations in soils and sediments. *Chem. Geol.* **114**, 347–363.

- Mayer L. M. (1994b) Surface area control of organic carbon accumulation in continental shelf sediments. *Geochim. Cosmochim. Acta* **58**, 1271–1284.
- McCaul M. V., Sutton D., Simpson A. J., Spence A., McNally D. J., Moran B. W., Goel A., O'Connor B., Hart K. and Kelleher B. P. (2011) Composition of dissolved organic matter within a lacustrine environment. *Environ. Chem.* **8**, 146–154.
- Molin P. and Abdi H. (1998) *New Table and Numerical Approximations for Kolmogorov-Smirnov/Lilliefors/Van Soest Normality Test.*, Technical report, University of Bourgogne.
- Morel F. M. (1993) *Principles and applications of aquatic chemistry.*, John Wiley & Sons.
- Mucci A., Starr M., Gilbert D. and Sundby B. (2011) Acidification of lower St. Lawrence Estuary bottom waters. *Atmosphere-Ocean* **49**, 206–218.
- Muccio Z. and Jackson G. P. (2009) Isotope ratio mass spectrometry. *Analyst* **134**, 213–222.
- Mueller C. W., Kölbl A., Hoeschen C., Hillion F., Heister K., Herrmann A. M. and Kögel-Knabner I. (2012) Submicron scale imaging of soil organic matter dynamics using NanoSIMS – From single particles to intact aggregates. *Org. Geochem.* **42**, 1476–1488.
- Mundy C. J., Gosselin M., Starr M. and Michelc C. (2010) Riverine export and the effects of circulation on dissolved organic carbon in the Hudson Bay system, Canada. *Limnol. Oceanogr.* **55**, 315–323.
- Navrotsky, A., Mazeina, L. and Majzlan, J., (2008) Size-driven structural and thermodynamic complexity in iron oxides. *Science*, **319**, 1635-1638
- Nguyen R. T. and Harvey H. R. (2001) Preservation of protein in marine systems: Hydrophobic and other noncovalent associations as major stabilizing forces. *Geochim. Cosmochim. Acta* **65**, 1467–1480.
- O'Day P. A., Rivera N., Root R. and Carroll S. A. (2004) X-ray absorption spectroscopic study of Fe reference compounds for the analysis of natural sediments. *Am. Mineral.* **89**, 572–585.
- Osburn C. L. and St-Jean G. (2007a) The use of wet chemical oxidation with high-amplification isotope ratio mass spectrometry (WCO-IRMS) to measure stable isotope values of dissolved organic carbon in seawater. *Limnol Ocean. Methods* **5**, 296–308.
- Osburn C. L. and St-Jean G. (2007b) The use of wet chemical oxidation with high-amplification isotope ratio mass spectrometry (WCO-IRMS) to measure stable isotope values of dissolved organic carbon in seawater. *Limnol Ocean. Methods* **5**, 296–308.
- Ouellet A., Lalonde K., Plouhinec J.-B., Soumis N., Lucotte M. and Gélinas Y. (2012) Assessing carbon dynamics in natural and perturbed boreal aquatic systems. *J. Geophys. Res. Biogeosciences 2005–2012* **117**.

- Ouellet, A., LeBerre, N., & Ayotte, C. (2013). A simplified and accurate method for the analysis of urinary metabolites of testosterone-related steroids using gas chromatography/combustion/isotope ratio mass spectrometry. *Rapid Comm. in Mass Spec*, **27**, 1739-1750.
- Pace M. L. and Prairie Y. T. (2005) Respiration in lakes. *Respir. Aquat. Ecosyst.*, 103–121.
- Panetta R. J., Ibrahim M. and Gélinas Y. (2008) Coupling a High-Temperature Catalytic Oxidation Total Organic Carbon Analyzer to an Isotope Ratio Mass Spectrometer To Measure Natural-Abundance $\delta^{13}\text{C}$ -Dissolved Organic Carbon in Marine and Freshwater Samples. *Anal. Chem.* **80**, 5232–5239.
- Perttilä M., Tulkki P. and Pietikäinen S. (1980) Mean values and trends of hydrographical and chemical properties in the Gulf of Finland 1962-1978. *Finn. Mar. Res.* **247**, 38–50.
- Peterson B. J. and Fry B. (1987) Stable isotopes in ecosystem studies. *Annu. Rev. Ecol. Syst.*, 293–320.
- Peyton G. R. (1993) The free-radical chemistry of persulfate-based total organic carbon analyzers. *Mar. Chem.* **41**, 91–103.
- Pocklington R. and Leonard J. D. (1979) Terrigenous organic matter in sediments of the St. Lawrence Estuary and the Saguenay Fjord. *J. Fish. Board Can.* **36**, 1250–1255.
- Poulton S. W. and Raiswell R. (2005) Chemical and physical characteristics of iron oxides in riverine and glacial meltwater sediments. *Chem. Geol.* **218**, 203–221.
- Preston C. M. (1996) Applications of NMR to soil organic matter analysis: history and prospects. *Soil Sci.* **161**, 144–166.
- Raiswell R. and Canfield D. E. (2012) The iron biogeochemical cycle past and present. *Geochem. Perspect.* **1**, 1–2.
- Ransom B., Bennett R. H., Baerwald R. and Shea K. (1997) TEM study of in situ organic matter on continental margins: occurrence and the “monolayer” hypothesis. *Mar. Geol.* **138**, 1–9.
- Ransom B., Kim D., Kastner M. and Wainwright S. (1998) Organic matter preservation on continental slopes: importance of mineralogy and surface area. *Geochim. Cosmochim. Acta* **62**, 1329–1345.
- Ravel B. N. M. (2005) ATHENA, ARTEMIS, HEPHAESTUS: data analysis for x-ray absorption spectroscopy using IFEFFIT. *J. Synchrotron Radiat.* **12**, 537–541.
- Raymond P. A. and Bauer J. E. (2001a) Riverine export of aged terrestrial organic matter to the North Atlantic Ocean. *Nature* **409**, 497–500.

- Raymond P. A. and Bauer J. E. (2001b) Use of ^{14}C and ^{13}C natural abundances for evaluating riverine, estuarine, and coastal DOC and POC sources and cycling: a review and synthesis. *Org. Geochem.* **32**, 469–485.
- Revesz E., Fortin D. and Paktunc D. (2015) Reductive dissolution of scorodite in the presence of *Shewanella* sp. CN32 and *Shewanella* sp. ANA-3. *Appl. Geochem.* **63**, 347–356.
- Rickard D. and Luther G. W. (2007) Chemistry of iron sulfides. *Chem. Rev.* **107**, 514–562.
- Riedel T., Iden S., Geilich J., Wiedner K., Durner W. and Biester H. (2014) Changes in the molecular composition of organic matter leached from an agricultural topsoil following addition of biomass-derived black carbon (biochar). *Org. Geochem.* **69**, 52–60.
- Riedel T., Zak D., Biester H. and Dittmar T. (2013) Iron traps terrestrially derived dissolved organic matter at redox interfaces. *Proc. Natl. Acad. Sci.* **110**, 10101–10105.
- Roehm C. L., Prairie Y. T. and Del Giorgio P. A. (2009) The pCO_2 dynamics in lakes in the boreal region of northern Québec, Canada. *Glob. Biogeochem. Cycles* **23**.
- Saliot A., Derieux S., Sadouni N., Bouloubassi I., Fillaux J., Dagaut J., Momzikoff A., Gondry G., Guillou C., Breas O., Cauwet G. and Deliat G. (2002) Winter and Spring Characterization of Particulate and Dissolved Organic Matter in the Danube–Black Sea Mixing Zone. *Estuar. Coast. Shelf Sci.* **54**, 355–367.
- Schafer C. T., Smith J. N. and Côté R. (1990) The Saguenay Fiord: A Major Tributary to the St. Lawrence Estuary. In *Oceanography of a Large-Scale Estuarine System* (eds. M. I. El-Sabh and N. Silverberg). Coastal and Estuarine Studies. Springer New York. 378–420.
- Scharlemann J. P., Tanner E. V., Hiederer R. and Kapos V. (2014) Global soil carbon: understanding and managing the largest terrestrial carbon pool. *Carbon Manag.* **5**, 81–91.
- Schierbeek H., te Braake F., Godin J.-P., Fay L.-B. and Van Goudoever J. B. (2007) Novel method for measurement of glutathione kinetics in neonates using liquid chromatography coupled to isotope ratio mass spectrometry. *Rapid Commun. Mass Spectrom.* **21**, 2805–2812.
- Schumacher M., Christl I., Scheinost A. C., Jacobsen C. and Kretzschmar R. (2005) Chemical heterogeneity of organic soil colloids investigated by scanning transmission X-ray microscopy and C-1s NEXAFS microspectroscopy. *Environ. Sci. Technol.* **39**, 9094–9100.
- Schumacher M., Christl I., Vogt R. D., Barmettler K., Jacobsen C. and Kretzschmar R. (2006) Chemical composition of aquatic dissolved organic matter in five boreal forest catchments sampled in spring and fall seasons. *Biogeochemistry* **80**, 263–275.
- Schwertmann U. (1966) Inhibitory Effect of Soil Organic Matter on the Crystallization of Amorphous Ferric Hydroxide. *Nature*, **212**, 645–646.

- Schwertmann U. and Cornell R. M. (2000) *Iron Oxides in the Laboratory*. 2 edition., Wiley-VCH, Weinheim ; New York.
- Shaffer G., Bendtsen J. and Ulloa O. (1999) Fractionation during remineralization of organic matter in the ocean. *Deep Sea Res. Part Oceanogr. Res. Pap.* **46**, 185–204.
- Sharp J. H. (1997) Marine dissolved organic carbon: Are the older values correct? *Mar. Chem.* **56**, 265–277.
- Sharp J. H., Carlson C. A., Peltzer E. T., Castle-Ward D. M., Savidge K. B. and Rinker K. R. (2002) Final dissolved organic carbon broad community intercalibration and preliminary use of DOC reference materials. *Mar. Chem.* **77**, 239–253.
- Shields M. R., Bianchi T. S., Gélinas Y., Allison M. A. and Twilley R. R. (2016) Enhanced terrestrial carbon preservation promoted by reactive iron in deltaic sediments. *Geophys. Res. Lett.* **43**, 1149–1157.
- Simpson M. J. and Hatcher P. G. (2004) Determination of black carbon in natural organic matter by chemical oxidation and solid-state ¹³C nuclear magnetic resonance spectroscopy. *Org. Geochem.* **35**, 923–935.
- Smith J. N. and Walton A. (1980) Sediment accumulation rates and geochronologies measured in the Saguenay Fjord using the Pb-210 dating method. *Geochim. Cosmochim. Acta* **44**, 225–240.
- Solomon D., Lehmann J., Harden J., Wang J., Kinyangi J., Heymann K., Karunakaran C., Lu Y., Wirick S. and Jacobsen C. (2012a) Micro- and nano-environments of carbon sequestration: Multi-element STXM–NEXAFS spectromicroscopy assessment of microbial carbon and mineral associations. *Chem. Geol.* **329**, 53–73.
- Solomon D., Lehmann J., Kinyangi J., Liang B., Heymann K., Dathe L., Hanley K., Wirick S. and Jacobsen C. (2009) Carbon (1s) NEXAFS spectroscopy of biogeochemically relevant reference organic compounds. *Soil Sci. Soc. Am. J.* **73**, 1817–1830.
- Solomon D., Lehmann J., Wang J., Kinyangi J., Heymann K., Lu Y., Wirick S. and Jacobsen C. (2012b) Micro- and nano-environments of C sequestration in soil: A multi-elemental STXM–NEXAFS assessment of black C and organomineral associations. *Sci. Total Environ.* **438**, 372–388.
- Spiker E. C. and Rubin M. (1975) Petroleum pollutants in surface and groundwater as indicated by the carbon-14 activity of dissolved organic carbon. *Science* **187**, 61–64.
- Starink, R.J., and Visser, R.G. iis Interlaboratory Studies: Protocol for the Organisation Statistics and Evaluation. Iis-protocol. 2014
- Stepanauskas R., Jørgensen N. O., Eigaard O. R., Žvikas A., Tranvik L. J. and Leonardson L. (2002) Summer inputs of riverine nutrients to the Baltic Sea: bioavailability and eutrophication relevance. *Ecol. Monogr.* **72**, 579–597.

- St-Onge G. and Hillaire-Marcel C. (2001) Isotopic constraints of sedimentary inputs and organic carbon burial rates in the Saguenay Fjord, Quebec. *Mar. Geol.* **176**, 1–22.
- Straneo F. and Saucier F. (2008) The outflow from Hudson Strait and its contribution to the Labrador Current. *Deep Sea Res. Part Oceanogr. Res. Pap.* **55**, 926–946.
- Stumm, W. and Morgan, J.J., (1970) Aquatic Chemistry: An introduction emphasizing chemical equilibria in natural waters. **1**. Wiley-Interscience.
- Sugimura Y. and Suzuki Y. (1988) A high-temperature catalytic oxidation method for the determination of non-volatile dissolved organic carbon in seawater by direct injection of a liquid sample. *Mar. Chem.* **24**, 105–131.
- Tegelaar E. W., De Leeuw J. W., Derenne S. and Largeau C. (1989) A reappraisal of kerogen formation. *Geochim. Cosmochim. Acta* **53**, 3103–3106.
- Telang S. A., Pocklington R., Naidu A. S., Romankevich E. A., Gitelson I. I. and Gladyshev M. I. (1991) Carbon and mineral transport in major North American, Russian arctic, and Siberian rivers: The St. Lawrence, the Mackenzie, the Yukon, the arctic Alaskan rivers, the arctic basin rivers in the Soviet Union, and the Yenisei. *Biogeochem. Major World Rivers* **42**, 75–104.
- Tessier A., Campbell P. G. and Bisson M. (1979) Sequential extraction procedure for the speciation of particulate trace metals. *Anal. Chem.* **51**, 844–851.
- Tessier A., Gobeil C. and Laforte L. (2014) Reaction rates, depositional history and sources of indium in sediments from Appalachian and Canadian Shield lakes. *Geochim. Cosmochim. Acta* **137**, 48–63.
- Thieme J., Sedlmair J., Gleber S.-C., Prietzel J., Coates J., Eusterhues K., Abbt-Braun G. and Salome M. (2010) X-ray spectromicroscopy in soil and environmental sciences. *J. Synchrotron Radiat.* **17**, 149–157.
- Thurman E. M. (1985) *Organic geochemistry of natural waters.*, Springer.
- Tissot B. P. and Welte D. H. (1978) Petroleum formation and occurrence: a new approach to oil and gas exploration. **538**, 323-324.
- Tranvik L. J., Downing J. A., Cotner J. B., Loiselle S. A., Striegl R. G., Ballatore T. J., Dillon P., Finlay K., Fortino K., Knoll L. B., Kortelainen P. L., Kutser T., Larsen S., Laurion I., Leech D. M., McCallister S. L., McKnight D. M., Melack J. M., Overholt E., Porter J. A., Prairie Y., Renwick W. H., Roland F., Sherman B. S., Schindler D. W., Sobek S., Tremblay A., Vanni M. J., Verschoor A. M., von Wachenfeldt E. and Weyhenmeyer G. A. (2009) Lakes and reservoirs as regulators of carbon cycling and climate. *Limnol. Oceanogr.* **54**, 2298–2314.
- Tremblay L. and Gagné J.-P. (2009) Organic matter distribution and reactivity in the waters of a large estuarine system. *Mar. Chem.* **116**, 1–12.

- Vogel C., Mueller C. W., Höschen C., Buegger F., Heister K., Schulz S., Schloter M. and Kögel-Knabner I. (2014) Submicron structures provide preferential spots for carbon and nitrogen sequestration in soils. *Nat. Commun.* **5**, 2947.
- Vogelsang V., Kaiser K., Wagner F. E., Jahn R. and Fiedler S. (2016) Transformation of clay-sized minerals in soils exposed to prolonged regular alternation of redox conditions. *Geoderma* **278**, 40–48.
- Wagai R. and Mayer L. M. (2007) Sorptive stabilization of organic matter in soils by hydrous iron oxides. *Geochim. Cosmochim. Acta* **71**, 25–35.
- Wang X.-C. and Druffel E. R. M. (2001) Radiocarbon and stable carbon isotope compositions of organic compound classes in sediments from the NE Pacific and Southern Oceans. *Mar. Chem.* **73**, 65–81.
- Ward N. D., Bianchi T. S., Medeiros P. M., Seidel M., Richey J. E., Keil R. G. and Sawakuchi H. O. (2017) Where carbon goes when water flows: Carbon cycling across the aquatic continuum. *Front. Mar. Sci.* **4** Art. No 74.
- Williams P. le B. (1975) Biological and chemical aspects of dissolved organic material in sea water. *Chem Ocean.*
- Williams P. M. and Druffel E. R. (1987) Radiocarbon in dissolved organic matter in the central North Pacific Ocean. *Nature* **330**, 246–248.
- Wilton D. H. (1996) Metallogenic overview of the Nain Province, northern Labrador. *CIM Bull.*, 43–52.
- Xie H., Aubry C., Bélanger S. and Song G. (2012) The dynamics of absorption coefficients of CDOM and particles in the St. Lawrence estuarine system: Biogeochemical and physical implications. *Mar. Chem.* **128**, 44–56.
- Yamashita Y., McCallister S. L., Koch B. P., Gonsior M. and Jaffé R. (2015) Dynamics of dissolved organic matter in fjord ecosystems: Contributions of terrestrial dissolved organic matter in the deep layer. *Estuar. Coast. Shelf Sci.* **159**, 37–49.
- Yeats P. A. and Bowers J. M. (1976) Trace metals in the waters of the Saguenay fjord. *Can. J. Earth Sci.* **13**, 1319–1327.
- Zee C. van der, Roberts D. R., Rancourt D. G. and Slomp C. P. (2003) Nanogoethite is the dominant reactive oxyhydroxide phase in lake and marine sediments. *Geology* **31**, 993–996.
- Zhang Y. and Xie H. (2015) Photomineralization and photomethanification of dissolved organic matter in Saguenay River surface water. *Biogeosciences* **12**, 6823–6836.
- Zonneveld K. A. F., Versteegh G. J. M., Kasten S., Eglinton T. I., Emeis K.-C., Huguet C., Koch B. P., de Lange G. J., De Leeuw J. W. and Middelburg J. J. (2010) Selective preservation

of organic matter in marine environments; processes and impact on the sedimentary record. *Biogeosciences* 7.

Appendix A1

Supplementary Materials for

Stable Isotope Analysis of Dissolved Organic Carbon in the

Canada's Eastern Coastal Waters

Andrew Barber, Maude Sirois, Gwénaëlle Chaillou, Yves Gélinas

This file includes:

Supplementary Tables A1-A3

Table A1-1: $\delta^{13}\text{C}$ -DOC signatures and DOC concentrations for the Saguenay Fjord

Station	Latitude	Longitude	Depth (m)	$\delta^{13}\text{C}$ -DOC (‰)	S.D.	[DOC] (mg/L)	S.D.
Sag 02	48.33876	-70.85307	2.4	-26.9	0.1	4.63	0.46
Sag 09	48.35032	-70.80098	2.2	-26.8	0.1	4.28	0.25
SF	48.42125	-70.85732	2.1	-26.9	0.0	4.37	0.08
SAG 05	48.41291	-70.82383	2.1	-26.6	0.0	4.05	0.18
SAG 06	48.40977	-70.74874	2.1	-26.5	0.1	4.86	0.07
SAG 15	48.36075	-70.69532	2.3	-26.6	0.1	4.89	0.18
SAG 20	48.37061	-70.57645	2.2	-26.7	0.1	5.10	0.07
SAG 25	48.36357	-70.51018	2.2	-26.3	0.2	4.97	0.12
SAG 30	48.36039	-70.40601	2.2	-26.7	0.2	5.25	0.01
	48.26225	-70.14783	259	-24.6	0.2	1.46	0.02
SAG 36	48.22835	-69.91226	2.3	-26.4	0.1	4.92	0.11
SAG 42	48.13698	-69.75187	2.3	-26.6	0.0	5.06	0.06
SAG 48	48.33876	-70.85307	2	-26.3	0.1	5.04	0.13

Table A1-2: $\delta^{13}\text{C}$ -DOC signatures and DOC concentrations for the Upper St. Lawrence Estuary

Station	Latitude	Longitude	Depth (m)	$\delta^{13}\text{C}$ -DOC (‰)	S.D.	[DOC] (mg/L)	S.D.
1	46.84526	-71.15052	3	-26.3	0.2	2.36	0.19
2	46.91297	-70.87427	3	-26.6	0.2	2.54	0.11
3	47.03361	-70.76152	3	-26.8	0.2	2.67	0.10
4	47.09138	-70.71653	3	-26.9	0.1	2.88	0.07
5	47.17287	-70.63157	3	-26.8	0.1	4.55	0.07

6	47.23418	-70.55795	3	-26.8	0.1	3.85	0.09
	47.23418	-70.55795	25	-25.7	0.1	3.24	0.04
7	47.43972	-70.24386	3	-26.0	0.1	2.57	0.04
8	47.51540	-70.18081	3	-25.3	0.2	2.31	0.03
9	47.59692	-69.99880	3	-25.5	0.1	2.20	0.07
	47.59692	-69.99880	56	-24.7	0.1	1.49	0.07
10	47.75144	-69.89859	3	-25.6	0.1	2.31	0.09
	47.75144	-69.89859	142	-24.5	0.2	1.46	0.04
11	47.91444	-69.77978	3	-25.1	0.2	2.24	0.08
	47.91444	-69.77978	115	-24.7	0.5	1.25	0.03
12	48.09459	-69.43394	3	-24.9	0.2	2.03	0.09

Table A1-3: $\delta^{13}\text{C}$ -DOC signatures and DOC concentrations for the Lower St. Lawrence Estuary and Gulf

Station	Latitude	Longitude	Depth (m)	$\delta^{13}\text{C}$ -DOC (‰)	S.D.	[DOC] (mg/L)	S.D.
13	48.28947	-69.37949	3	-22.4	0.1	1.38	0.04
	48.28947	-69.37949	70	-19.9	0.2	1.05	0.11
	48.28947	-69.37949	200	-20.5	1.2	0.94	0.03
	48.28947	-69.37949	318	-20.7	0.7	0.95	0.08
14	48.41984	-69.11667	3	-22.9	1.1	1.03	0.10
	48.41984	-69.11667	65	-23.2	0.2	1.55	0.11
	48.41984	-69.11667	200	-21.8	0.3	1.10	0.11
	48.41984	-69.11667	295	-21.5	0.1	0.94	0.02
15	48.63910	-68.63350	3	-23.8	0.3	1.37	0.09
	48.63910	-68.63350	25	-23.5	0.2	1.22	0.04
	48.63910	-68.63350	245	-23.9	0.6	0.76	0.02

	48.63910	-68.63350	316	-23.4	0.3	0.76	0.01
16	48.72578	-68.65820	3	-24.6	0.2	1.72	0.02
	48.72578	-68.65820	50	-21.9	0.2	1.15	0.10
	48.72578	-68.65820	200	-22.6	0.8	0.99	0.08
	48.72578	-68.65820	338	-21.5	0.4	0.93	0.09
17	48.94544	-68.09631	3	-23.2	0.3	1.88	0.03
	48.94544	-68.09631	45	-22.0	0.4	1.35	0.03
	48.94544	-68.09631	200	-21.8	0.2	1.20	0.06
	48.94544	-68.09631	305	-21.7	0.5	1.34	0.16
18	49.07803	-67.30275	3	-23.8	0.2	1.97	0.08
	49.07803	-67.30275	50	-21.6	0.2	1.24	0.06
	49.07803	-67.30275	200	-21.6	1.0	1.17	0.17
	49.07803	-67.30275	311	-21.5	0.8	0.75	0.02
19	49.12020	-67.27840	3	-23.8	0.1	1.63	0.06
	49.12020	-67.27840	25	-23.0	0.1	1.32	0.04
	49.12020	-67.27840	250	-22.6	0.2	0.95	0.05
	49.12020	-67.27840	319	-22.9	0.2	0.87	0.05
20	50.04440	-66.37970	3	-23.5	0.1	1.45	0.10
	50.04440	-66.37970	35	-21.4	0.3	0.91	0.02
	50.04440	-66.37970	150	-20.6	0.4	1.00	0.05
	50.04440	-66.37970	196	-21.6	0.6	1.24	0.08
21	49.97840	-66.22880	4	-23.7	0.5	1.34	0.02
	49.97840	-66.22880	30	-22.8	0.4	1.24	0.10
	49.97840	-66.22880	210	-24.8	0.1	0.95	0.15
	49.97840	-66.22880	241	-24.5	0.5	0.82	0.02
22	49.42298	-66.32401	3	-23.2	0.6	1.29	0.02

	49.42298	-66.32401	25	-22.2	0.1	0.96	0.04
	49.42298	-66.32401	200	-22.2	0.9	0.85	0.19
	49.42298	-66.32401	317	-21.8	0.7	0.80	0.20
23	49.50040	-65.99810	3	-23.8	0.4	1.46	0.34
	49.50040	-65.99810	30	-22.8	0.4	1.21	0.05
	49.50040	-65.99810	255	-22.9	0.2	1.07	0.10
	49.50040	-65.99810	324	-22.2	0.5	0.86	0.07
24	49.48956	-65.22160	3	-23.5	0.4	1.82	0.07
	49.48956	-65.22160	35	-22.3	0.2	1.12	0.05
	49.48956	-65.22160	200	-21.4	0.3	0.78	0.11
	49.48956	-65.22160	350	-22.1	0.3	0.69	0.06
25	49.25310	-64.24982	3	-25.7	0.1	2.03	0.10
	49.25310	-64.24982	50	-21.5	0.4	1.04	0.11
	49.25310	-64.24982	250	-20.5	0.5	0.64	0.04
	49.25310	-64.24982	373	-22.4	0.3	0.87	0.11
26	49.29000	-63.98760	4	-23.0	0.4	1.49	0.06
	49.29000	-63.98760	30	-22.8	0.4	1.38	0.17
	49.29000	-63.98760	240	-21.5	0.3	0.91	0.05
	49.29000	-63.98760	370	-23.5	0.1	0.82	0.06
27	48.97207	-63.12904	3	-20.5	0.4	1.02	0.05
	48.97207	-63.12904	90	-20.9	0.3	0.88	0.12
	48.97207	-63.12904	200	-19.9	0.3	0.72	0.11
	48.97207	-63.12904	391	-20.3	0.7	0.64	0.05
28	48.55070	-62.24940	5	-23.7	0.2	1.58	0.12
	48.55070	-62.24940	50	-23.7	0.3	1.32	0.13
	48.55070	-62.24940	250	-22.8	0.7	1.11	0.03

	48.55070	-62.24940	437	-23.8	0.9	1.17	0.24
29	48.40284	-60.74993	3	-23.4	0.3	1.12	0.05
	48.40284	-60.74993	40	-23.3	0.2	1.12	0.12
	48.40284	-60.74993	300	-23.3	0.2	0.83	0.02
30	47.50000	-60.08330	4	-23.0	0.2	1.69	0.04
	47.50000	-60.08330	20	-21.4	0.3	1.26	0.07
	47.50000	-60.08330	120	-22.5	0.1	1.44	0.24
	47.50000	-60.08330	250	-22.9	0.5	1.05	0.04
31	47.18640	-59.53830	3	-24.7	0.2	1.54	0.07
	47.18640	-59.53830	40	-24.3	0.1	1.25	0.05
	47.18640	-59.53830	100	-24.4	0.3	1.63	0.26
	47.18640	-59.53830	225	-24.3	0.1	1.23	0.08
32	50.22320	-58.46580	5	-22.1	0.2	1.14	0.02
	50.22320	-58.46580	40	-21.5	0.3	1.15	0.07
	50.22320	-58.46580	250	-22.1	0.2	1.05	0.02
	50.22320	-58.46580	320	-22.1	0.5	0.82	0.05

Appendix 2

Supplementary Materials for

The role of iron in the diagenesis of organic carbon and nitrogen in sediments:

A long-term incubation experiment

Andrew Barber, Karine Lalonde, Alfonso Mucci, Yves Gélinas

This file includes:

Time series of $\delta^{13}\text{C}$ of DOC

Iron concentration profiles

Supplementary Figures A2-1 to A2-14

Calculations for thermodynamic feasibility of feammox in marine sediments

Supplementary Information

This supplementary material section presents details and data that, due to space constraints, could not be included in the original manuscript. It is separated into three sections: the first section shows $\delta^{13}\text{C}$ DOC time series for replicate vials of each redox and amendment condition, the second shows dissolved iron concentration in control vials for each redox condition and the third deals with thermodynamic calculations of Feammox feasibility in marine sediments.

Time series of $\delta^{13}\text{C}$ of DOC

The concentration of the algal tracer in solution decreases throughout the incubation, following first order kinetics down to a relatively stable asymptotic value, attained within 30 to 150 days of the start of the incubation, depending on redox condition. Final DOC concentrations are given in Table 1 of the manuscript. Table 2 of the manuscript also shows the degradation rate and half-life of the DOC, the latter being 2 to 3 times shorter under oxic rather than anaerobic conditions. These rate constants are calculated from the decrease in DOC concentrations between sampling days, as discussed in the manuscript.

This section of the supplementary information shows time series of DOC concentrations, concomitantly to its $\delta^{13}\text{C}$ signature. Profiles of replicate vials are arranged firstly by amendment condition and secondly by redox condition. Timepoint values for each of the duplicate vials are shown as either triangles for the first vials (V1) or squares for the second vials (V2) of each condition. For the iron-amended condition, only one vial was measured for each of the three redox conditions. All concentrations (in $\mu\text{g mL}^{-1}$) are represented by white symbols whereas $\delta^{13}\text{C}$ (in ‰) values are shown in teal. Background plot colors

were modified to indicate the redox condition during sampling, either oxic or anoxic, and to highlight trends observed in DOC concentration or $\delta^{13}\text{C}$ upon changes in redox condition. A white background was used for samples taken under oxic conditions, whereas a grey background was used for samples taken under anoxic conditions. We outline important trends observed for each amendment condition within the corresponding sub-section below. Note that errors on $\delta^{13}\text{C}$ measurements are slightly higher for amendment conditions in which the organic tracer was not added, due to lower DOC concentrations.

OM amended vials

For all redox conditions of this amendment scenario, $\delta^{13}\text{C}$ drifts from the depleted signature of the tracer ($-41.34\text{‰} \pm 0.12\text{‰}$) to a more enriched signature (between -30 and -36‰), demonstrating partial degradation, release and desorption of soluble material from the native sediment organic matter ($\delta^{13}\text{C} = -24.29 \pm 0.10\text{‰}$) into solution.

Because of higher DOC degradation rates under oxic conditions, we see a steeper decrease in DOC concentrations in oxic vials relative to anoxic vials. Under mixed redox conditions, the decomposition of DOC follows a segmented decrease, with slower DOC losses during the initial anoxic segment, followed by a sharper drop during oxic subsampling. We do not observe any clear trend in DOC concentrations during subsequent shifts in redox condition.

Oxic condition

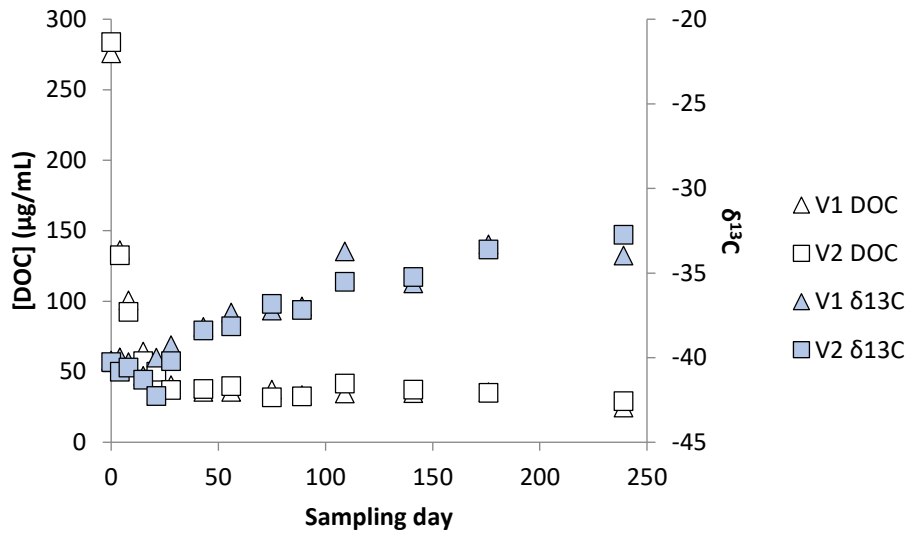


Figure A2-1: The temporal evolution of the DOC concentration (white) and $\delta^{13}\text{C}$ signature (teal) for the oxic, OM amended scenario. V1 and V2 each represent duplicate vials.

Mixed redox condition

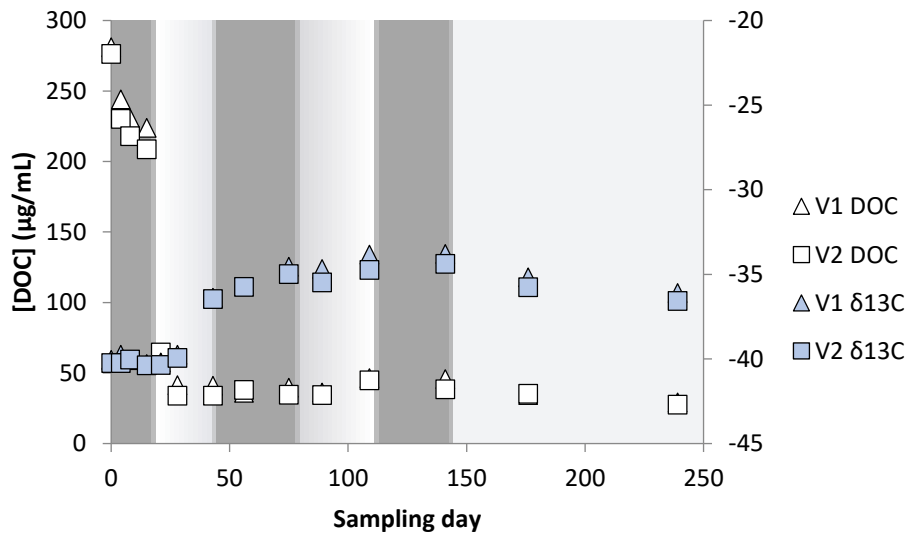


Figure A2-2: The temporal evolution of the DOC concentration (white) and $\delta^{13}\text{C}$ signature (teal) for the mixed redox, OM amended scenario. Periods appearing with a grey background were anoxic at the time of subsampling while those appearing on a white background were subsampled while the vials were maintained under oxic conditions. V1 and V2 each represent duplicate vials.

Anoxic condition

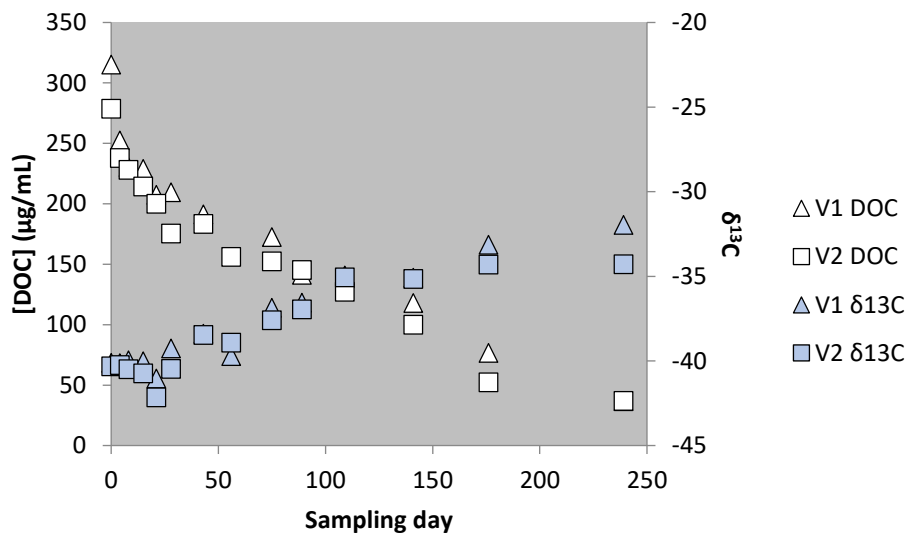


Figure A2-3: The temporal evolution of the DOC concentration (white) and $\delta^{13}\text{C}$ signature (teal) for the anoxic, OM amended scenario. V1 and V2 each represent duplicate vials.

Fe and OM amendment scenario

DOC concentrations and $\delta^{13}\text{C}$ profiles are similar for vials that were both iron- & OM-amended and those amended only with OM. We see similar degradation profiles, with accentuated decomposition upon exposure to oxygen. As discussed in the manuscript, the precipitation of iron oxides in the oxic and mixed redox vials of this amendment condition, increases the partitioning of DOC from solution onto solid particles, therefore reducing the DOC concentrations compared to vials amended with OM only (see Table 1 of manuscript). Note that there is an initial DOC concentration discrepancy between duplicate vials of the anoxic condition of Fe and OM amendment scenario, which is carried over to the following time points. The slope of the DOC concentration decrease is however not affected, therefore both plots were used to calculate the rate of DOC decomposition (Table 2 of manuscript).

A noteworthy feature of these $\delta^{13}\text{C}$ -DOC plots is the initial drop in $\delta^{13}\text{C}$ observed in oxic vials. This feature is not observed in vials amended with OM only. We postulate that the decrease in $\delta^{13}\text{C}$ reflects the preferential absorption and/or coagulation of $\delta^{13}\text{C}$ -enriched DOC with iron oxides, leaving in solution $\delta^{13}\text{C}$ -depleted DOC. This is consistent with the comparison of solid-state $\delta^{13}\text{C}$ signatures of iron-associated versus non-iron-associated OC in marine sediments, reported previously (Lalonde et al., 2012). A similar $\delta^{13}\text{C}$ drop (though not as important) is observed upon transitioning between anoxic and oxic conditions in the mixed redox scenario, also likely caused by the adsorption and/or coagulation of $\delta^{13}\text{C}$ -enriched molecules upon precipitation of iron oxides.

Oxic condition

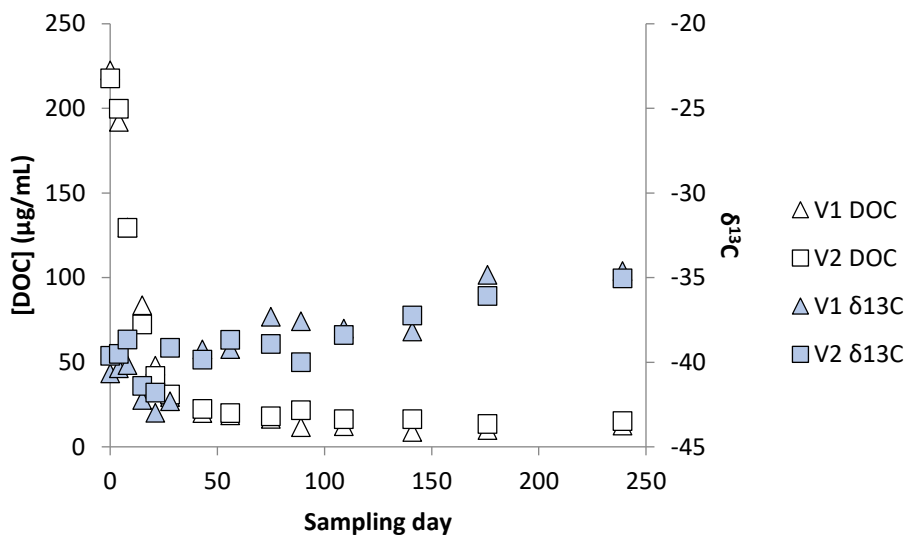


Figure A2-4: The temporal evolution of the DOC concentration (white) and $\delta^{13}\text{C}$ signature (teal) for the oxic, Fe and OM amended scenario. V1 and V2 each represent duplicate vials.

Mixed redox condition

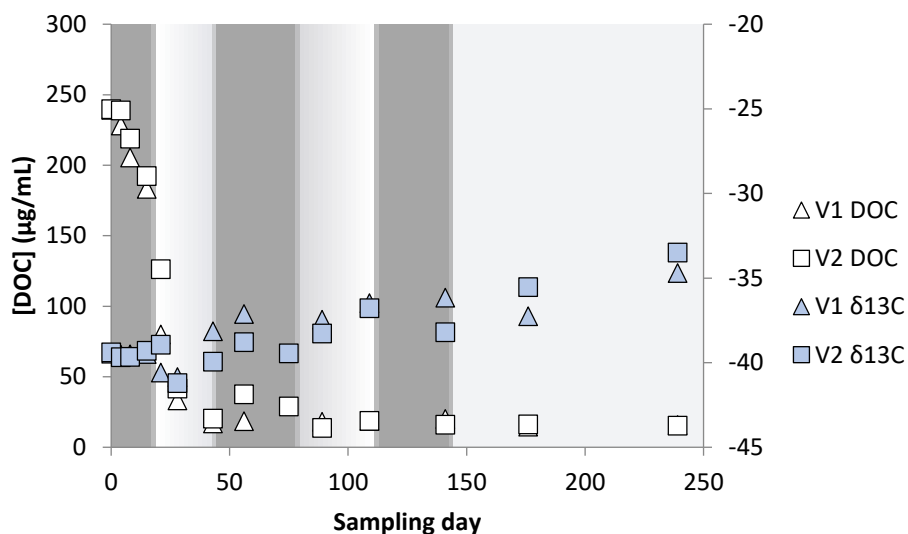


Figure A2-5: The temporal evolution of the DOC concentration (white) and $\delta^{13}\text{C}$ signature (teal) for the mixed redox, Fe and OM amended scenario. Periods appearing with a grey background were anoxic at the time of subsampling while those appearing on a white background were subsampled while the vials were maintained under oxic conditions. V1 and V2 each represent duplicate vials.

Anoxic condition

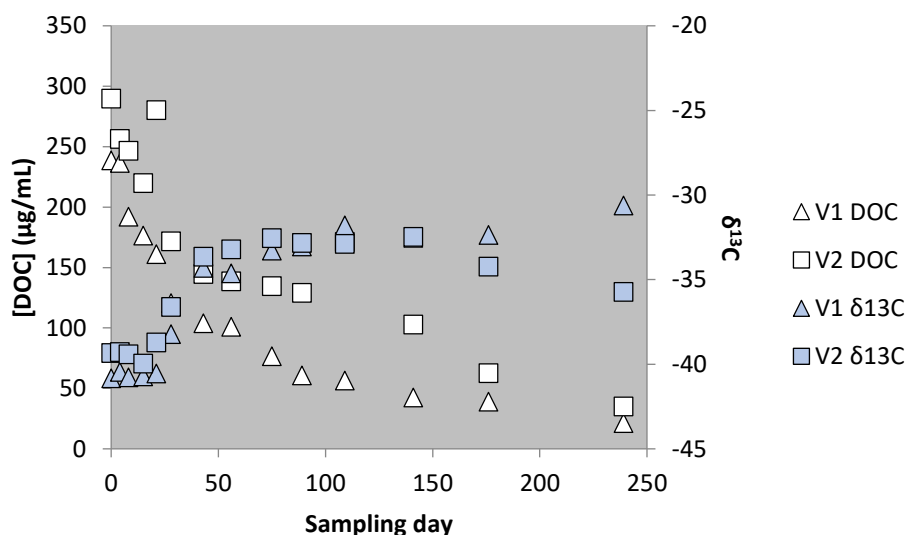


Figure A2-6: The temporal evolution of the DOC concentration (white) and $\delta^{13}\text{C}$ signature (teal) for the anoxic, Fe and OM amended scenario. V1 and V2 each represent duplicate vials.

Control scenario

DOC concentrations measured in the control scenario are much lower than for the OM-amended scenarios. Concentrations start at 2 to 4 $\mu\text{g mL}^{-1}$, increasing progressively during the course of the experiment. $\delta^{13}\text{C}$ values do not seem to follow any obvious pattern in mixed redox and anoxic incubations, but become progressively more depleted in oxic vials.

Oxic condition

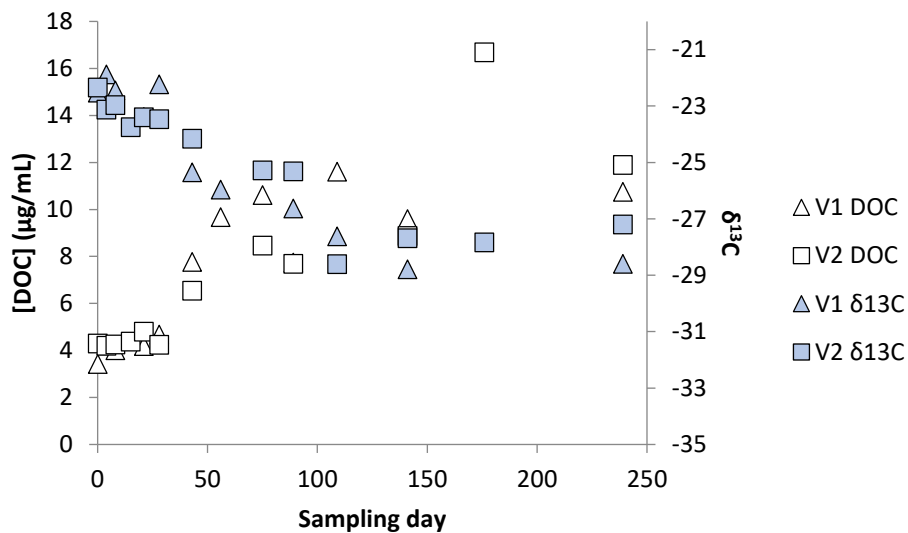


Figure A2-7: The temporal evolution of the DOC concentration (white) and $\delta^{13}\text{C}$ signature (teal) for the oxic, control scenario. V1 and V2 each represent duplicate vials.

Mixed Redox condition

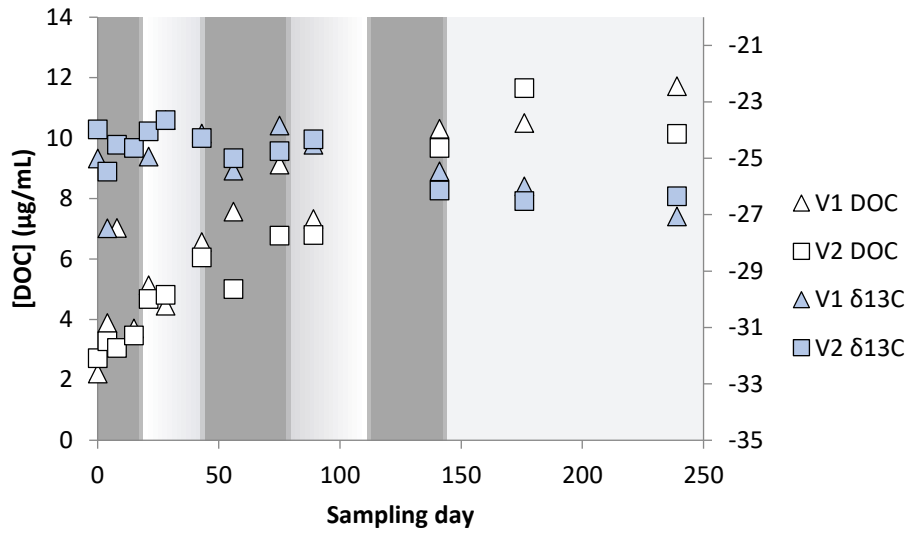


Figure A2-8: The temporal evolution of the DOC concentration (white) and $\delta^{13}\text{C}$ signature (teal) for the mixed redox, control scenario. Periods appearing with a grey background were anoxic at the time of subsampling while those appearing on a white background were subsampled while the vials were maintained under oxic conditions. V1 and V2 each represent duplicate vials.

Anoxic Condition

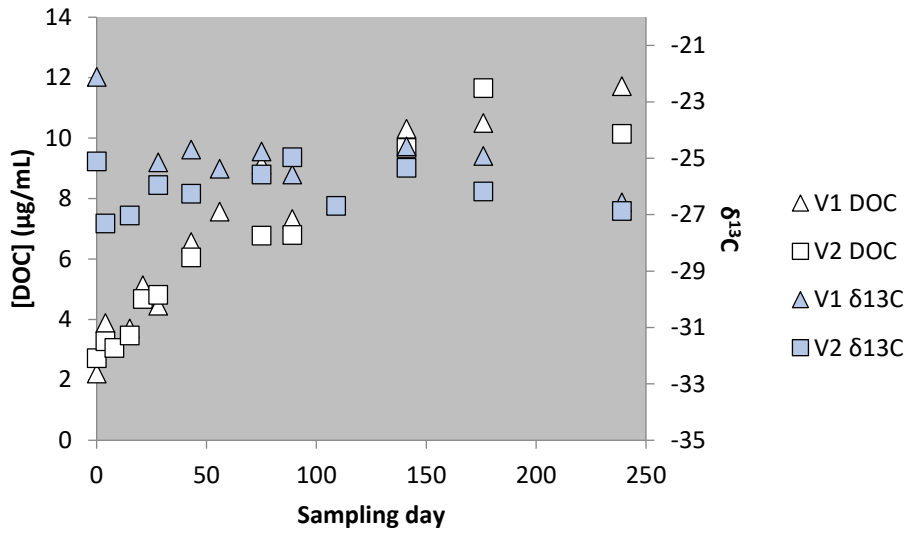


Figure A2-9: The temporal evolution of the DOC concentration (white) and $\delta^{13}\text{C}$ signature (teal) for the anoxic, control scenario. V1 and V2 each represent duplicate vials.

Fe amended scenario

DOC concentration and $\delta^{13}\text{C}$ profiles are similar for control and iron-amended scenarios. Increased partitioning of DOC onto solid particles decreases DOC concentrations, as shown in Table 4-1 of the manuscript.

Oxic condition

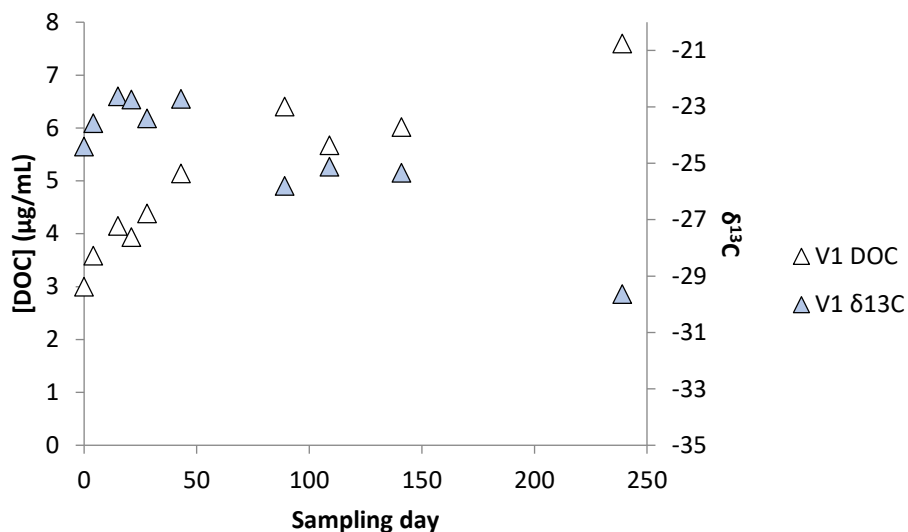


Figure A2-10: The temporal evolution of the DOC concentration (white) and $\delta^{13}\text{C}$ signature (teal) for the oxic, Fe amended scenario. V1 and V2 each represent duplicate vials.

Mixed redox condition

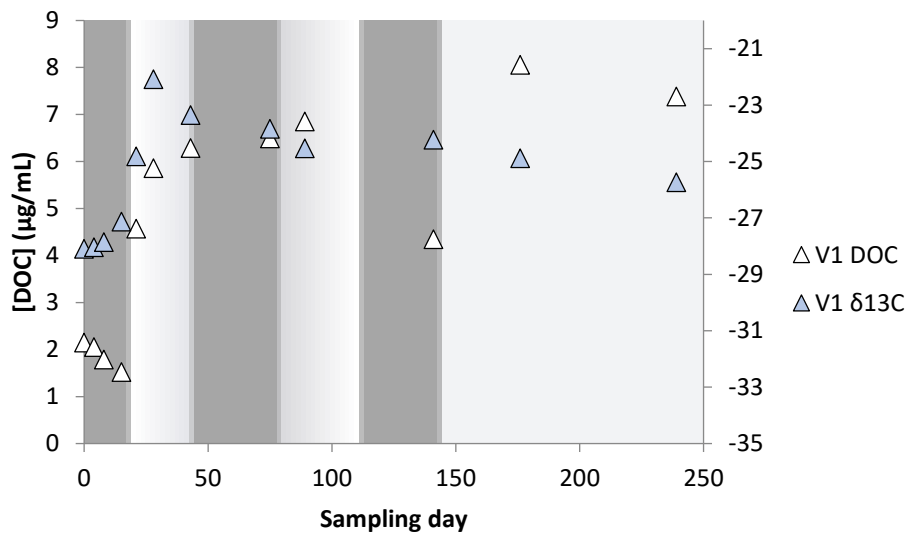


Figure A2-11: The temporal evolution of the DOC concentration (white) and $\delta^{13}\text{C}$ signature (teal) for the mixed redox, Fe amended scenario. Periods appearing with a grey background were anoxic at the time of subsampling while those appearing on a white background were subsampled while the vials were maintained under oxic conditions. V1 and V2 each represent duplicate vials.

Anoxic Condition

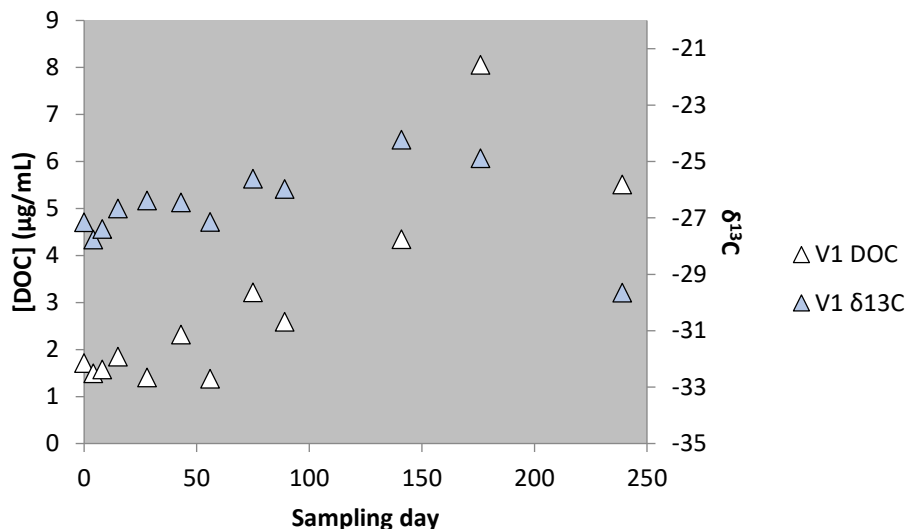


Figure A2-12: The temporal evolution of the DOC concentration (white) and $\delta^{13}\text{C}$ signature (teal) for the anoxic, Fe scenario. V1 and V2 each represent duplicate vials.

Iron concentration profiles

Dissolved iron concentrations were measured in the anoxic control scenarios, in part to verify that the anoxic redox conditions were properly maintained throughout the incubation and during sampling. Control incubations were connected downstream of all other vials (Figure 1 of manuscript). Given the experimental design, these vials would be the first to become oxic due to a break in the flow of nitrogen gas used to maintain anoxic conditions. In the aerobic scenarios, soluble iron(II) concentrations were below detection limit within one week of the start of the incubations (except for one point in the mixed redox condition, which we believe to be a method or sampling artifact). In contrast, under the anoxic scenario, there was progressive release of dissolved iron from the unamended, natural sediment, to a concentration slightly above $1 \mu\text{g mL}^{-1}$. Time series of dissolved iron concentrations in the control vials are shown below (only the most downstream of the duplicate vials was sampled for this analysis).

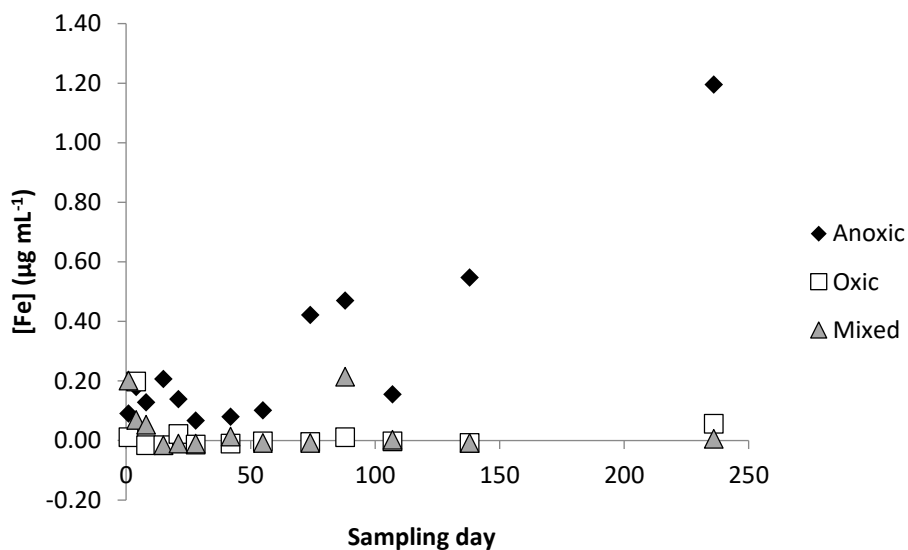


Figure A2-13: Soluble Fe²⁺ concentration with time for the unamended control vials in the anoxic, oxic and mixed redox scenarios.

Dissolved iron(II) concentrations in vials amended with iron(II) chloride were below detection within one week following its addition. In reactors maintained under anoxic conditions, iron(II) concentrations decreased from 250 µg mL⁻¹ to about 20 µg mL⁻¹ upon the addition of iron(II) chloride (Fe and Fe-OM scenarios), most likely in response to the strong affinity of iron(II) for sedimentary mineral surfaces (Burdige, 1993), its precipitation as sulfides throughout the incubation, as well as its oxidation to iron(III) by electron acceptors other than oxygen, such as manganese oxides and nitrate, at the start of the incubation (Magen et al., 2011). Iron(II) profiles of iron amended scenarios are shown here:

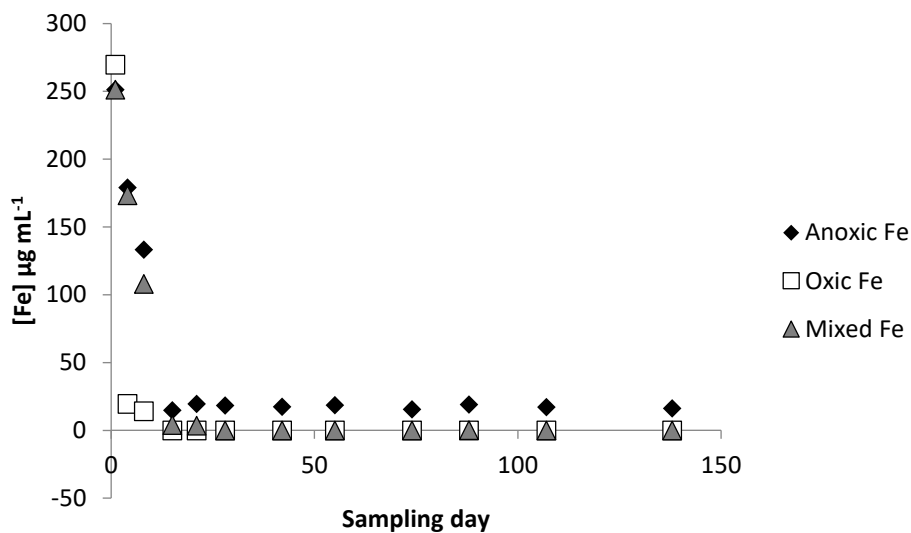


Figure A2-14: Soluble Fe²⁺ concentration with time for the Fe(II) amended vials in the anoxic, oxic and mixed redox scenarios.

It should be noted that dissolved iron was not measured in the OM-amended incubations as high DOM concentrations interfere with the complexation iron(II) to ferrozine and the generation of the chromophoric product.

Calculations for thermodynamic feasibility of feammox in marine sediments

Luther III et al. (1997) were first to propose the possible coupling of ammonium oxidation to N₂ through iron oxide reduction, though they state that Fe³⁺ catalysis of N₂ formation can only occur at pH < 6.8 based on pE-pH calculations. Above this pH, (Luther III et al., 1997) state that “the reaction between Fe³⁺ species and NH₄⁺ to form N₂ is thermodynamically unfavorable”. In contrast, Yang et al. (2012) note that “... Feammox to N₂ using ferrihydrite, a poorly crystalline Fe oxide ... remains energetically favorable over a wide pH range”. The thermodynamic feasibility of this reaction in soil systems is outlined in the supplementary information of Yang et al. (2012).

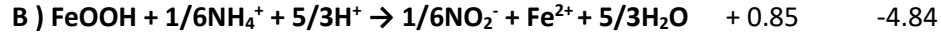
In the following section, we repeat these calculations, using reaction conditions typically found in marine sediments.

Firstly, we reproduced the electrochemical half-reactions D and G featured in Luther (1997) and associated $\log(K)$ and ΔG° values. We also show the reduction of nitrite to ammonium using $\log(K)$ values from Stumm and Morgan (1970) (labelled below as equation H):

Half reactions:	Log (K)	ΔG° (kJ/mol)
D) $1/6\text{N}_2 + 4/3\text{H}^+ + \text{e}^- \rightarrow 1/3\text{NH}_4^+$	+ 4.65	-91.12
G) $\text{FeOOH} + 3\text{H}^+ + \text{e}^- \rightarrow \text{Fe}^{2+} + 2\text{H}_2\text{O}$	+ 15.99	-20.50
H) $1/6 \text{NO}_2^- + 4/3 \text{H}^+ + \text{e}^- \rightarrow 1/6 \text{NH}_4^+ + 1/3 \text{H}_2\text{O}$	+ 15.14	-86.27

The reduction reaction of iron oxide (equation G) can be coupled to the oxidation of ammonium (reverse of equation D and H) by reversing equations D and H and adding them to equation G to yield electrochemical reactions A and B (table below). $\log(K)$ values for the complete electrochemical reactions can then be calculated by subtracting $\log(K)$ of D or H from the $\log(K)$ of G (as carried out in Luther 1997):

Half reactions:	Log (K)	ΔG° (kJ/mol)
A) $\text{FeOOH} + 1/3\text{NH}_4^+ + 5/3\text{H}^+ \rightarrow 1/6\text{N}_2 + \text{Fe}^{2+} + 2\text{H}_2\text{O}$	+ 11.34	-64.62



Positive Log(K) and negative ΔG° indicate that these reactions are thermodynamically feasible when the system is under standard conditions, i.e. at a temperature of 298 K, total pressure of 1 atmosphere when all solutes are assigned a unit activity. We can calculate ΔG values for the reactions under conditions that are more typical of marine sediments using the following equation for process A.

$$\Delta G = \Delta G^\circ + RT \ln \frac{[\text{N}_2]^{1/6} [\text{Fe}^{2+}]^1 [\text{H}_2\text{O}]^2}{[\text{FeOOH}]^1 [\text{NH}_4^+]^{1/3} [\text{H}^+]^{5/3}}$$

where R is the gas constant (0.008314 kJ/mol*K) and T is the temperature in K (277 K). An activity of 1 is assigned to the solid-phase iron oxide minerals (FeOOH) and water as activities of pure solids and liquids are assumed to be equal to unity (Laidler and Meiser, 1999). The concentration of N_2 was at 0.001 mol/L (as used by Yang (2012)), based its aqueous solubility. Fe^{2+} concentrations in oxic sediment porewaters are extremely low since Fe^{2+} is quickly oxidized to Fe^{3+} and precipitated as iron oxides. We used 0.06nM, the solubility of freshly precipitated ferrihydrite in oxic seawater (Raiswell and Canfield, 2012), for our Fe^{2+} concentration. The equation therefore becomes:

$$\Delta G = -64.62 + 0.008314 * 277 * \ln \frac{[0.001]^{1/6} [0.06 * 10^{-9}]^1 [1]^2}{[1]^1 [\text{NH}_4^+]^{1/3} [\text{H}^+]^{5/3}}$$

We can isolate the NH_4^+ and H^+ concentrations from the equation to determine the pH and ammonium concentration dependency of the Gibb's free energy for the oxidation of ammonium and iron oxide reduction:

$$\Delta G = -64.62 + 0.008314 * 277 * \left(\ln(1.9 * 10^{-10}) - \frac{1}{3} \ln \text{NH}_4^+ - 2.3 \frac{5}{3} \log[\text{H}^+] \right)$$

$$\Delta G = -64.62 + 0.008314 * 277 * \left(\ln(1.9 * 10^{-10}) - \frac{1}{3} \ln NH_4^+ + 3.83pH \right)$$

We chose to determine ΔG as a function of both NH_4^+ (from $5\mu M$ to $300\mu M$) and pH (0 to 14) for equation A. Values are displayed in the matrix below:

pH	NH_4^+	5E-6	10E-6	20E-6	30E-6	50E-6	150E-6	200E-06	300E-06
↓	(μM)	→							
0		-106.8	-107.3	-107.9	-108.2	-108.6	-109.4	-109.6	-109.9
1		-98.0	-98.5	-99.0	-99.3	-99.7	-100.6	-100.8	-101.1
2		-89.1	-89.7	-90.2	-90.5	-90.9	-91.7	-92.0	-92.3
3		-80.3	-80.8	-81.4	-81.7	-82.1	-82.9	-83.1	-83.4
4		-71.5	-72.0	-72.5	-72.8	-73.2	-74.1	-74.3	-74.6
5		-62.6	-63.1	-63.7	-64.0	-64.4	-65.2	-65.4	-65.8
6		-53.8	-54.3	-54.8	-55.2	-55.5	-56.4	-56.6	-56.9
7		-44.9	-45.5	-46.0	-46.3	-46.7	-47.5	-47.8	-48.1
8		-36.1	-36.6	-37.2	-37.5	-37.9	-38.7	-38.9	-39.2
9		-27.3	-27.8	-28.3	-28.6	-29.0	-29.9	-30.1	-30.4
10		-18.4	-19.0	-19.5	-19.8	-20.2	-21.0	-21.3	-21.6
11		-9.6	-10.1	-10.6	-11.0	-11.4	-12.2	-12.4	-12.7
12		-0.7	-1.3	-1.8	-2.1	-2.5	-3.4	-3.6	-3.9
13		8.1	7.6	7.0	6.7	6.3	5.5	5.3	4.9
14		16.9	16.4	15.9	15.6	15.2	14.3	14.1	13.8

ΔG values highlighted in yellow are not thermodynamically feasible (positive) under conditions typically found in sediments. Feammox can theoretically occur under conditions typically observed in marine

sediment porewaters as the upper pH limit for feammox to N₂ using ferrihydrite is 13, a value that is well above that of seawater (pH ≈ 8).

Likewise, we can calculate ΔG for equation B (feammox to NO₂⁻). Values are displayed in the matrix below:

pH	NH ₄ ⁺ (μM)	5E-6	10E-6	20E-6	30E-6	50E-6	150E-6	200E-06	300E-06
↓	→								
0		-52.3	-52.6	-52.9	-53.0	-53.2	-53.6	-53.7	-53.9
1		-43.5	-43.8	-44.0	-44.2	-44.4	-44.8	-44.9	-45.1
2		-34.6	-34.9	-35.2	-35.3	-35.5	-36.0	-36.1	-36.2
3		-25.8	-26.1	-26.3	-26.5	-26.7	-27.1	-27.2	-27.4
4		-17.0	-17.2	-17.5	-17.7	-17.9	-18.3	-18.4	-18.5
5		-8.1	-8.4	-8.7	-8.8	-9.0	-9.4	-9.6	-9.7
6		0.7	0.4	0.2	0.0	-0.2	-0.6	-0.7	-0.9
7		9.5	9.3	9.0	8.9	8.7	8.2	8.1	8.0
8		18.4	18.1	17.8	17.7	17.5	17.1	17.0	16.8
9		27.2	27.0	26.7	26.5	26.3	25.9	25.8	25.6
10		36.1	35.8	35.5	35.4	35.2	34.7	34.6	34.5
11		44.9	44.6	44.4	44.2	44.0	43.6	43.5	43.3
12		53.7	53.5	53.2	53.0	52.8	52.4	52.3	52.2
13		62.6	62.3	62.0	61.9	61.7	61.3	61.2	61.0
14		71.4	71.1	70.9	70.7	70.5	70.1	70.0	69.8

This process is not thermodynamically favorable at seawater pH (pH ≈ 8) when ferrihydrite is used as a substrate. Nevertheless, it is interesting to consider how the ΔG° of feammox to either N₂ or NO₂⁻ are affected by the choice of iron oxide substrate. ΔG° for a chemical reaction can be calculated from the Gibb's free energy of formation (ΔG°_f) of all the species involved. For example, ΔG° for feammox to N₂ (process A) can be calculated from:

$$\Delta G^\circ = \frac{1}{6} \Delta G^\circ_{f(N_2)} + \Delta G^\circ_{f(Fe^{2+})} + 2\Delta G^\circ_{f(H_2O)} - \Delta G^\circ_{f(FeOOH)} - \frac{1}{3} \Delta G^\circ_{f(NH_4^+)} - \frac{5}{3} \Delta G^\circ_{f(H^+)}$$

ΔG° for feammox to NO_2^- (process B) can be calculated from:

$$\Delta G^\circ = \frac{1}{6} \Delta G^\circ_{f(\text{NO}_2^-)} + \Delta G^\circ_{f(\text{Fe}^{2+})} + \frac{5}{3} \Delta G^\circ_{f(\text{H}_2\text{O})} - \Delta G^\circ_{f(\text{FeOOH})} - \frac{1}{6} \Delta G^\circ_{f(\text{NH}_4^+)} - \frac{5}{3} \Delta G^\circ_{f(\text{H}^+)}$$

The ΔG°_f of the iron oxide substrate used by Luther (1997) was -699 kJ/mol; a value that is associated to ferrihydrite formation (Stumm and Morgan, 1970). Oxyhydroxides (nominally FeOOH), such as ferrihydrite, are generally thought to precipitate first from sediment porewaters, and are likely ammonium substrates in feammox. On the other hand, oxyhydroxides come in a variety of polymorphs (e.g. ferrihydrite, goethite, lepidocrocite), each having different morphologies, particle sizes as well as surface properties (e.g. level of hydration, isoelectric point, charge, reactivity.. etc.) (Navrotsky et al., 2008). Each of these factors greatly affects the oxyhydroxide's ΔG°_f which, in turn, influences the thermodynamic feasibility of the reaction of interest. For example, the ΔG°_f of goethite and lepidocrocite (-490.6 and -482.7 kJ/mol respectively, (Navrotsky et al., 2008)) are significantly different from the ΔG°_f of ferrihydrite (-699 kJ/mol). Using the ΔG°_f of goethite instead of ferrihydrite changes the ΔG° of equation A from -64.62 kJ/mol to -273.02 kJ/mol and ΔG° of equation B from -4.84 kJ/mol to -213.24 kJ/mol, which makes both reactions thermodynamically feasible at *all* pH conditions and ammonium concentrations encountered in marine sediments. Since nanophases of goethite have been identified as the dominant oxyhydroxide phase in lake and marine sediments (Van der Zee et al., 2003), it is not unreasonable to use these newly calculated ΔG° values to assess the thermodynamic feasibility of feammox in marine sediments. We therefore feel justified in stating that it is *possible* that feammox takes place during our incubation experiments.